Acausal Powertrain Modelling with Application to Model-based Powertrain Control

by

Hadi Adibi Asl

A thesis
presented to the University of Waterloo
in fulfillment of the
thesis requirement for the degree of
Doctor of Philosophy
in
Mechanical and Mechatronics Engineering

Waterloo, Ontario, Canada, 2014

Abstract

The automotive industry has long been searching for efficient ways to improve vehicle performance such as drivability, fuel consumption, and emissions. Researchers in the automotive industry have tried to develop methods to improve fuel consumption and reduce the emission gases of a vehicle, while satisfying drivability and ride comfort issues. Today, by developing computer/software technologies, automotive manufacturers are moving more and more towards modelling a real component (prototype) in a software domain (virtual prototype). For instance, modelling the components of a vehicle's powertrain (driveline) in the software domain helps the designers to iterate the model for different operating conditions and scenarios to obtain better performance without any cost of making a real prototype.

The objective of this research is to develop and validate physics-based powertrain models with sufficient fidelity to be useful to the automotive industry for rapid prototyping. Developing a physics-based powertrain model that can accurately simulate real phenomenon in the powertrain components is of great importance. For instance, a high-fidelity simulation of the combustion phenomenon in the internal combustion (IC) engine with detailed physical and chemical reactions can be used as a virtual prototype to estimate physical prototype characteristics in a shorter time than it would take to build a physical prototype. Therefore, the powertrain design can be explored and validated virtually in the software domain to reduce the cost and time of product development.

The main focus of this thesis is on development of an internal combustion engine model, four-cylinder spark ignition engine, and a hydrodynamic torque converter model. Then, the models are integrated along with the rest of a powertrain's components (e.g. vehicle longitudinal dynamics model) through acausal connections, which represents a more feasible physics-based powertrain model for model-based control design. The powertrain model can be operated at almost all operating conditions (e.g. wide range of the engine speeds and loads), and is able to capture some transient behaviour of the powertrain as well as the steady state response. Moreover, the parametric formulation of each component in the proposed powertrain model makes the model more efficient to simulate different types of powertrain (e.g. for a passenger car or truck).

Acknowledgements

I would like to express
My deep appreciation to my supervisor, Professor John McPhee
for his continued support, valuable guidance,
and the academic environment he provided during the course of research.

I would like to thank
My co-supervisor, Professor Roydon Fraser
for his valuable guidance and fruitful discussions during my PhD research.

I also wish to thank
My committee members, Professor Andrzej Sobiesiak, Professor Steve Lambert,
Dr. Nasser Lashgarian Azad, and Dr. John Wen for reviewing and improving my thesis.

I am grateful to
My friends and colleagues at the Motion Research Group (MoRG),
for providing a friendly and dynamic environment.

Sincere thanks to
My sponsors, Natural Sciences and Engineering Research Council of Canada (NSERC),
Toyota, and Maplesoft Company for their financial supports.

Finally and most importantly, I would like to acknowledge
My parents, and my brothers throughout all these years,
for giving me the encouragement, understanding, and care.

Dedication

To the great men and women,
who have dedicated their lives
to spread peace and love

Table of Contents

List of Tables

List of Figures

Nomenclature

$[\ ]$	Molar concentration of species
α_p	Torque converter's pump blade angle
α_s	Torque converter's stator blade angle
α_t	Torque converter's turbine blade angle
α_{road}	Road inclination
$\bar{R}$	Universal gas constant
$\bar{U}_p$	Mean piston speed
β_{arm}	Armature damping coefficient
χ_i	Molar fraction of species during reaction
ΔGB_i	Gibbs free energy of species
ΔP_v	Valve pressure loss
Δt_{cycle}	cycle time
ΔV_d	Cylinder displaced volume change
δW_f	Friction work
Δx	Piston displacement
η_v	Volumetric efficiency
$\frac{A}{F}$	Air-fuel ratio

γ	Specific heat capacity ratio
κ_{P_i}	Equilibrium constant of the i^{th} equilibrium reaction
μ	Viscosity
μ_ω	Velocity-dependent friction coefficient
ν	Velocity
ν_w	Wind velocity
ω_{tire}	Tire angular speed
Φ	Equivalence ratio
ϕ	Throttle angle
ρ_b	Density of burned mixture
ρ_i	Inlet gas density
ρ_u	Density of unburned mixture
ρ_{air}	Air density
ρ_{TC}	Torque converter's oil density
τ_p	Torque converter's pump torque
τ_R	Resistant torque
τ_s	Torque converter's stator torque
τ_t	Torque converter turbine's torque
τ_{axle}	Axle torque
τ_{brake}	Resistant brake torque
$\tau_{ElecMag}$	Electromagnetic torque from DC motor
τ_{in}	Input torque
τ_{out}	Output torque

τ_{pe}	Torque converter's pump equilibrium torque
τ_{se}	Torque converter's stator equilibrium torque
τ_{te}	Torque converter's turbine equilibrium torque
θ	Crank angle
θ_{SOC}	Start of combustion crank angle
ε_{oil}	Oil film thickness between the ring and cylinder wall
ζ	Tire slip ratio
A_f	Flame front area
a_i	Wiebe function constant parameters i=1,2
A_p	Piston area
A_w	Cylinder wall area
A_{EGR}	EGR valve area
A_{front}	vehicle frontal area
A_{TC}	Torque converter's average flow area
A_{Th}	Throttle valve area
B	Cylinder bore diameter
BD	Burn duration
C_f	Torque converter frictional loss coefficient
C_D	Discharge coefficient
C_{geo}	Brake geometry constant
c_{pb}	Burned specific heat capacity at constant pressure
c_{pu}	Unburned specific heat capacity at constant pressure
C_{sh}	Torque converter shock loss coefficient

C_{skirt}	Piston skirt clearance
c_{vb}	Burned specific heat capacity at constant volume
c_{vu}	Unburned specific heat capacity at constant volume
CR	Compression ratio
D	Throttle bore diameter
d	Throttle pin diameter
D_{air}	Air drag coefficient
E_i	Efficiency of i^{th} gear
F_n	Braking normal force
F_p	Piston force
F_{aero}	Aerodynamic force
F_{grav}	Gravitational force
f_{mep}	Mean effective pressure friction
F_{roll}	Rolling resistant force
F_x	Tire traction force
F_z	Tire vertical force
g	Gravitational acceleration
G_i	i^{th} gear
h_b	Burned enthalpy
H_i	Heat transfer constant parameters i=1,2,3
h_u	Unburned enthalpy
I_p	Torque converter's pump inertia
I_s	Torque converter's stator inertia

I_t	Torque converter's turbine inertia
I_{arm}	Armature inertia
i_{dyno}	Source of current of dyno
I_{tire}	Tire inertia
K_D	PID derivative gain
K_I	PID integral gain
K_P	PID proportional gain
K_{dyno}	Dyno torque constant
L_f	Torque converter's fluid inertia length
l_t	Length of eddies
L_{iv}	Maximum valve lift
L_{ring}	Piston ring length
L_{rod}	Connecting rod length
L_{skirt}	Piston skirt length
m_b	Mass of burned mixture
m_e	Flame entrained mass
m_u	Mass of unburned mixture
M_v	vehicle mass
m_{cv}	Control volume mass
m_{Cyl}	Total in-cylinder mass
m_{EGR}	EGR mass flow
m_{Fuel}	Fuel mass
m_{Th}	Throttle mass flow

n	engine rpm
n_{Ref}	Reference engine rpm
P_b	Burned pressure
P_L	Torque converter power loss
P_m	Intake manifold pressure
P_u	Unburned pressure
P_{atm}	Atmospheric pressure
P_{Cyl}	In-cylinder pressure
P_{exh}	Exhaust pressure
P_{in}	Pressure during intake stroke
Q_b	Heat transfer between burned zone and cylinder walls
Q_u	Heat transfer between unburned zone and cylinder walls
Q_{TCe}	Torque converter equilibrium volumetric flow rate
Q_{TC}	Torque converter's volumetric flow rate
R_b	Specific gas constant for burned mixture
r_p	Torque converter's pump radius
r_s	Torque converter's stator radius
r_t	Torque converter's turbine radius
R_u	Specific gas constant for unburned mixture
r_{crank}	Crank radius
r_{tire}	Tire radius
Re	Reynolds number
S_l	Laminar flame speed

S_p	Torque converter's pump design constant
S_p	Torque converter's stator design constant
S_t	Torque converter's turbine design constant
SA	Spark advance angle
t	time
T_0	Ambient temperature
T_b	Burned temperature
t_b	Time duration to burn eddies
t_D	PID derivative time constant
t_I	PID integral time constant
T_m	Intake manifold temperature
T_u	Unburned temperature
T_w	Cylinder wall temperature
T_{EGR}	EGR temperature
T_{exh}	Exhaust temperature
T_{in}	Temperature during intake stroke
$T_{sampler}$	Triggered sampler time constant
T_{Th}	Throttle temperature
U_i	Inlet gas speed
U_p	Piston speed
U_t	Characteristics speed of eddies
V_b	Volume of burned mixture
V_c	Cylinder clearance volume

V_d	Displaced volume
V_f	Volume of spherical flame
V_m	Intake manifold volume
V_u	Volume of unburned mixture
V_θ	Instantaneous cylinder volume
V_{exh}	Exhaust manifold volume
w_p	Torque converter's pump angular speed
w_s	Torque converter's stator angular speed
w_t	Torque converter's turbine angular speed
w_{arm}	Armature angular speed
w_{in}	Input angular speed
w_{out}	Output angular speed
w_{pe}	Torque converter's pump equilibrium angular speed
w_{se}	Torque converter's stator equilibrium angular speed
w_{te}	Torque converter's turbine equilibrium angular speed
X_i	Molar fraction of species

Chapter 1

Introduction

A vehicle powertrain is a combination of mechanical, electrical, and hydraulic components that transfer power from the engine, combustion released energy, to the wheels. The combustion power is transferred through the mechanical mechanism such as manual or automatic transmission system. The reduction of fuel consumption and emissions are two active areas of vehicle research. It is of great importance to design powertrain components to improve fuel consumption and reduce emissions while satisfying drivability and ride comfort issues.

Recently by developing advanced simulation tools [30, 34, 56, 75, 85], modeling large dynamic systems (high-fidelity models) has been efficiently done and iterated for different operating conditions. Therefore, the efficient powertrain models have significantly helped the automotive industry to reduce the cost of production.

1.1 Background

Today, automobile manufacturers are moving towards more and more virtual vehicle prototypes including prototypes of the powertrain. A virtual prototype is the modeling and simulation of a physical (real) prototype in a software environment (virtual domain). The main advantages of modeling virtual prototypes before making physical prototypes are:

- Lower expenses: the cost of making a virtual prototype is dramatically less than the physical prototype.
- Higher quality: virtual prototypes enable the rapid virtual testing of many iterations to study the effect of parameter changes on a design thus improving the quality of the physical prototype when constructed.
- Shorter time to present the product to markets: this has recently been one of the key progresses in attracting customers, by advertising and showing the virtual prototype operations which are similar to the real prototypes.

In the automotive industry, specifically in vehicle dynamics modeling and simulation, several software packages have been developed such as Adams, MapleSim, Dymola, CarSim, and so on. In this project, the major part of the modeling and simulations are executed in MapleSim.

MapleSim, one of the products of the Maplesoft company, is a multi-domain modeling and simulation tool to build dynamic models from different domains (e.g. mechanical, electrical, and hydraulic). The main advantages of employing this software for modeling and simulation of the powertrain components are:

- The powerful and user-friendly library which includes components from different domains, and the ability to combine both causal and acausal components
- The ability to generate a user-defined component, either a causal or an acausal component, by custom component option
- Powerful ability to generate symbolic equations and optimized simulation code
- Exploring the model in various ways such as parameter optimization, model reduction, and sensitivity analysis by manipulating the equations behind the model

An acausal system is suitable in vehicle dynamics modeling and simulation where the connections are usually flanges and the response of the component is not only based on the past/current inputs, but also it is affected by the future inputs.

Figure 1.1 shows the operation of the acausal system in comparison with the causal system. In the causal model the direction of information flow is defined, see the lower diagram in Figure 1.1, and the power flows in one direction (e.g. from left to the right side of the component). In the acausal system, the upper diagram, the power flow direction can be either from left to right or vice versa. Therefore, an acausal modeling approach is more suitable for systems which the direction of information flow between components is not specified (e.g. powertrain simulation) [32].

MapleSim provides a good library to generate acausal models from the library of components and user-defined components (custom components).

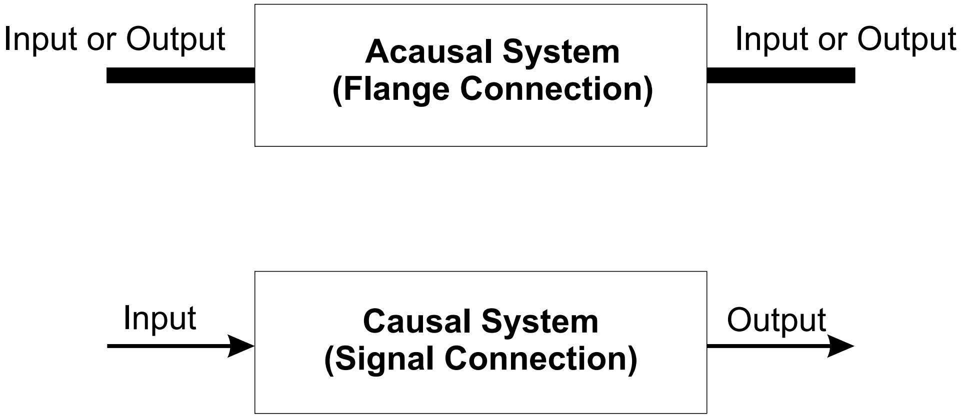

Figure 1.1: Acausal vs. causal system

1.2 Motivation and Objectives

Cars play an important role in our everyday life. However, the fast growth of automotive companies and consequently the number of cars has caused some serious problems regarding the vehicle fuel and environmental issues.

Researchers in the automotive industry have tried to develop methods to improve fuel consumption and reduce the exhaust gases and emissions of vehicles. For these purposes the modeling and simulation of the vehicle powertrain (driveline) has been of great importance. The power, or energy, in the powertrain can be generated either in the internal combustion (IC) engine via chemical reactions or in the electric motors by using the charges of batteries in hybrid electric vehicles (HEVs). Then, the generated power is transformed to mechanical power, through the set of gears, clutches, and shafts, to move the vehicle.

From this point of view, the design of the detailed powertrain system model significantly helps the automotive manufacturers to evaluate the performance of the virtual powertrain prototype and test different controllers to improve the fuel consumption and emission issues while satisfying the drivability and ride comfort of passengers. The approach of powertrain modeling with physical meaningful parameters and equations, which is called physics-based modelling, gives a detailed view of powertrain components and operations. The most important benefit of using physics-based models is to track the effects of the physical-meaning parameters on the system operation. For instance, the schematic diagram in Figure 1.2 shows different approaches to the modeling of IC engines. As indicated in Figure 1.2, the IC engine model includes more and more physical parameters by approaching from the left to the right of the diagram.

The first approach shown in Figure 1.2, the empirical method, uses experimental data to simulate the IC engine model. The empirical modeling approach is usually represented by a group of look-up tables. The second approach, the power balancing, is a combination of empirical data and physics-based equations. Mean-value engine modelling is an example of using both physics-based equations (e.g. mass and energy conservation equations) and look-up tables (e.g. combustion model). The third approach includes simulations of the combustion model as well as thermodynamic equations. For instance, a two-zone combustion model with flame propagation through the combustion chamber can be categorized in this group. Finally, the most complex modeling approach can simulate the fluid flow dynamics by employing finite element methods (FEM) and computational fluid dynamics (CFD) packages.

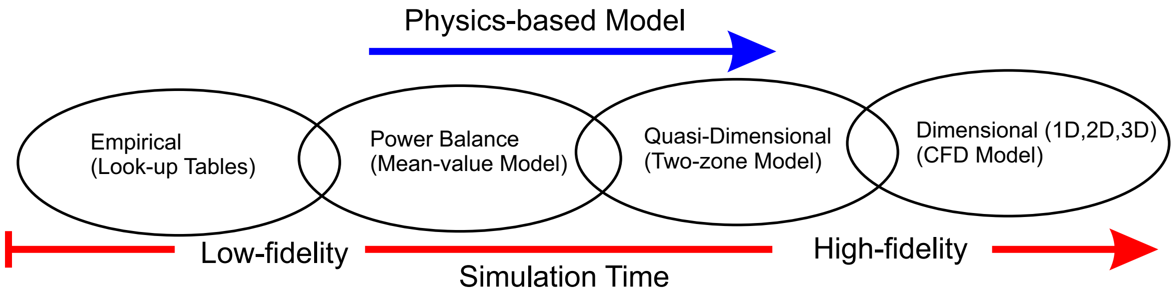

Figure 1.2: Different approaches of IC engine model

The major part of the proposed research is focused on the modeling and simulation of powertrain components, specifically the physics-based acausal IC engine model and the automatic transmission model, in the MapleSim environment.

As mentioned in the previous section, the approach of physics-based models has grown up in the automobile industry. A high-fidelity physics-based powertrain model can represent a suitable virtual prototype of a real powertrain (physical prototype). Therefore, the powertrain design can be explored and validated virtually in the software domain to reduce the cost of making physical prototypes.

Typically, the major components in an automatic powertrain model, as shown in Figure 1.3, are: driver model, engine model, torque converter model, transmission model, differential model, chassis model, brake model, tire model, and resistant forces model.

However some of the mentioned components can be modeled using the elements in the MapleSim library such as the braking model and the tire model, so the main focus of the proposed research is on modeling the IC engine and the automatic transmission (including the math-based torque converter model).

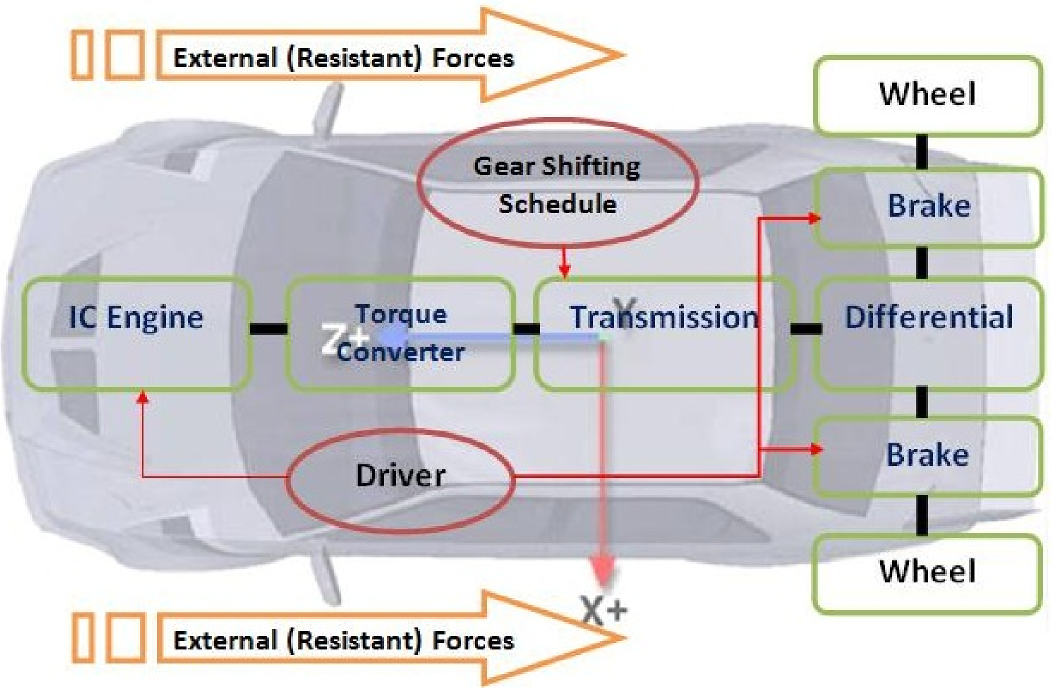

Figure 1.3: Schematic automatic driveline diagram

The proposed powertrain model is a fully acausal model. In other words, all components (except for the driver) are connected through flange connections. The thick lines among the components in Figure 1.3 represent the shaft or flange connections, and the thin arrows represent the control signals. For instance, in an automatic transmission, the driver can control the vehicle speed by changing the throttle angle via the gas pedal, or by pushing on the brake pedal.

The proposed physics-based IC engine model will contain the four strokes in the Otto cycle diagram: the intake, compression, combustion, and exhaust. All four stroke operations will be represented by physics-based modeling approaches. Furthermore, all causal sub-systems, which are usually represented by look-up tables, such as the thermal efficiency and the volumetric efficiency in the mean-value model, will be replaced by fully physical meaning representations.

The level of complexity of the combustion stroke, which is the most important part of the model, will be defined so as to predict the brake power, the engine output shaft power, and the emission gases (CO, NO_x). For this purpose, the modeling approaches will start by considering a single zone combustion model. Although the single zone cannot predict the emission gases, it is a suitable approach to model physics-based combustion to determine the variations of the pressure and the temperature, which will be compared against literature values.

The next step will be using a two-zone approach to model combustion. In this level, the combustion zone is divided into the burned and unburned zones, and the flame propagation (flame speed and shape) will be modeled during the combustion. Then the chemical reactions will be entered in the flame propagation model to predict the emissions [68]. The proposed engine model will be added to the acausal torque converter model at the pump shaft, and the rest of the powertrain components will connect to the torque converter through the torque converter turbine shaft. The proposed physics-based powertrain model is a complete package for component-level and system-level simulation to capture both transient and steady state behaviour of the dynamic system. Moreover, the fast simulation time makes the model appropriate for model-based control development and hardware-in-the-loop (HIL) tests.

The original contributions of the proposed research can be summarized as follows:

- Physics-based torque converter model: The model is able to capture torque converter characteristics in all operating modes. The damping characteristics and frequency response of the model as well as the parametric sensitivity analysis are studied in this research. The model is reusable for different powertrain configurations. Since very few literatures have studied a torque converter reverse flow operation, as well as flow transition, the developed model in this dissertation is fully described the reverse flow and flow transition simulation in both component-level and system-level simulation (e.g. engine braking phenomenon in a powertrain simulation).

- Physics-based four-cylinder SI engine model: The developed SI engine model, in Chapter 4 of this dissertation, is able to simulate in-cylinder variations at each crank angle such as pressure, temperature, brake torque, fuel consumption, and emission gases. The multibody dynamics is integrated along with the four-stroke (two-zone combustion) SI engine model. The model is able to simulate many cycles simulation with fast simulation time (faster than real-time simulation), which makes the model suitable for an engine model-based control development and optimization.
- Acausal integrated powertrain model: The multibody crankshaft model of the SI engine is connected to the acausal torque converter model, automatic transmission, differential gear, brake, tire, and longitudinal chassis model (see Chapter 5). The originality of the proposed powertrain model is its feasibility (due to the acausal modeling approach), fast simulation (due to the optimized code generation in MapleSim), and generating simulation results with variable engine operating speed. The whole acausal powertrain model is treated as a hybrid dynamic system (includes both continuous and discrete state variables) with variable initial conditions at each time step.

The powerful DAEs' stiff solvers in MapleSim and custom component development based on a Modelica language, helps more to handle complex hybrid dynamic system.

1.3 Thesis Layout

The current thesis is organized as:

Chapter 2: This chapter presents relevant literature review in three topics: torque converter modeling, IC engine modeling, and powertrain modeling.

Chapter 3: In this chapter, the hydrodynamic torque converter model is fully described. The dynamic model is created in the MapleSim software, and the model is simulated in all operating modes. Moreover, the damping characteristics of the model is evaluated in different modes for both the linear and non-linear model. The torque converter characteristic is also simulated in the integrated powertrain model.

Chapter 4: This chapter represents modeling and simulation of a spark ignition engine. The SI engine model is created based on a four-stroke operation. The two-zone combustion formulation along with the turbulent flame propagation model is employed to model the combustion process. The model is able to generate simulation results at each crank angle. Moreover, the physics-based SI engine model is cross-validated against the GT-Power simulation results.

Chapter 5: In this chapter, the developed high-fidelity SI engine model is connected to the acausal torque converter model, and the torque converter model is connected to the automatic transmission and vehicle longitudinal dynamics through acausal rotational flange connection. The model is able to generate a many cycle simulation with variable engine speed and load.

Chapter 6: This chapter summarizes the thesis, and highlights the main contributions of the research. It also contains recommendations for future works.

Chapter 2

Literature Review

The following sections review the existing literature on torque converter modeling and IC engine modeling.

2.1 Torque Converter

The torque converter plays an important role in transmitting the engine torque during the multiplication (converter) and coupling (lock-up) modes. The torque multiplication mode happens in lower gear ratios to help the vehicle to start moving, and then at higher gear ratios, the engine and transmission are mechanically connected via the torque converter shaft which is called lock-up mode. Furthermore, during gear shifting, its response characteristics considerably affect the vehicle longitudinal dynamics and, consequently, the fuel consumption and drive quality.

Figure 2.1 depicts the mechanism of a torque converter operation during multiplication and coupling modes. In the intermediate speed, when the turbine speed is increasing, the resultant velocity (ν_R) direction (fluid flow absolute direction) is changed. The resultant velocity direction is significantly changed by increasing the turbine angular speed. Therefore, as shown in the lowest part of the Figure 2.1, the resultant velocity direction hits the back of the stator blades which causes the one-way clutch to disengage and the stator starts rotating freely in a same direction as pump and turbine.

The torque converter characteristic is usually represented by the torque ratio plot, the efficiency plot, and the capacity factor (K-factor) plot versus speed ratio (the ratio of turbine to pump angular speed) (Figure 2.2). The torque ratio in modern torque converters typically starts from some value around 2, in lower gear ratios, and approaches to unity in higher gear ratios. In other words, the torque converter works analogous to a lock-up clutch after the coupling point as if the pump and turbine shaft are mechanically connected. The efficiency plot represents the net power that can be transmitted from the pump side (driver side) to the turbine side (driven side). The capacity factor (K-factor), which is almost independent of the individual speeds and loads, represents the ability of a torque converter to multiply input torque [47].

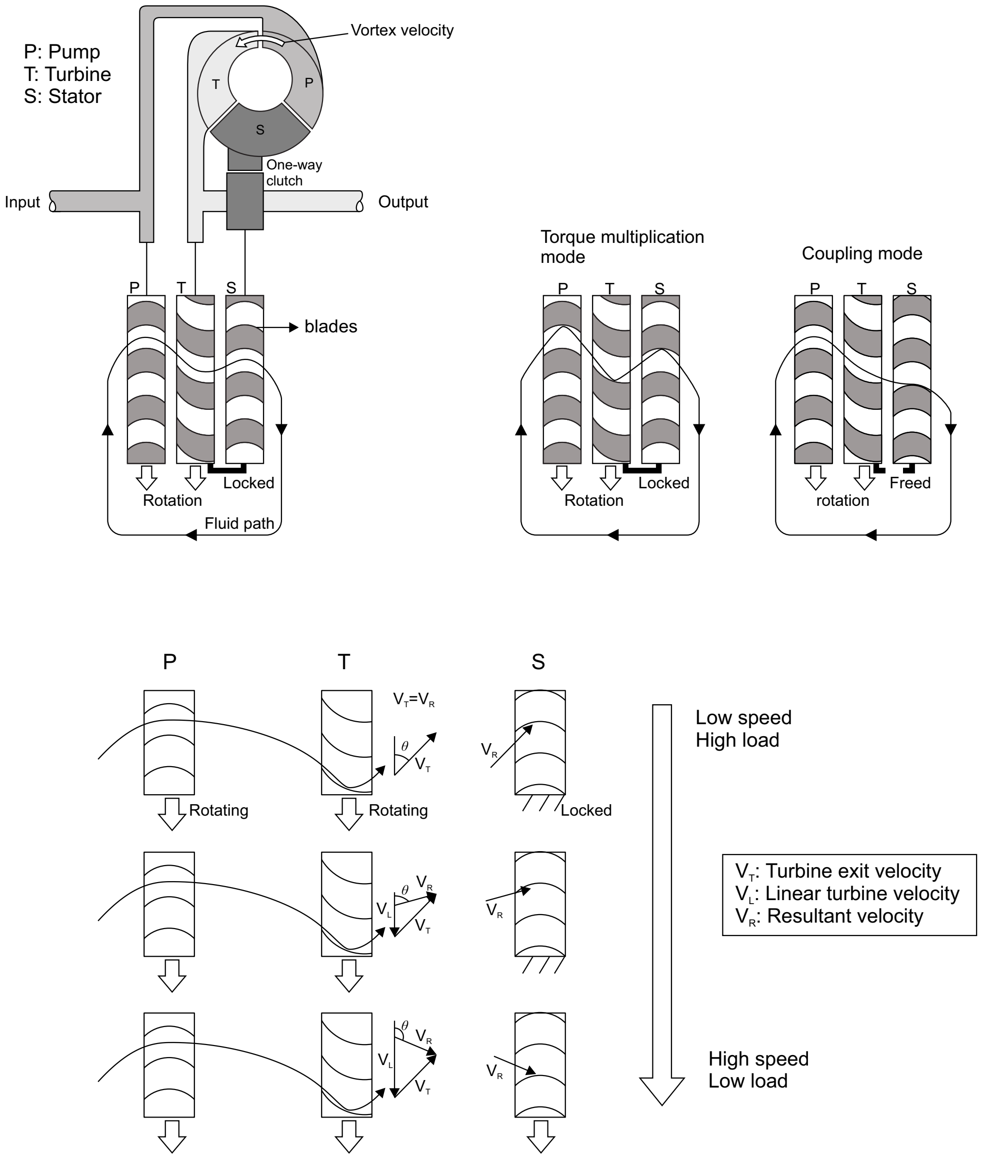

Figure 2.1: Torque converter operation

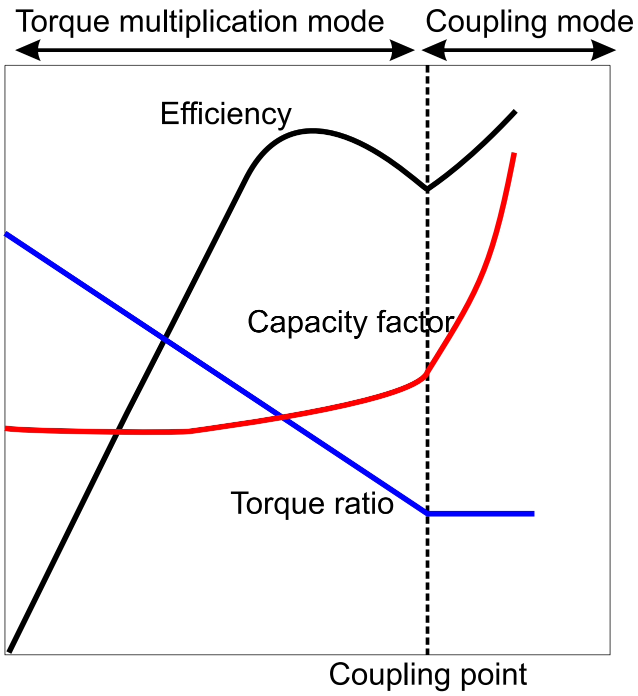

Figure 2.2: Torque converter characteristic plots

A torque converter is an essential component in an automatic powertrain system and it is necessary to know the structure and the dynamic equations of the torque converter. In some powertrain simulations, a torque converter is implemented as a simple look up table which does not reflect the effects of the torque converter parameters. The following literature introduces the related works on dynamic torque converter models.

Ishihara and Emori [48] are among the first authors to consider torque converter transient response. The torque converter model in their work is expressed by three first-order differential equations for pump, turbine, and energy conservation. The transient characteristics and damping effects of the torque converter are studied in that paper and the numerical results are verified with experimental results. Moreover, it concludes that in case of a slow unsteady (transient) phase, the working fluid inertia can be neglected and the steady state equations can be used to describe the torque converter operation.

Kotwicki [54] derived the equations of torque converters to obtain a simplified quadratic algebraic form of torque converter characteristics. The original equations are four steady-state non-linear equations with four states: the angular speed of the pump, turbine, and stator as well as the volumetric flow rate. The simplifications have been done by approximating the volumetric flow rate as a function of the pump and turbine angular speed. Due to the simple nature of algebraic equations in comparison with differential equations, the simplified model in the Kotwicki paper is used along with some controllers to investigate the powertrain dynamics and control. The proposed torque converter in his work is equipped in a powertrain model along with an engine and a transmission.

A comprehensive study of torque converter dynamics is presented by Hrovat and Tobler [47], who used four first-order nonlinear differential equations to represent the torque converter dynamics. The stator dynamic equation is included in this paper [47], and the coupling point, which typically happens when the speed ratio reaches around 90%, is defined based on the stator torque. Bond graph theory is employed to model a torque converter and the numerical results are verified by experimental tests. The proposed model in [47] is useful for investigating the parameter effects on the torque converter performance. Moreover, the transient characteristic of the torque converter can be evaluated. The authors also derive the torque converter equations during the reversal flow mode. This mode, which is also called the overrun mode, happens when the turbine speed is greater than the pump speed and the flow direction is changed. In this case, the turbine drives the pump and the stator overruns. This mode of the torque converter could occur during engine braking or coasting.

A torque converter model with lock-up clutch has been studied in [53, 58, 70]. The simulation results along with experimental results of torque converter with lock-up clutch show that the lock-up clutch improves the torque converter efficiency in higher speed ratios.

Xia and Oh [86] studied the effect of torque converter dynamics on vehicle longitudinal dynamics. The proposed torque converter model in [86] is similar to Hrovat and Tobler's model [47]. The results are compared with Kotwicki's model, which includes merely the steady state behaviour of a torque converter represented by two algebraic equations. The plots show better response of Xia and Ohs torque converter model and the simulation results are closer to the experimental data. This paper [86] verifies that using a torque converter model based on the differential equations is more realistic and the vehicle longitudinal dynamics based on this model is more adjusted to the experiments.

In a paper by Pohl [65], the parameter values for three types of automobile torque converters are given. This paper also studied the transient characteristics of the torque converter using Hrovat and Tobler's equations in the EASY5 software and compared the results with experimental data. The results show that the simple static model can be used for low frequency conditions (e.g. less than $1Hz$). In other words, the transient fluid momentum effects are insignificant for low frequency, but for higher frequencies, between $1 - 10Hz$, the transient fluid momentum must be considered to obtain acceptable results.

Adibi-Asl et al. [2] developed a math-based torque converter model in MapleSim and studied the effects of the torque converter parameters such as the flow area, the blade angles, and the radii of the pump, the turbine, and the stator on the torque converter performance.

The damping characteristics of a torque converter have been evaluated in [26, 50, 69]. Kesy and Kesy [50] studied the damping characteristic of a torque converter during a torque multiplication mode, before coupling point, for different speed ratios. The authors linearized the torque converter equations and approximated the transfer functions, between angular speeds and torques, with a first order system. Moreover, the effects of the torque converter parameters on damping coefficients are discussed in this paper.

Deur et al. [26] derive all transfer functions based on a linearized model for both before and after coupling mode operations. The frequency response (bode diagram) is employed to compare the damping characteristics of a transmission with and without a torque converter. The authors conclude that the torque converter is able to significantly damp the high frequency disturbances transferred from the pump to turbine side and vice versa. However, the pump to pump and turbine to turbine high frequency damping performance is worse than in the converter-less transmission.

The novelty of the physics-based torque converter model in this dissertation (Chapter 3) in comparison to the previous works are:

- All operating modes (multiplication, coupling, and reverse flow) are modeled as an acausal component which is able to simulate flow transition from the forward to the reverse flow operation and vice versa. Moreover, the acausal torque converter model is integrated in an acausal powertrain model to study powertrain system-level characteristics (e.g. engine braking).

- The torque converter damping characteristics is evaluated in all operating modes; more specifically the damping characteristics during the reverse flow mode has not been evaluated before.

2.2 Internal Combustion Engine

The idea of developing combustion engines has been started since the Industrial Revolution in Europe. The purpose of using combustion engines is converting chemical (fuel) reactions to the mechanical work through a suitable mechanism. These engines have been classified based on different criteria such as the type of fuel, working cycle, and ignition methods [45].

The internal combustion (IC) engines can also be categorized based on the fuel ignition:

- Spark ignition engine (SI): the fuel, petrol, is ignited via a spark plug, which is placed at the top of the cylinder.
- Compression ignition engine (CI): the fuel, diesel, in this type has lower self-ignition temperature compared to SI engines. Therefore by increasing the cylinder pressure the temperature inside the cylinder is also increased, and thus the diesel fuel starts self-igniting.

The IC engines, which have been widely used in commercial vehicle powertrains, are usually working in four thermodynamic processes (i.e. four stroke engines). The schematic of a four stroke cycle is shown in Figure 2.3. The process is started by inspiring fresh air and fuel into the cylinder through the intake valve to obtain the air-fuel mixture. Then, the mixture is compressed up to a certain level, close to the top dead center (TDC), where the fuel mixture is ignited via the spark plug. Finally the exhaust gases are driven out from the cylinder through the exhaust valve.

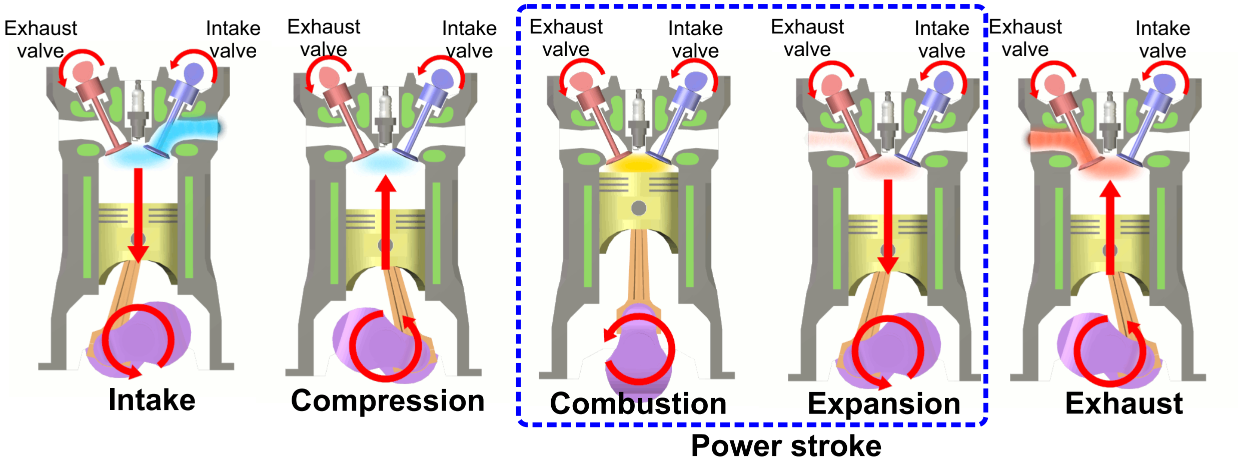

Figure 2.3: Four stroke IC engine operation [*courtesy of Wikipedia*]

IC engines have been modeled in different ways based on the level of the model complexity. For instance, the IC engine characteristics can be expressed by a group of look-up tables, or simple torque-speed differential equations, or a more detailed model with chemical reactions and fluid dynamics.

The following literature review represents some related studies in modeling and simulation of IC engines. The reviews in this section are classified into two modeling approaches. The first approach is the mean-value model, and the second is the spark ignition (SI) engine with combustion model.

2.2.1 Mean-value engine model (MVEM)

Mean-value engine models (MVEMs) are intermediate level IC engine models which include more physical details than simplistic linear transfer function models, but significantly simpler models than large complex cylinder by cylinder models [31]. In this modeling approach the operating time scale is assumed longer than the engine cycle. The detailed combustion dynamics cannot be captured by the MVEM, but the major engine component dynamics can be mathematically formulated in this approach.

The MVEM has been well-known as a suitable plant model for model-based control applications. The combinations of the physics-based components, which allow the physical parameter effects to be evaluated and controlled, and the look-up table models, with fast response, make the MVEM suitable for control applications. The schematic diagram below (Figure 2.4) shows the look-up table models and the physics-based components in the MVEM.

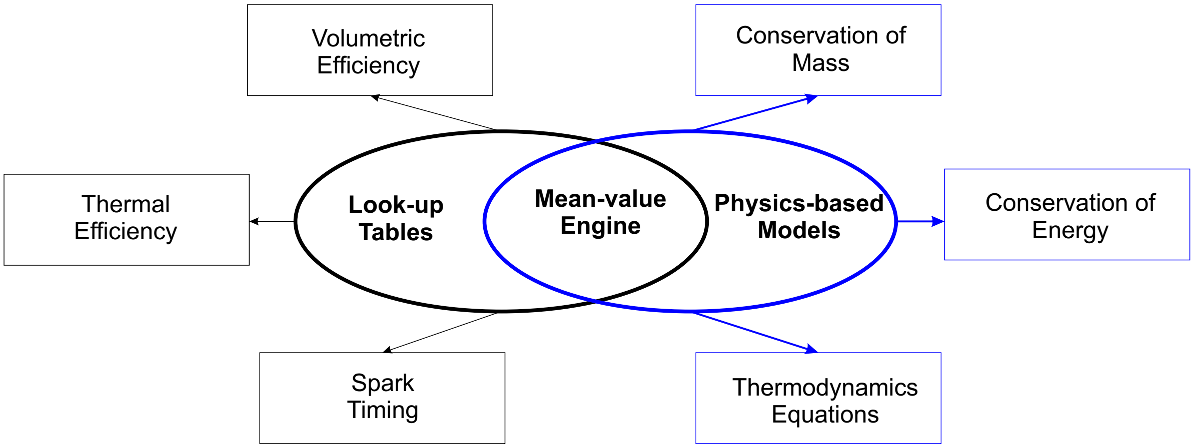

Figure 2.4: Schematic diagram of the MVEM modeling interfaces

Conventionally, IC engine models were represented by empirical data such as look-up tables, which express the IC engine characteristic variables as a function of the engine rotational speeds and torques, or by static math-based models [20,67], which were not able to capture the transient phenomena in the IC engine models.

The dynamic math-based IC engine models have been studied since 1970 [28,39]. These models have been significantly useful to study transient phenomena such as fuel dynamics, manifold pressure and temperature variations, air/fuel ratio (AFR) changes, and throttle angle effects.

Powell [66] introduced a basic nonlinear model of an engine dynamics system. The model includes engine dynamics, intake manifold dynamics, throttle dynamics, fuel injection dynamics, and exhaust-gas-recirculation (EGR) system. The dynamics of the components are represented by simple first order differential equations. The overall model is rewritten in the form of nonlinear state space equations for control purposes.

Aquino [10] was among the first researchers to develop a math-based fuel dynamics model in an IC engine model. He introduced the wall-wetting phenomena by assuming that a portion of the injected fuel is left on the port walls and would be evaporated after some delay time. In Aquino's math-based engine model, the fuel dynamics variables are expressed as a function of the manifold pressure and the engine speed.

Dobner [27, 28] represented a math-based SI engine model with the carburetor model. The carburetor model, which is used to control the air and the fuel flow in to the engine, is represented by look-up tables as a function of the manifold pressure, the air/fuel ratio, and the throttle angle. The engine model contains four sub-models (Figure 2.5) which are the carburetor, the intake manifold, the combustion, and the engine rotational dynamics models.

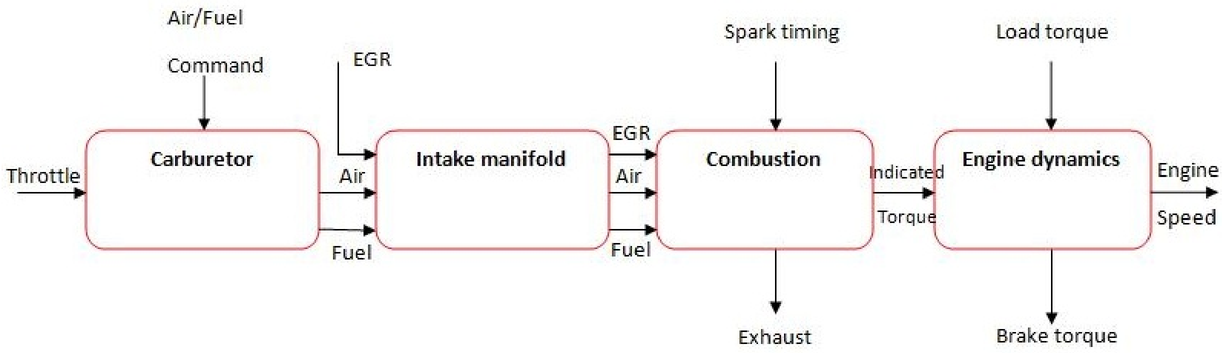

Figure 2.5: SI model structure in [28]

Yuen and Servati [89] presented a simple math-based model of emission gases in the MVEM. The emission gases such as CO and NO_x are formulated as a function of air/fuel ratio of the combustion mixture.

The most well-known version of the MVEM was introduced by Hendricks and Sorenson in 1990 [42]. The model in this paper, which is a simple model of a four cylinder SI engine, has three main states (three differential equations): the engine speed, manifold pressure, and air mass flow rate. The instantaneous engine variables are expressed as a function of the main state variables. For instance, the thermal efficiency and volumetric efficiency are represented by look-up data as a function of the engine speed and the manifold pressure. The simulation results show reasonable agreement with experimental data in the entire operating range of the SI engine, with the accuracy of most variables within less than 2% of the experimental results. The major developments of the MVEM have been accomplished by Hendricks et al. since 1990 [43, 44].

Saeedi [71] developed a mean-value engine model in MapleSim software and validated against the experimental results. The model includes several sub-models such as: speed controller (driver model), throttle body, intake manifold, and engine (cylinder) model. The developed mean-value engine model by Saeedi is expanded and integrated along with automatic transmission and vehicle longitudinal dynamics in a driveline [3, 7].

2.2.2 Spark ignition (SI) engine and combustion model

The mean-value engine model (MVEM), which is widely used in model-based control applications, is partially a physics-based SI engine model, but detailed physical phenomena such as the combustion model, including fuel chemical kinetics, and the emission model cannot be represented by the MVEM.

Combustion modeling plays an important role in modeling an SI engine which contains the detailed chemical kinetics during the combustion process, the released chemical energy, and the emission gases. The combustion in the SI engine happens just before the end of the compression stroke, extends through the combustion stroke, and ends after the peak cylinder pressure occurs [45].

The mathematical models of spark ignition engines, from a thermodynamics point of view, can be categorized into single zone and multi-zone models. In the single zone model the fuel composition, temperature, and pressure are assumed to be uniform in the cylinder. The multi-zone model is a more realistic model which contains the burned and unburned regions [68]. Considering more zones in the combustion chamber increases the number of calculations, but the results can be more realistic, specifically in the case of evaluating the formation of emissions [19, 74, 77].

In multi-zone models (e.g. two zones) the combustion chamber is divided into burned and unburned zones. Each zone has different properties in terms of composition, temperature, and pressure distribution. Essentially the equations are based on conservation of mass and energy which are used to calculate the cylinder thermodynamic state variables (e.g. cylinder pressure) [68]. The two-zone thermodynamic assumptions and mathematical derivations are mentioned in the next section.

Benson et al. [18] studied a comprehensive simulation model of a four stroke SI engine model. The proposed model simulated a full power cycle and gas dynamic model in the exhaust pipe. Moreover, the simulations can predict NO_x emissions. In their work, a two zone combustion model is employed to simulate ignition (expansion) stroke. Equations of each stroke (e.g. compression, ignition, and expansion) are derived and combustion kinetics is used to model NO_x emissions along the exhaust pipe. The simulation results show good agreement with experimental results.

Blumberg et al [21] were among the first researchers that presented a physics-based SI engine model. They described the SI engine complex structure as a group of separate physically-based sub-models that are phenomenologically important. In other words, the sub-models are presented based on fundamental physical formulations (e.g. conservation of mass and energy) in a suitable way that can depict the phenomena in the proposed sub-model.

Bayraktar [15] and Bayraktar and Durgun [16] developed a SI engine cycle with a combustion model as a flame propagation process. The model is based on a two-zone combustion model, and all four strokes are mathematically formulated. The pressure and temperature variations of the proposed math-based model show good agreement with the experimental results for different engines (e.g. Figure 2 compares the theoretical pressure variation with experiments). Although their math-based SI engine model can well predict power, temperature, and pressure in a cylinder, it could not predict emissions (no chemical kinetics is included in the model).

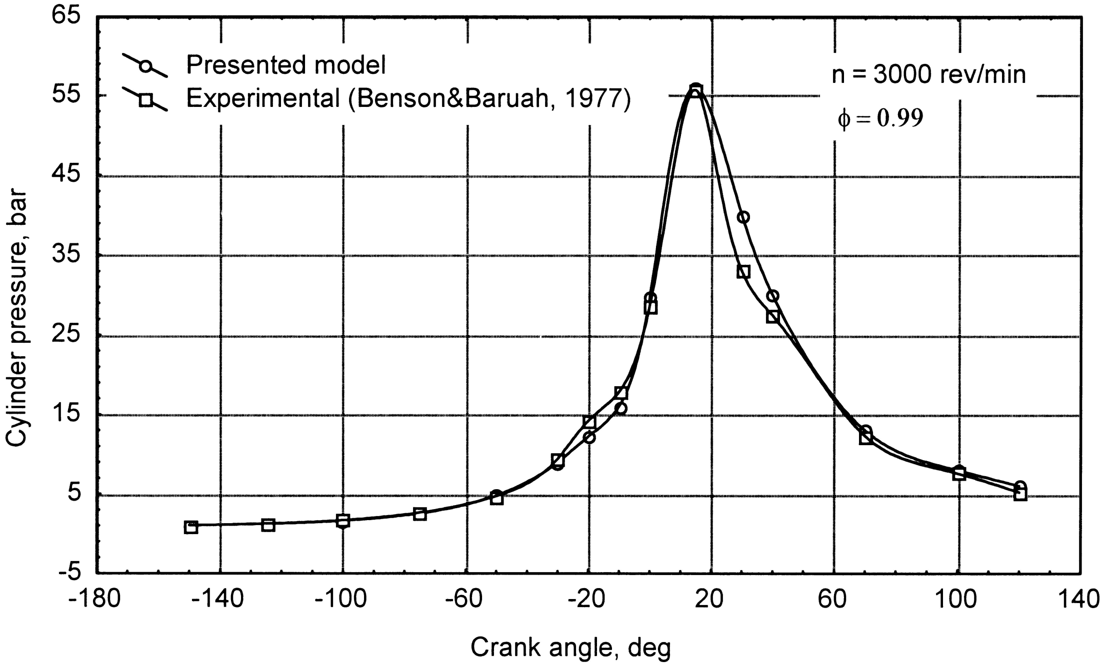

Figure 2.6: Pressure variations of the math-based model vs. experimental results [15]

Verhelst and Sheppard [82] presented a critical overview of SI engine combustion modeling using a multi-zone approach. The authors mentioned that choosing multi-zone model is largely dictated by the applications of the proposed engine model. For instance, if the goal of the SI engine model is to simulate the engine characteristics in a wide range of operation and to evaluate the effect of engine parameters on the engine performance with a reasonable level of accuracy, then a multi-zone model is recommended.

The two-zone SI engine combustion model has been simulated in Matlab/Simulink [76] and Modelica/Dymola [61]. The combustion models, in these works, include physical and thermodynamic formulations to simulate the generated power, but they did not include integrated model of combustion chemical kinetics to predict emissions.

The developed physics-based SI engine model, in this dissertation (Chapter 4), is based on the two-zone combustion with turbulent flame prorogation approach. The unique features of the proposed physics-based model are:

- The SI engine model in MapleSim is able to capture many cycles simulation with quite fast simulation time (real time simulation), which makes the model suitable for model-based control development.

- The parametric (math-based) development of the model allows the user to manipulate the math-based model (DAEs) for different purposes (e.g. parametric sensitivity analysis).

- The mechanical part of the multi-domain model is created from the multi-body library of MapleSim which is connected to the rest of the powertrain (Chapter 5) through the acausal flange connection (crankshaft). The whole system can be simulated for a wide range of loads and speeds. Moreover, the model is able to generate simulation for a variable engine speed (updating initial conditions) in one simulation time frame.

Chapter 3

Physics-based Torque Converter Model

In an automobile with an automatic transmission, instead of a mechanical clutch, a torque converter (a type of fluid coupling) can be utilized to transmit the engine's power. The major roles of a torque converter are multiplying torque generated by the engine and absorbing torsional vibration of the engine and powertrain [80].

The torque converter includes three rotating elements: the pump (impeller), the turbine, and the stator as shown in Figure 3.1.

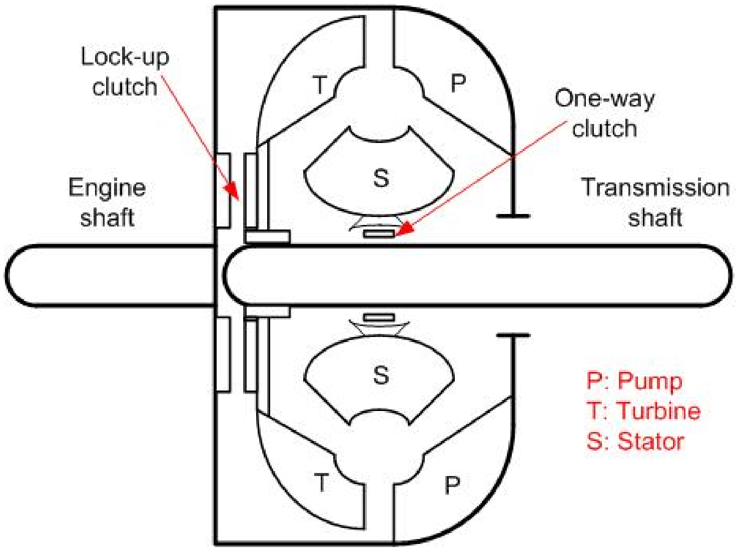

Figure 3.1: Cross section of a torque converter

The pump is attached to the engine shaft, which is called the prime mover, and the turbine is connected to the transmission shaft. The stator, which is placed between the pump and the turbine, redirects the returning fluid from the turbine to the pump. A one-way clutch is used along with the stator to either lock or unlock the stator depending on the fluid direction (whether it hits the front or back of the stator's vanes).

Torque converters can be mathematically modeled by a look-up table, simple algebraic equations, or differential equations. The look-up table model is a simple model based on experimental data and can be easily implemented in a powertrain system model. The simple algebraic equations express the pump's torque and the turbine's torque as a function of the pump and turbine rotational speeds. However both look-up table and algebraic equations do not convey information about torque converter parameters and dynamics, but are fairly suitable models for model-based control design.

The differential equation model of a torque converter, which is represented by four first-order nonlinear differential equations, is suitable to show the transient effect of the torque converter, e.g. the transient behaviour of a vehicle's longitudinal dynamics during gear shifting. Moreover, it can be used to evaluate the effects of the torque converter parameters on the performance. This model is more realistic than simple look-up tables and static models and contains all pump, turbine, and stator dynamics.

3.1 Torque Converter Operating Modes

The following sections presents modelling and simulation of a dynamic torque converter in all operating modes (torque multiplication, coupling, and reverse flow modes) in the MapleSim environment [56].

3.1.1 Forward Flow Operation

In the forward flow mode operation, which is usually used to simulate torque converters, the pump side (connected to the engine shaft) is the driver shaft and the turbine shaft is the driven shaft (load). In this mode the flow direction is positive and the speed ratio (the ratio of the turbine speed to the pump speed) is always less than one.

The torque converter forward operation can be explained using the "coupling point", which is defined based on the stator torque (τ_s). In the torque multiplication range, below the coupling point, the stator is fixed and its rotational speed (w_s) is zero. In the coupling range, which happens after the coupling point, the stator freely rotates and the stator torque is zero. The coupling point occurs when the turbine angular speed typically reaches to 90% of the pump angular speed [47]. At this point, the algebraic summation of the pump, turbine, and stator torques are almost zero, and the ratio between turbine torque and pump torque approaches unity. In the multiplication mode, which operates below the coupling point, the property of the fluid coupling helps to multiply the engine's torque to accelerate the vehicle. On the other hand, when the speed ratio reaches the coupling point value, the turbine torque is almost the same as the transmitted torque from the engine.

The torque converter model in this section is based on four first-order differential equations, given in [47], which are implemented as a "custom components" in the MapleSim software.

$$I_p\dot{w}_p + \rho_{TC}S_p\dot{Q}_{TC} = -\rho_{TC}\left(w_p r_p^2 + r_p\frac{Q_{TC}}{A_{TC}}\tan(\alpha_p) - w_s r_s^2 - r_s\frac{Q_{TC}}{A_{TC}}\tan(\alpha_s)\right)Q_{TC} + \tau_p \tag{3.1}$$

$$I_t\dot{w}_t + \rho_{TC}S_t\dot{Q}_{TC} = -\rho_{TC}\left(w_t r_t^2 + r_t\frac{Q_{TC}}{A_{TC}}\tan(\alpha_t) - w_p r_p^2 - r_p\frac{Q_{TC}}{A_{TC}}\tan(\alpha_p)\right)Q_{TC} + \tau_t \tag{3.2}$$

$$I_s\dot{w}_s + \rho_{TC}S_s\dot{Q}_{TC} = -\rho_{TC}\left(w_s r_s^2 + r_s\frac{Q_{TC}}{A_{TC}}\tan(\alpha_s) - w_t r_t^2 - r_t\frac{Q_{TC}}{A_{TC}}\tan(\alpha_t)\right)Q_{TC} + \tau_s \tag{3.3}$$

$$\begin{aligned}
&\rho_{TC}(S_p\dot{w}_p + S_t\dot{w}_t + S_s\dot{w}_s) + \rho_{TC}\frac{L_f}{A_{TC}}\dot{Q}_{TC} = \rho_{TC}(r_p^2w_p^2 + r_t^2w_t^2 + r_s^2w_s^2\\
&- r_s^2w_pw_s - r_p^2w_tw_p - r_t^2w_sw_t) + w_p\frac{Q_{TC}}{A_{TC}}\rho_{TC}(r_p\tan(\alpha_p) - r_s\tan(\alpha_s))+\\
&w_t\frac{Q_{TC}}{A_{TC}}\rho_{TC}(r_t\tan(\alpha_t) - r_p\tan(\alpha_p)) + w_s\frac{Q_{TC}}{A_{TC}}\rho(r_s\tan(\alpha_s) - r_t\tan(\alpha_t)) - P_L
\end{aligned} \tag{3.4}$$

Equations 3.1, 3.2, 3.3, and 3.4 are the pump, turbine, stator angular momentum and conservation of energy (including power loss P_L) equations respectively, which are implemented in a custom component block (Figure 3.2). The pump torque (τ_p) and the turbine torque (τ_t) are the inputs of the custom component block, and the stator torque is represented by τ_s in Equation 3.3. The states of the model are pump angular speed (w_p), turbine angular speed (w_t), stator angular speed (w_s), and volumetric flow rate (Q_{TC}). The definition and values of the torque converter parameters are listed in Table 3.1.

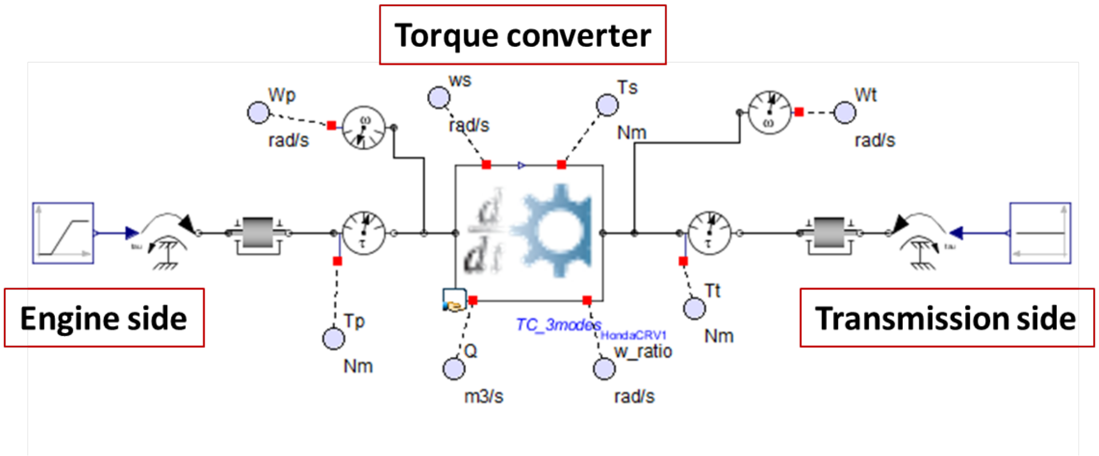

Figure 3.2: Torque converter model in MapleSim environment

The stator torque (τ_s) is used as a switching criterion. In the multiplication range the stator is fixed and the rotational speed (w_s) is zero. In the coupling range the stator freely rotates and the stator torque is zero (e.g. threshold=0.1 N.m) (Equation 3.5).

$$0 = \begin{cases} w_s & \text{threshold} \leq \tau_s \\ \tau_s & \text{otherwise} \end{cases} \tag{3.5}$$

Table 3.1: Nominal values of the torque converter parameters of Honda CRV [65]

Fluid density (ρ_{TC})	840 kg/m^3	Turbine inertia (I_t)	0.026 $kg.m^2$
Flow area (A_{TC})	0.0097 m^2	Stator inertia (I_s)	0.012 $kg.m^2$
Pump radius (r_p)	0.11 m	Fluid inertia length (L_f)	0.28 m
Turbine radius (r_t)	0.066 m	Shock loss coefficient (C_{sh})	1
Stator radius (r_s)	0.06 m	Frictional loss coefficient (C_f)	0.25
Pump exit angle (α_p)	0 deg	Pump design constant (S_p)	-0.001 m^2
Turbine exit angle (α_t)	-59.04 deg	Turbine design constant (S_t)	-0.00002 m^2
Stator exit angle (α_s)	65 deg	Stator design constant (S_s)	0.002 m^2
Pump inertia (I_p)	0.092 $kg.m^2$		

This strategy is used to solve the aforementioned set of differential equations. In other words, before the coupling point the stator angular speed (w_s) is set to zero and there are three differential equations (for w_p, w_t, Q_{TC}) and one algebraic equation (for τ_s). The algebraic equation, which is the stator equation in the torque multiplication range, is used to calculate the stator torque (τ_s). The coupling point happens when the stator torque goes below the threshold value and the coupling range is started at this point. In the coupling range, the aforementioned set of four differential equations are solved for w_p, w_s, w_t, and Q_{TC}. The stator torque and angular speed are shown in Figure 3.3. These plots clearly illustrate the coupling point definition, and the concept of the torque multiplication range (when the stator is fixed) and coupling range (when the stator freely rotates).

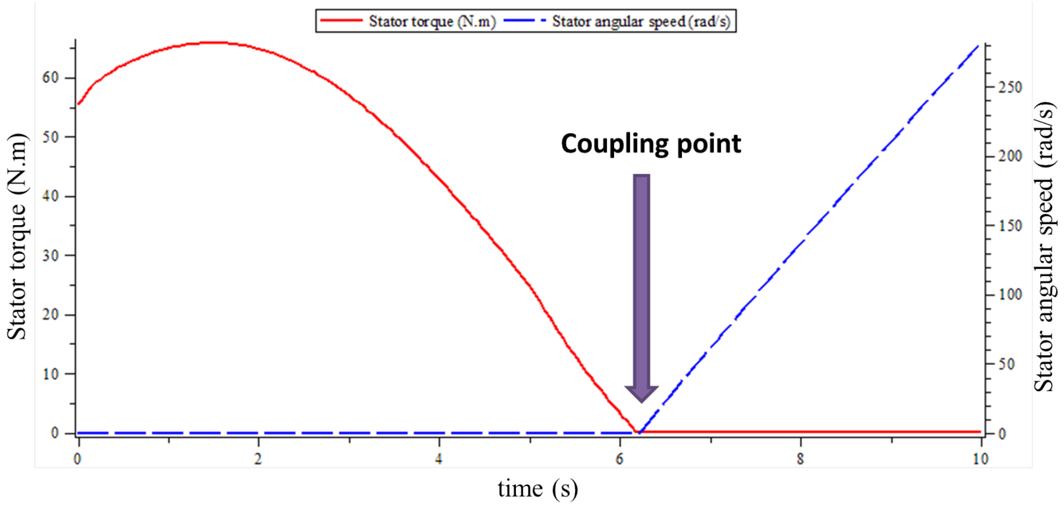

Figure 3.3: Stator torque and angular speed

The torque converter model is validated during forward flow in both multiplication and coupling modes. The simulation results are based on steady state calculations. In other words, all derivative terms are set to zero in Equations 3.1, 3.2, 3.3, and 3.4.

Characteristic plots for torque ratio ($\frac{\tau_t}{\tau_p}$) and capacity factor ($\frac{w_p}{\sqrt{\tau_p}}$) are compared with the corresponding experimental results for the Honda CRV torque converter [65], as shown in Figure 3.4 and Figure 3.5. Although there are small differences between the simulation and experimental results, the agreement is reasonable, and the qualitative performance of the model is clearly representative of an actual torque converter.

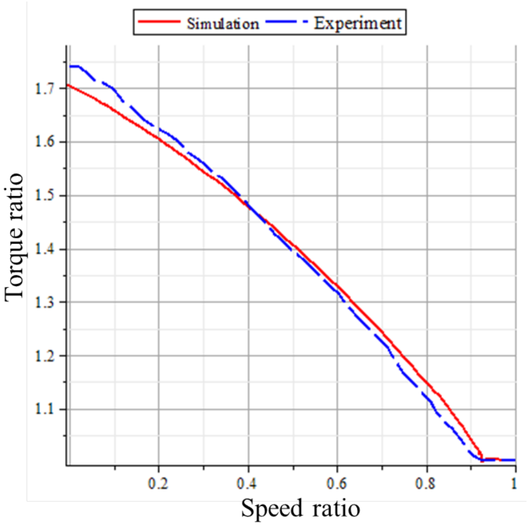

Figure 3.4: Torque ratio simulation and experimental results

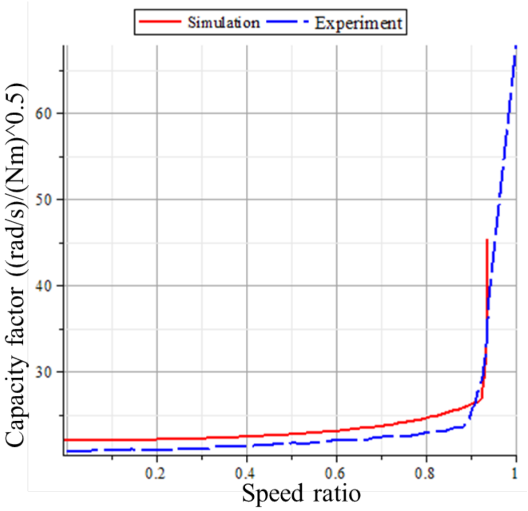

Figure 3.5: Capacity factor simulation and experimental results

3.1.2 Reverse Flow Operation

In this mode, which happens during the engine braking or coasting, the turbine drives the pump shaft, the flow direction is reversed, and the speed ratio exceeds one [47].

The dynamic equations of the torque converter, in forward flow operation, are slightly changed to represent the reversed flow mode equations. The main changes are in the blade angles (entrance and exit angles) and the angular speeds. The dynamic equations of this mode are listed in Equations 3.6, 3.7, 3.8, and 3.9. In the literature, to the best knowledge of the author, the torque converter simulation during the reverse flow mode and the transition from the forward flow mode to the reverse flow mode operations have not been studied. The transition from the forward flow mode to the reverse flow mode happens when the speed ratio exceeds one due to the sudden sharp increase in the turbine angular speed and/or pump angular speed drop.

$$I_p\dot{w}_p + \rho_{TC}S_p\dot{Q}_{TC} = -\rho_{TC}\left(w_t r_p^2 + r_p\frac{Q_{TC}}{A_{TC}}\tan(\alpha_t) - w_p r_s^2 - r_s\frac{Q_{TC}}{A_{TC}}\tan(\alpha_p)\right)Q_{TC} + \tau_p \tag{3.6}$$

$$I_t\dot{w}_t + \rho_{TC}S_t\dot{Q}_{TC} = -\rho_{TC}\left(w_s r_t^2 + r_t\frac{Q_{TC}}{A_{TC}}\tan(\alpha_s) - w_t r_p^2 - r_p\frac{Q_{TC}}{A_{TC}}\tan(\alpha_t)\right)Q_{TC} + \tau_t \tag{3.7}$$

$$I_s\dot{w}_s + \rho_{TC}S_s\dot{Q}_{TC} = -\rho_{TC}\left(w_p r_s^2 + r_s\frac{Q_{TC}}{A_{TC}}\tan(\alpha_p) - w_s r_t^2 - r_t\frac{Q_{TC}}{A_{TC}}\tan(\alpha_s)\right)Q_{TC} + \tau_s \tag{3.8}$$

$$\begin{aligned}&\rho_{TC}(S_p\dot{w}_p + S_t\dot{w}_t + S_s\dot{w}_s) + \rho_{TC}\frac{L_f}{A_{TC}}\dot{Q}_{TC} = \rho_{TC}(r_p^2 w_t^2 + r_t^2 w_s^2 + r_s^2 w_p^2\\ &- r_s^2 w_p w_s - r_p^2 w_t w_p - r_t^2 w_s w_t) + w_p\frac{Q_{TC}}{A_{TC}}\rho_{TC}(r_p\tan\alpha_t - r_s\tan\alpha_p) +\\ &w_t\frac{Q_{TC}}{A_{TC}}\rho_{TC}(r_t\tan\alpha_s - r_p\tan\alpha_t) + w_s\frac{Q_{TC}}{A_{TC}}\rho_{TC}(r_s\tan\alpha_p - r_t\tan\alpha_s) - P_L\end{aligned} \tag{3.9}$$

The custom component torque converter, along with models of two dynamometers, is shown in Figure 3.6. Dynamometers are electro-mechanical devices that are used to control either the torque or the angular speed of the rotational shaft, and are included in this model to test the torque converter. In this work, the dynamometer is modelled as a permanent magnet DC motor (PMDC) along with a proportional-integral-derivative (PID) controller to control either the torque or angular speed of the shaft. This modelling approach is similar to a physical apparatus used to evaluate torque converter characteristics (SAE J643), based on electric motor/generator dynamometers. The electric motor can produce electric power to drive a mechanical shaft, or can be used as an electric generator by absorbing mechanical power. The MapleSim multi-domain environment provides a good combination of causal (e.g. PID controller) and acausal (e.g. DC motor) components, which helps us to model the proposed virtual test apparatus efficiently.

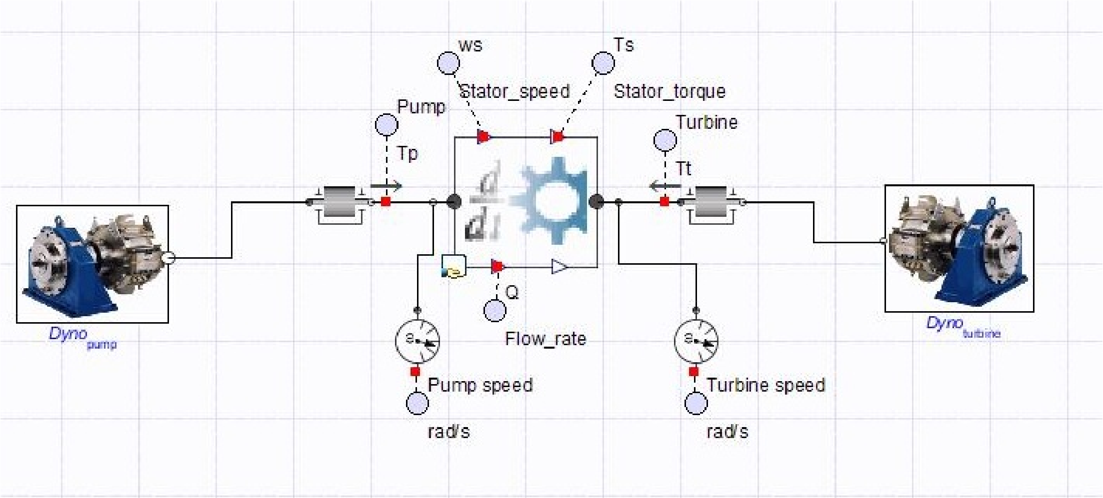

Figure 3.6: Torque converter model with dynamometers

In this simulation, the pump's dynamometer controls the pump torque; the turbine's dynamometer initially controls the turbine torque, and then switches to controlling the turbine speed at a later time. The dynamometer sub-models in MapleSim are shown in Figure 3.7 (from the pump shaft) and Figure 3.8 (from the turbine shaft).

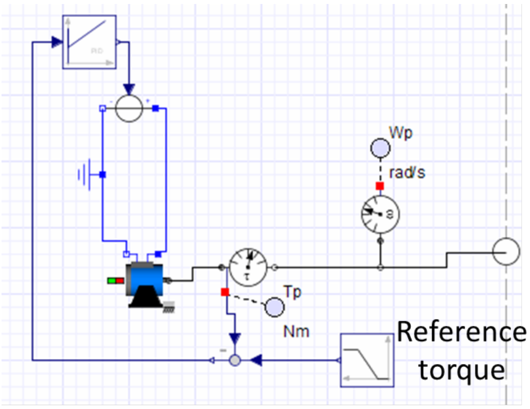

Figure 3.7: Dynamometer (pump side)

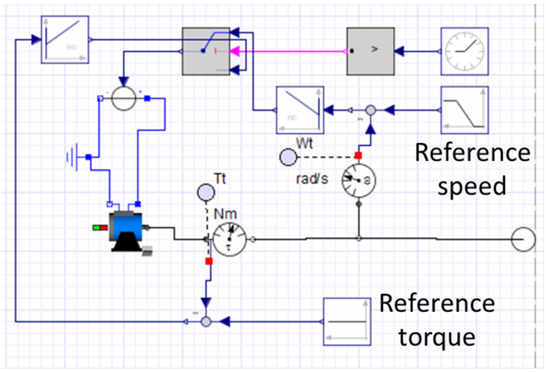

Figure 3.8: Dynamometer (turbine side)

The pump torque is controlled by a PID controller throughout the simulation to follow the reference torque signal, which is a combination of constant and ramp functions, as shown in Figure 3.9. The gains of the PID controller are obtained by trial-and-error, with $K_P = 1$, $K_I = 100$, and $K_D = 0.01$. The output of the PID controller is DC current to run the PMDC motor. The turbine torque (Figure 3.10) is set to $-200 N.m$ in the first period (up to the time $= 10s$), and then it is switched to speed control on turbine angular speed. As expected from the torque results, during the reverse flow mode, the turbine torque value is equal to the pump torque. In other words, in the forward mode the pump's shaft is the driver shaft (motor) and the turbine's shaft is the driven shaft (load/generator), but during the reverse flow mode (started around time $= 11s$) the turbine's shaft is the driver (motor) and the pump's shaft is the driven one.

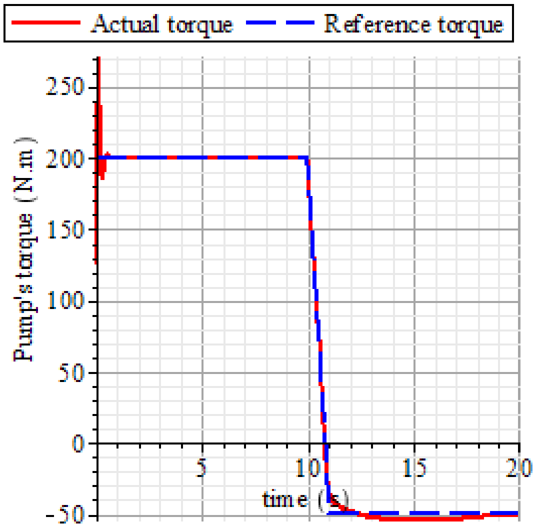

Figure 3.9: Pump torque (forward to reverse mode)

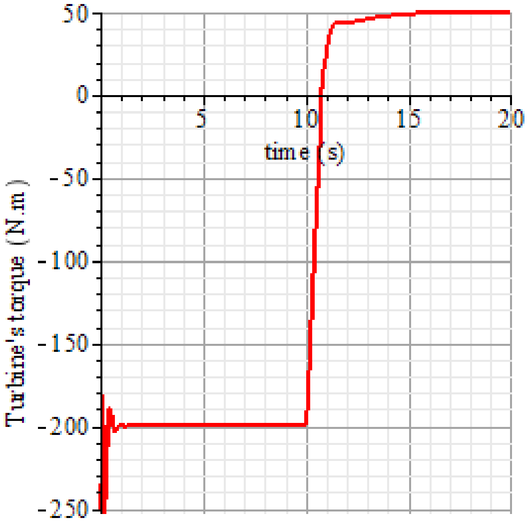

Figure 3.10: Turbine torque (forward to reverse mode)

The simulation results (Figure 3.11 and Figure 3.12) show that the speed ratio remains greater than one and the flow rate direction is reversed during the reverse flow mode.

Using the torque converter in the reverse flow mode during engine braking can help to slow down the vehicle without using an external braking mechanism. This idea will be used, in Section 3.4.2, to simulate the torque converter operation during the flow reversal in the powertrain along with the vehicle longitudinal dynamics to show the engine braking phenomenon.

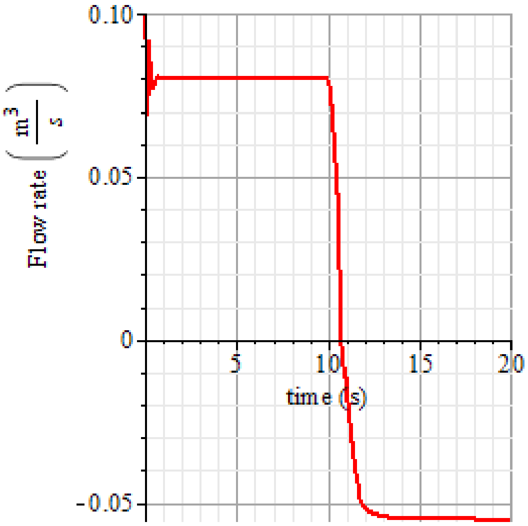

Figure 3.11: Fluid flow rate (forward to reverse mode)

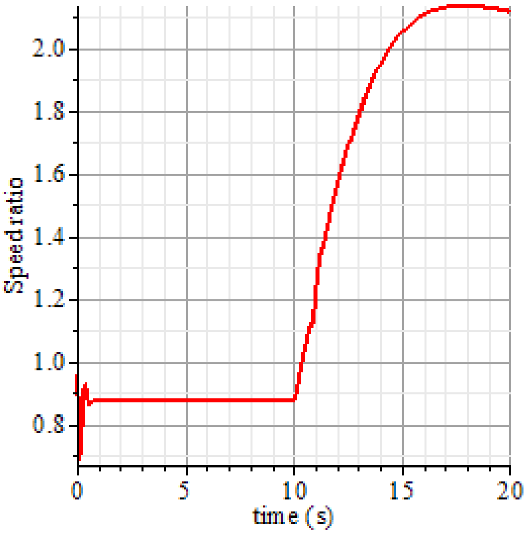

Figure 3.12: Speed ratio (forward to reverse mode)

3.2 Sensitivity Analysis

A sensitivity analysis is used to investigate the effect of the parameters on the torque converter performance characteristics. The effect of the torque converter's parameters is considered in torque converter manufacturing [51]. During the manufacturing process, some errors can affect the geometric dimensions of torque converters such as flow area, blade angles, and radius of the pump, turbine, and stator.

The proposed sensitivity analysis is a simple model of parameter variations (10%, 20%, or 50% below and above the nominal value of the parameter), and shows the effects of these variations on performance characteristics of the torque converter. The main parameters investigated are: flow area, radius, and blade angles of the pump, turbine, and stator.

The flow area (A_{TC}) in the circular path, in the proposed torque converter model, is assumed constant. The capacity factor is more sensitive to flow area variation (Figure 3.14) than the efficiency (Figure 3.13).

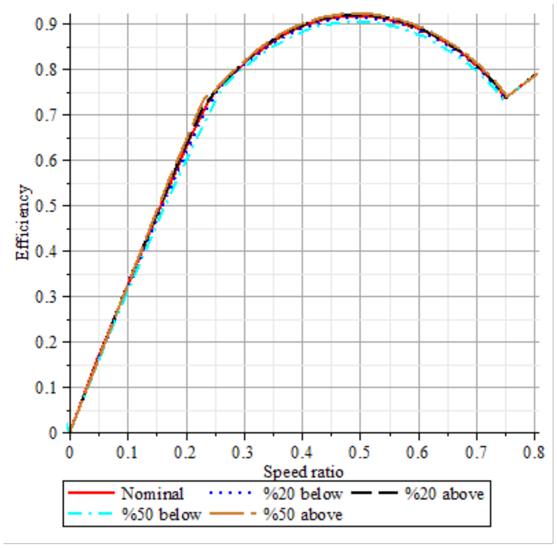

Figure 3.13: Efficiency vs. speed ratio (flow area sensitivity analysis)

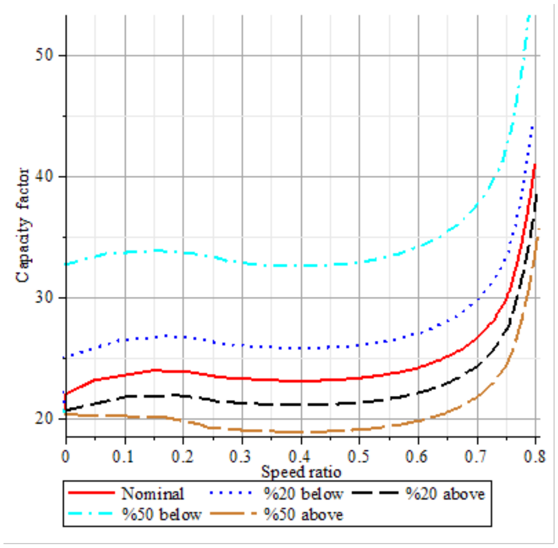

Figure 3.14: Capacity factor vs. speed ratio (flow area sensitivity analysis)

The variation of pump, turbine, and stator radius (r_p, r_t, r_s) show that the pump and stator radius affect the performance characteristic plots more than the turbine radius. Furthermore, the coupling point is displaced. For instance, Figure 3.15 shows that the coupling point occurs at a higher speed ratio by increasing the pump radius, and moves to the lower value by increasing the stator radius (Figure 3.19).

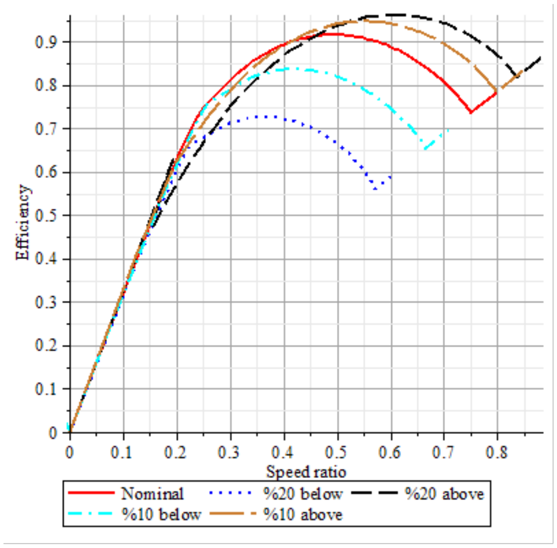

Figure 3.15: Efficiency vs. speed ratio (pump radius sensitivity analysis)

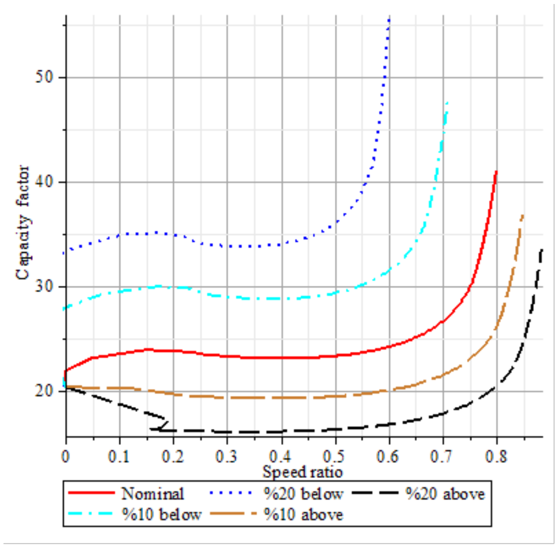

Figure 3.16: Capacity factor vs. speed ratio (pump radius sensitivity analysis)

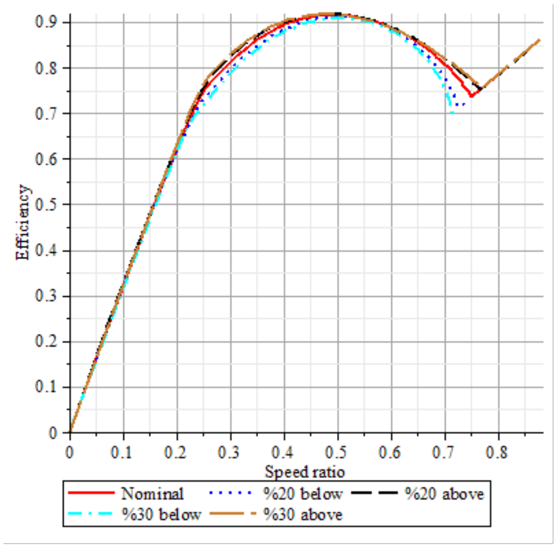

Figure 3.17: Efficiency vs. speed ratio (turbine radius sensitivity analysis)

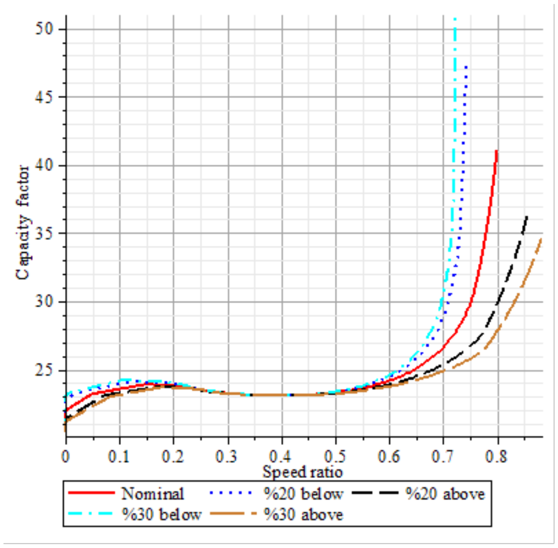

Figure 3.18: Capacity factor vs. speed ratio (turbine radius sensitivity analysis)

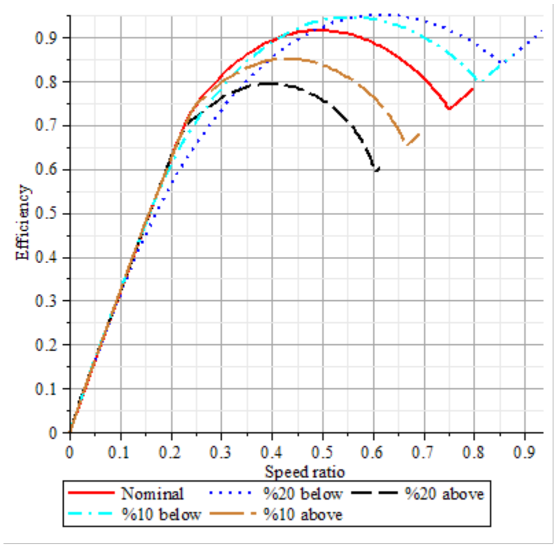

Figure 3.19: Efficiency vs. speed ratio (stator radius sensitivity analysis)

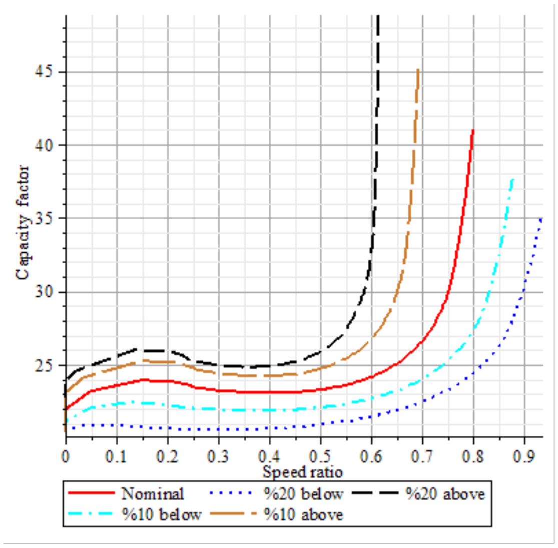

Figure 3.20: Capacity factor vs. speed ratio (stator radius sensitivity analysis)

The nominal value of the pump blade angle is set to zero in this study. Therefore the variation of this parameter, based on the proposed sensitivity analysis, is not considered. The efficiency (Figures 3.21 and 3.23) and capacity factor (Figures 3.22 and 3.24) plots show that increasing the blade angles (α_t and α_s) from the nominal values affect torque converter performance characteristics more than reducing the blade angles.

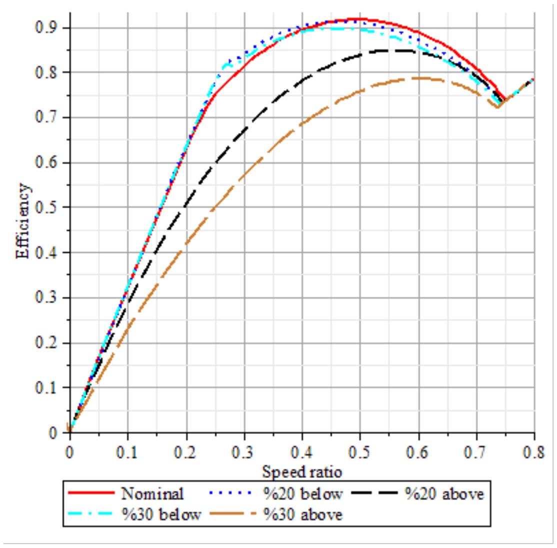

Figure 3.21: Efficiency vs. speed ratio (turbine exit blade angle sensitivity analysis)

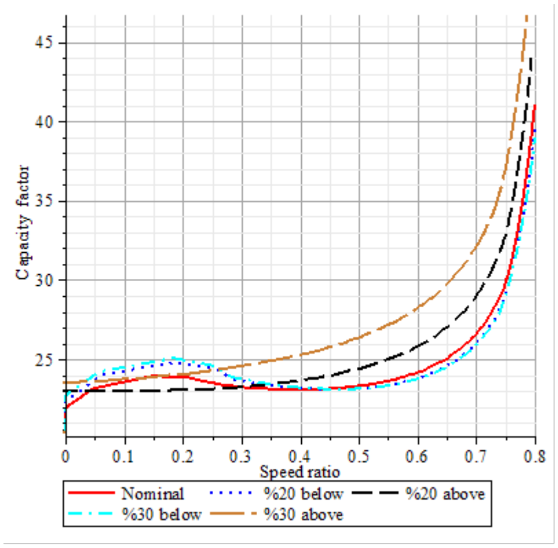

Figure 3.22: Capacity factor vs. speed ratio (turbine exit blade angle sensitivity analysis)

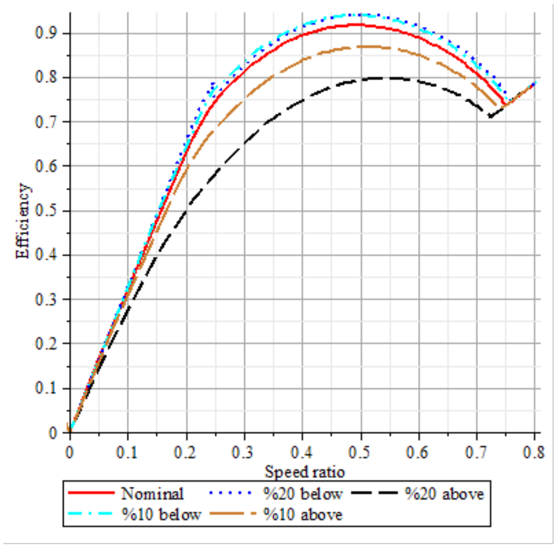

Figure 3.23: Efficiency vs. speed ratio (stator exit blade angle sensitivity analysis)

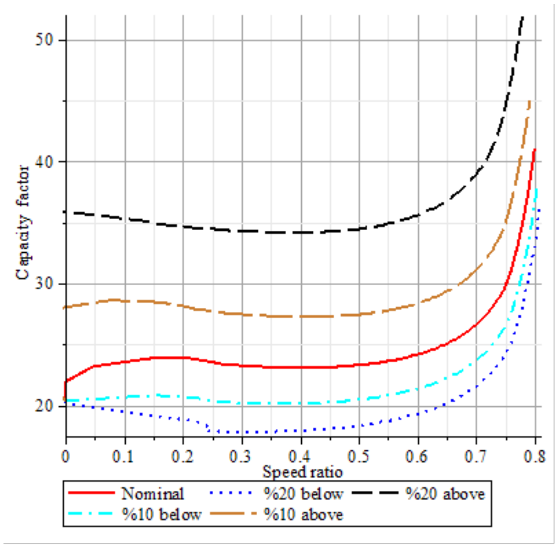

Figure 3.24: Capacity factor vs. speed ratio (stator exit blade angle sensitivity analysis)

The sensitivity analysis results show that:

- The capacity factor is more sensitive than efficiency to the torque converter flow area.
- Both the capacity factor and efficiency are extremely sensitive to the radius of the pump and stator. Furthermore, the coupling point is influenced by radius variations.
- Blade angle variations have significant effects on capacity factor and efficiency plots.

3.3 Damping Characteristics

In this section, torque converter damping characteristics are evaluated in three modes: the torque multiplication mode (before coupling point), the coupling mode (after coupling point), and the reverse flow mode. In the first step, the torque converter equations are linearized to obtain system transfer functions and then the bode diagram of the transfer functions are used to evaluate damping characteristics.

3.3.1 Linearization

The Jacobian linearization technique [12] is employed to linearize the nonlinear equations around equilibrium points. Maple software is employed for this purpose, since it offers a very powerful environment to deal with symbolic equations.

The torque converter equations are linearized in the torque multiplication mode, before coupling point, in which the stator is stationary due to the one-way clutch. Therefore, the stator dynamic equation (Equation 3.3) can be neglected and there are three nonlinear first-order differential equations (Equations 3.1, 3.2, and 3.4). A similar approach can be used for the coupling mode, after coupling point, and the reverse flow mode operation. The linearized Equations 3.10, 3.11, and 3.12 are:

$$\begin{aligned} I_p\dot{w}_p + \rho_{TC} S_p \dot{Q}_{TC} = {}& \left(\frac{\partial f_1(w_p, w_t, Q_{TC})}{\partial w_p}\right)_{EP} (w_p - w_{pe}) + \left(\frac{\partial f_1(w_p, w_t, Q_{TC})}{\partial w_t}\right)_{EP} (w_t - w_{te}) \\ &+ \left(\frac{\partial f_1(w_p, w_t, Q_{TC})}{\partial Q_{TC}}\right)_{EP} (Q_{TC} - Q_{TCe}) + (\tau_p - \tau_{pe}) \end{aligned} \tag{3.10}$$

$$\begin{aligned} I_t\dot{w}_t + \rho_{TC} S_t \dot{Q}_{TC} = {}& \left(\frac{\partial f_2(w_p, w_t, Q_{TC})}{\partial w_p}\right)_{EP} (w_p - w_{pe}) + \left(\frac{\partial f_2(w_p, w_t, Q_{TC})}{\partial w_t}\right)_{EP} (w_t - w_{te}) \\ &+ \left(\frac{\partial f_2(w_p, w_t, Q_{TC})}{\partial Q_{TC}}\right)_{EP} (Q_{TC} - Q_{TCe}) + (\tau_t - \tau_{te}) \end{aligned} \tag{3.11}$$

$$\begin{aligned} \rho_{TC}(S_p\dot{w}_p + S_t\dot{w}_t) + \rho_{TC}\frac{L_f}{A_{TC}}\dot{Q}_{TC} = {}& \left(\frac{\partial f_3(w_p, w_t, Q_{TC})}{\partial w_p}\right)_{EP} (w_p - w_{pe}) \\ &+ \left(\frac{\partial f_3(w_p, w_t, Q_{TC})}{\partial w_t}\right)_{EP} (w_t - w_{te}) + \left(\frac{\partial f_3(w_p, w_t, Q_{TC})}{\partial Q_{TC}}\right)_{EP} (Q_{TC} - Q_{TCe}) \end{aligned} \tag{3.12}$$

The subscript (EP) means that the partial derivative is evaluated at an equilibrium point where $(w_p, w_t, Q_{TC}) = (w_{pe}, w_{te}, Q_{TCe})$ and the functions $f_1(w_p, w_t, Q_{TC})$, $f_2(w_p, w_t, Q_{TCe})$, and $f_3(w_p, w_t, Q_{TC})$ represent the nonlinear, with respect to the state variables, part of the Equations 3.1, 3.2, and 3.4. The equilibrium values and transfer functions are shown in Table 3.2.

The simulation results for the pump speed (Figure 3.25), the turbine speed (Figure

Table 3.2: Equilibrium points and transfer functions

Operation	**Equilibrium Point**	**Transfer Function**
Before coupling point	$\tau_{pe} = 100\ N.m$	$G_{pp} = \frac{\Delta w_p}{\Delta \tau_p} = \frac{1.28s(s+11)(s+415.85)}{(s+5.93)(s+15.80)(s+410.97)}$
	$\tau_{te} = -150\ N.m$	$G_{tp} = \frac{\Delta w_t}{\Delta \tau_p} = \frac{0.00003s(s+881.39)(s+935000)}{(s+5.93)(s+15.80)(s+410.97)}$
	$w_{pe} = 207\ rad/s$	$G_{pt} = \frac{\Delta w_p}{\Delta \tau_t} = \frac{0.00003s(s-12884)(s-1603.34)}{(s+5.93)(s+15.80)(s+410.97)}$
	$w_{te} = 207\ rad/s$	$G_{tt} = \frac{\Delta w_t}{\Delta \tau_t} = \frac{4.57s(s+10.61)(s+414.51)}{(s+5.93)(s+15.80)(s+410.97)}$
After coupling point	$\tau_{pe} = 150\ N.m$	$G_{pp} = \frac{\Delta w_p}{\Delta \tau_p} = \frac{1.3(s+347)(s+15.58+21.36I)(s+15.58-21.36I)}{(s+338)(s+23.42+24.29I)(s+23.42-24.29I)}$
	$\tau_{te} = -150\ N.m$	$G_{tp} = \frac{\Delta w_t}{\Delta \tau_p} = \frac{0.00003(s+11.13)(s+814)(s+1015276)}{(s+338)(s+23.42+24.29I)(s+23.42-24.29I)}$
	$w_{pe} = 223\ rad/s$	$G_{pt} = \frac{\Delta w_p}{\Delta \tau_t} = \frac{0.00003(s+49.73)(s-2268)(s-74189)}{(s+338)(s+23.42+24.29I)(s+23.42-24.29I)}$
	$w_{te} = 205\ rad/s$	$G_{tt} = \frac{\Delta w_t}{\Delta \tau_t} = \frac{4.3(s+359)(s+8.42+11.96I)(s+8.42-11.96I)}{(s+338)(s+23.42+24.29I)(s+23.42-24.29I)}$
Reverse flow mode	$\tau_{pe} = -150\ N.m$	$G_{pp} = \frac{\Delta w_p}{\Delta \tau_p} = \frac{1.3(s+16.21)(s+136.38)(s+367.47)}{(s+17.86)(s+139.43)(s+364.62)}$
	$\tau_{te} = 150\ N.m$	$G_{tp} = \frac{\Delta w_t}{\Delta \tau_p} = \frac{0.00003(s+29.67)(s+3179)(s+93745)}{(s+17.86)(s+139.43)(s+364.62)}$
	$w_{pe} = 165\ rad/s$	$G_{pt} = \frac{\Delta w_p}{\Delta \tau_t} = \frac{0.00003(s+51.29)(s+673)(s+810000)}{(s+17.86)(s+139.43)(s+364.62)}$
	$w_{te} = 376\ rad/s$	$G_{tt} = \frac{\Delta w_t}{\Delta \tau_t} = \frac{4.5(s+3.1)(s+54.37)(s+430.74)}{(s+17.86)(s+139.43)(s+364.62)}$

3.26), and flow rate (Figure 3.27), show a good agreement between the nonlinear and the linear systems at different equilibrium points in the torque multiplication range.

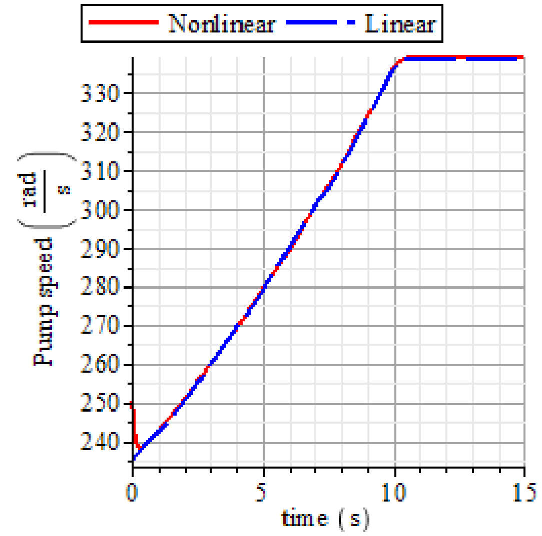

Figure 3.25: Pump angular speed (linear vs. nonlinear)

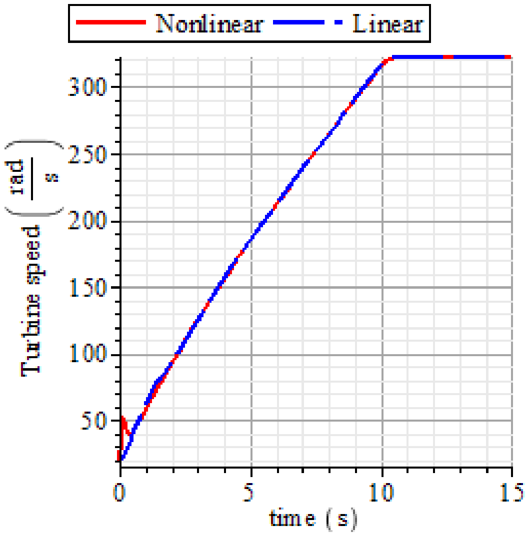

Figure 3.26: Turbine angular speed (linear vs. nonlinear)

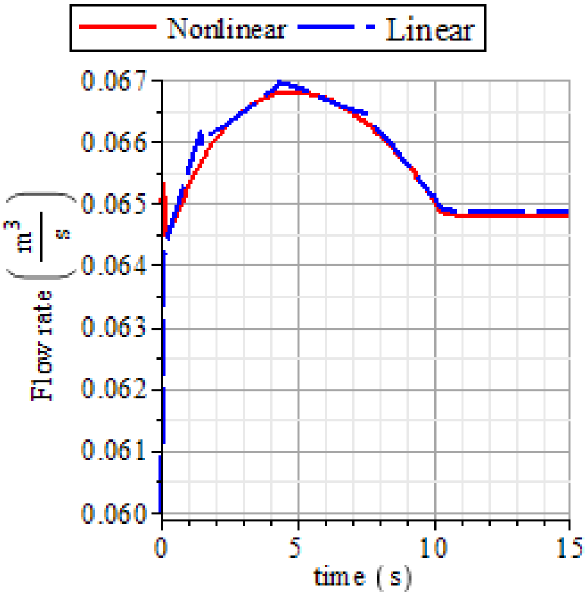

Figure 3.27: Flow rate (linear vs. nonlinear)

3.3.2 Frequency response

One of the main advantages of using a torque converter in an automatic transmission is its capability to filter disturbances [26, 50] introduced either from the engine side, e.g. engine pulsation or overanxious driver, or from the transmission side when the wheels hit road bumps or potholes as shown schematically in Figure 3.28.

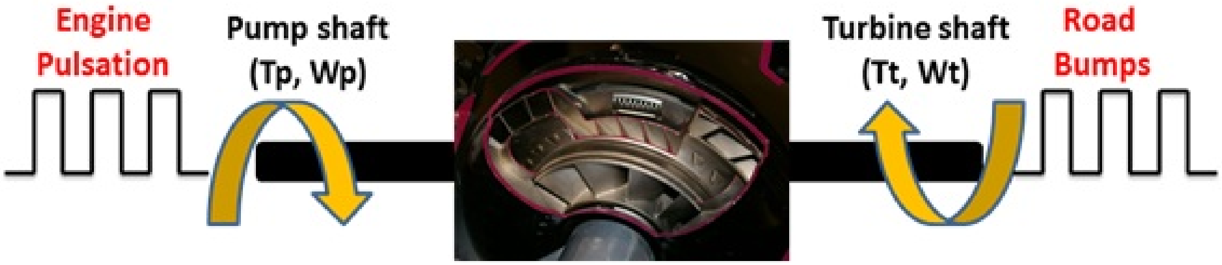

Figure 3.28: Schematic torque converter model subjected to disturbances

The transfer functions of the proposed torque converter model around some equilibrium points for operating before and after coupling point and reverse flow modes are derived and shown in Table 3.2. The transfer functions, which represent the relation between inputs (τ_p and τ_t), and the outputs (w_p and w_t), are normalized with respect to a transmission without a torque converter $G_o(s) = \frac{w(s)}{\tau(s)} = \frac{1}{(I_p+I_s+I_t)s}$. Once normalized with respect to $G_o(s)$, the magnitude of the resulting transfer function provides a comparison of the response with a torque converter to that without a torque converter. In particular, a magnitude less than zero dB at a particular frequency indicates that disturbances at this frequency are attenuated more when a torque converter is present. The gain diagrams (magnitude vs. frequency) of the transfer functions are shown in Figure 3.29 (before coupling point), Figure 3.30 (after coupling point), and Figure 3.31 (reverse flow). One can see that the torque converter significantly damps the high frequency disturbances transferred from the pump to turbine side (G_{pt}), and vice versa (G_{tp}). However, the pump to pump (G_{pp}) and turbine to turbine (G_{tt}) damping performance of the torque converter is worse than the converter-less transmission.

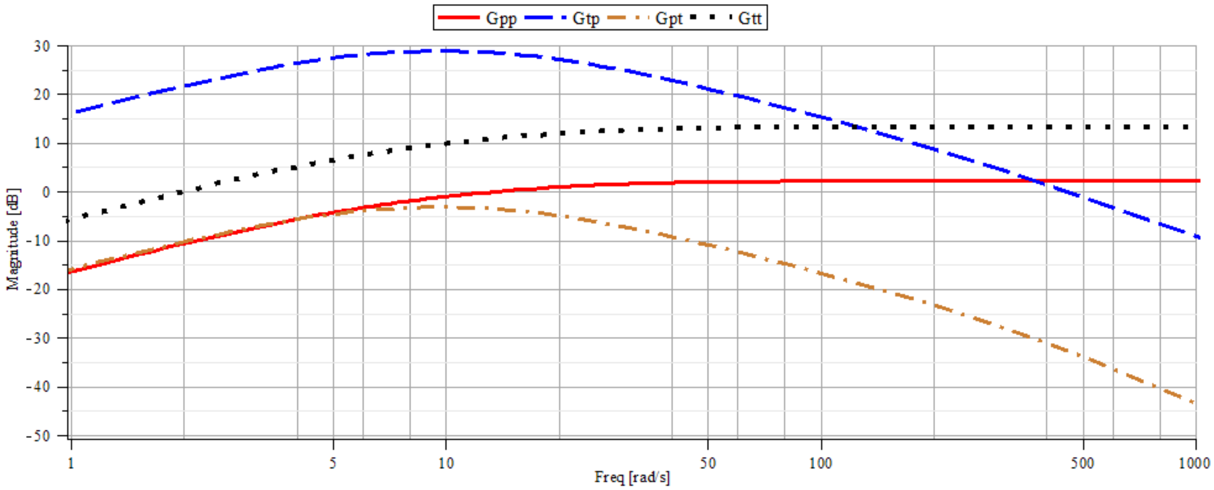

Figure 3.29: Gain diagram (before coupling point mode)

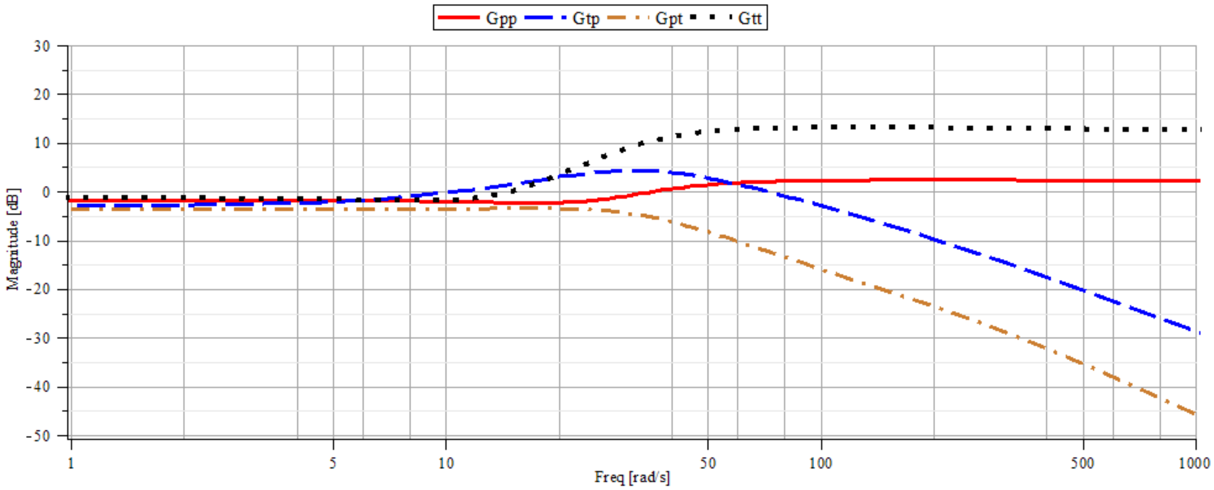

Figure 3.30: Gain diagram (after coupling point mode)

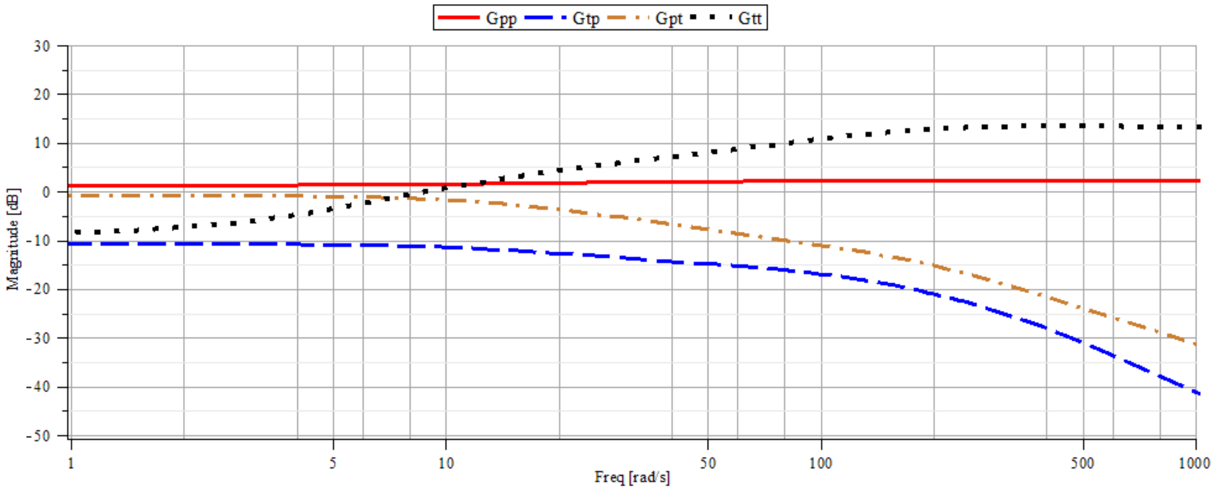

Figure 3.31: Gain diagram (reverse flow mode)

The torque converter frequency response analysis, based on linear equations, shows that the torque converter is working as a low-pass filter to damp disturbances which are transferred from the pump side to the turbine side, and vice versa. The simulation results for the nonlinear torque converter model, which is subjected to a disturbance torque in a wide range of frequencies, confirm the results of linear gain diagrams. For instance, in the forward flow mode operation, the pump torque is given as a combination of a nominal value and disturbances $\tau_p = \tau_{pe} + 10\sin(2\pi f t)$ where the frequency (f) is varied from $0.5(Hz)$ to $100(Hz)$, and the turbine torque is assumed constant $\tau_t = \tau_{te}$. The plots of the pump speed (w_p) and the turbine speed (w_t), Figure 3.32 and Figure 3.33, clearly show the damping characteristics of the torque converter to filter high frequency disturbances (e.g. from pump to turbine side).

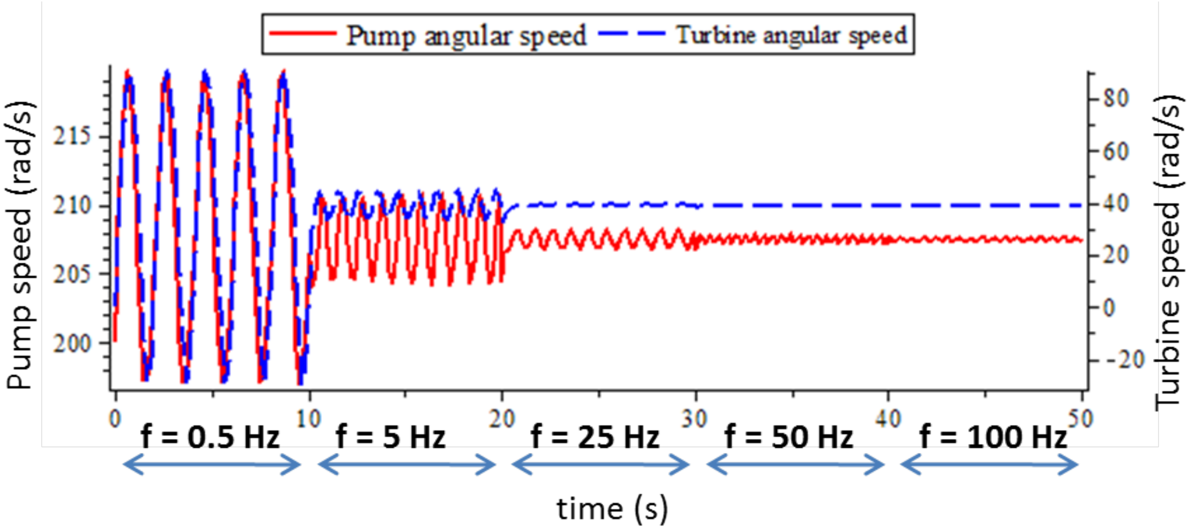

Figure 3.32: Nonlinear model response (before coupling point)

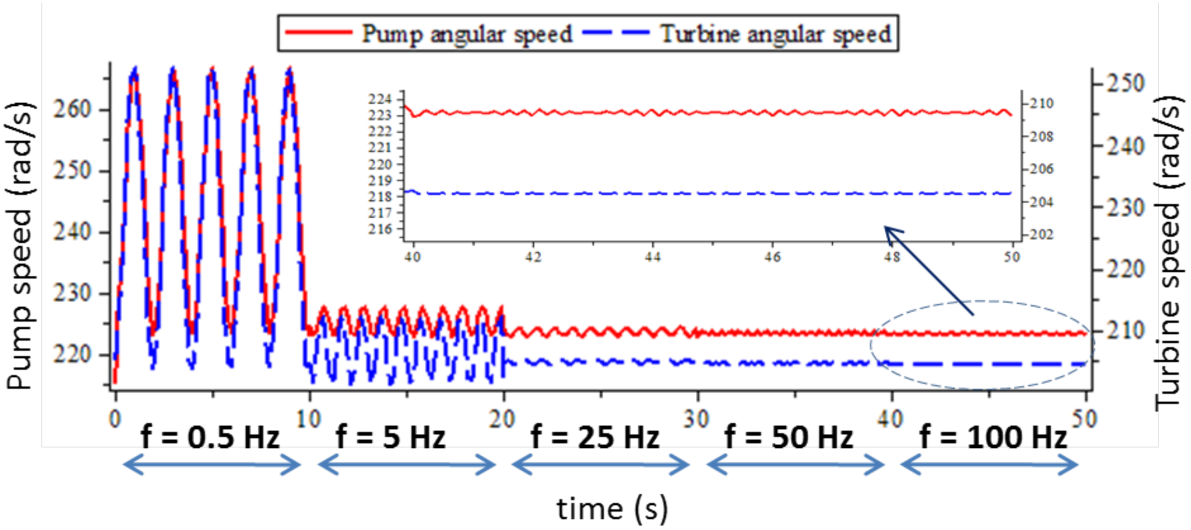

Figure 3.33: Nonlinear model response (after coupling point)

A similar simulation is generated for the reverse flow mode operation. In this case, the turbine torque is assumed to be a disturbance input $\tau_t = \tau_{te} + 10\sin(2\pi f t)$ and the oscillation is transferred from the turbine side to the pump side, and the pump torque is assumed constant $\tau_p = \tau_{pe}$. As expected from the linearized system, the disturbances from the pump side are significantly damped (Figure 3.34), especially at higher frequencies.

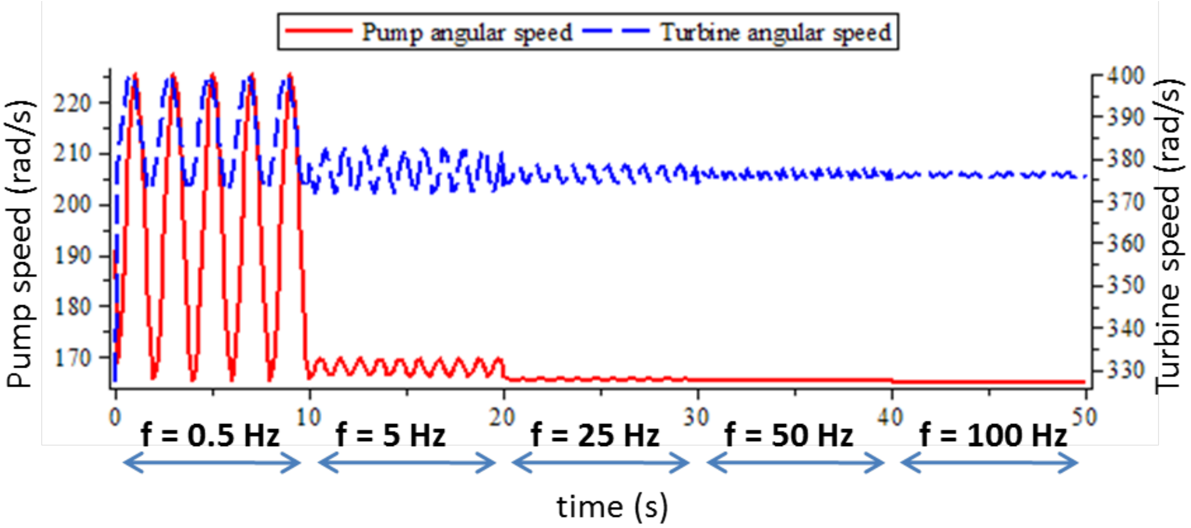

Figure 3.34: Nonlinear model response (reverse flow mode)

3.4 Torque Converter Characteristics in Automatic Driveline

The proposed torque converter model is placed between a mean-value engine model and a transmission shaft, as shown in Figure 3.35. The mean-value engine model has been developed in MapleSim by M. Saeedi [71]. The input to the mean-value engine is a throttle angle controlled by depressing the accelerator pedal, and the outputs are fuel consumption and the mechanical power delivered to the torque converter shaft.

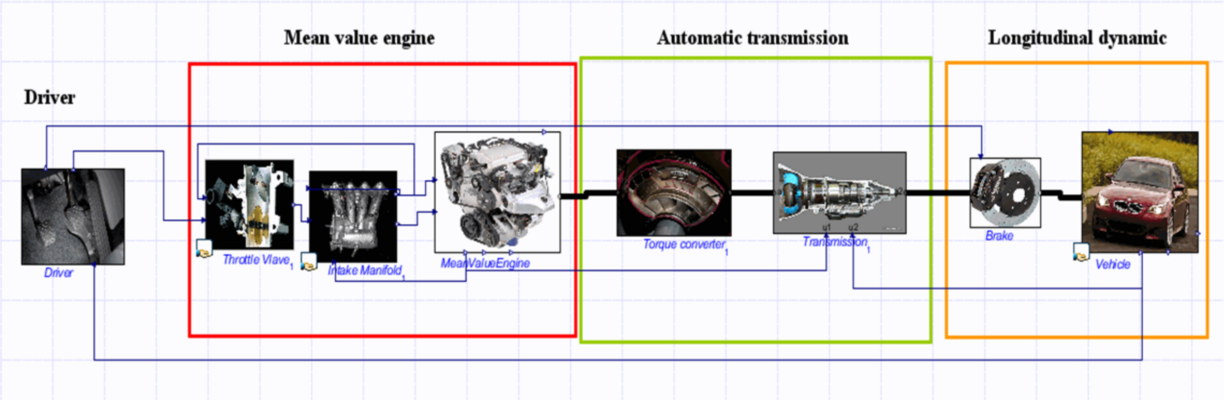

Figure 3.35: Powertrain model in MapleSim including torque converter

The transmission gearbox is modeled as a simple input-output torque with variable gear ratios (G_i) along with the efficiency of each gear (E_i). The input torque to the gearbox is the torque converter turbine torque (τ_{in}) and the output torque (τ_{out}) is multiplied by the final drive ratio to obtain the driving torque. Equations 3.13 and 3.14 represent the gearbox model that is implemented in a custom component block in MapleSim.

$$\tau_{out} = \tau_{in} G_i E_i \tag{3.13}$$

$$w_{in} = G_i w_{out} \tag{3.14}$$

The variation of each gear ratio based on the vehicle forward velocity (km/h) and engine rotational speed (rpm) is listed in Table 3.3.

Table 3.3: Gear ratios and efficiencies

Gear number	**Gear ratio** (G_i)	**Gear efficiency** (E_i)	**Forward velocity** (km/h)	**Engine speed** (rpm)
#1	2.8	0.94	$\nu \leq 15$	$n \leq 1000$
#2	1.6	0.94	$15<\nu<30$	$1000<n$
#3	1.1	1	$30<\nu<50$	$1000<n$
#4	0.8	0.98	$50 \leq \nu$	$1000<n$

The input throttle angle is a ramp function which is started at fully closed throttle angle to the half-opened throttle angle. The longitudinal dynamics sub-model includes vehicle mass, inertia, final drive ratio, and resistance forces such as aerodynamic drag and rolling resistance forces. The details of the powertrain components is provided in Chapter 5. The vehicle parameters are listed in Table 3.4.

Table 3.4: Parameters for a compact sedan

Vehicle mass	1417 kg
Coefficient of rolling resistance	0.012
Coefficient of air drag	0.35
Frontal area	2.58 m^2
Rolling radius of tire	0.3 m
Final drive ratio	3.64
Inertia of engine	0.42 $kg.m^2$
Inertia of wheel and axle	1.5 $kg.m^2$

The proposed powertrain model can be used for different modeling and control purposes. In this section, we evaluate the effects of the torque converter lock-up clutch on the vehicle longitudinal dynamics.

3.4.1 Lock-up Clutch Simulation

In modern automatic transmissions, a lock-up clutch is implemented in the torque converter to lock the engine and the transmission shafts at higher gear ratios (e.g. gear ratios = 3 and 4). The main advantage of using a lock-up clutch mechanism is improving the torque converter efficiency. During the coupling mode, and without a lock-up clutch, the speed ratio and the torque ratio remain around 0.9 and 1 respectively. Therefore the torque converter efficiency, which is defined as products of the speed ratio and the torque ratio, can at most reach 90%. The lock-up clutch mechanism increases the efficiency value to 100% due to the rigid connection between the pump and the turbine shafts. However using the lock-up clutch, the mechanical connection generates some undesirable torque pulses during the clutch engaging, which affects the drivability [40].

As discussed earlier, the power loss due to the torque converter fluid coupling is eliminated in the lock-up clutch model and consequently the powertrain efficiency has been improved in comparison with the torque converter model without the lock-up clutch. The simulation results of the forward velocity (Figure 3.36) show that the lock-up clutch improves the vehicle forward velocity in comparison with the clutch-less torque converter for the same throttle angle profile. However, there is a sharp acceleration peak due to the lock-up clutch engagement as shown in Figure 3.37.

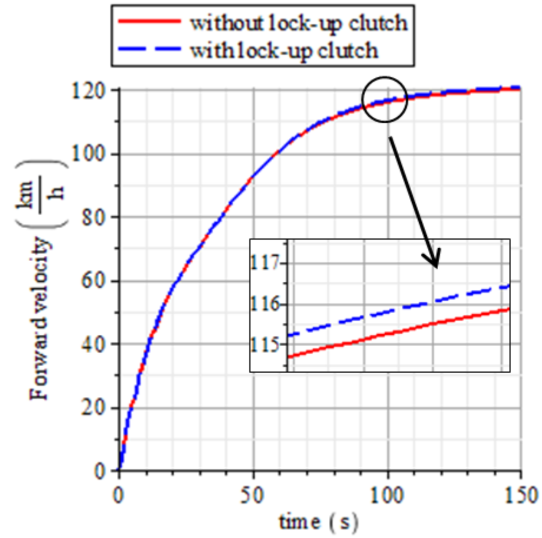

Figure 3.36: Lock-up clutch effect on forward velocity

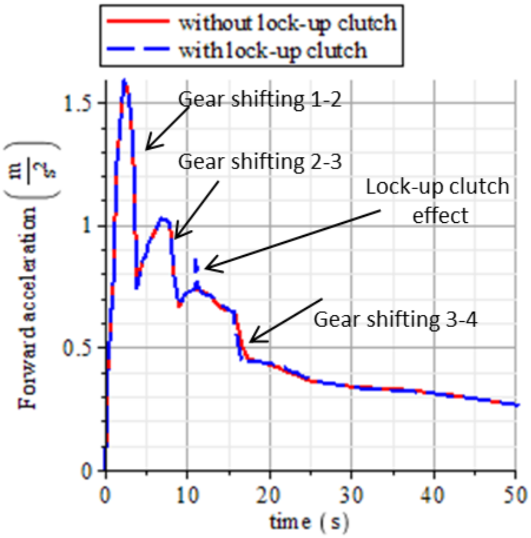

Figure 3.37: Lock-up clutch effect on forward acceleration

3.4.2 Engine Braking Simulation

During vehicle deceleration, kinetic energy is lost due to the road load, aerodynamic forces, mechanical braking, and engine braking [13]. Using the torque converter in the reverse flow mode during engine braking can help to slow down the vehicle without using an external braking mechanism. This is the most significant advantage of the reversal flow mode during the engine braking, which saves the brakes from unnecessary wear and tear.

In this section, the input to the powertrain model is a throttle angle that feeds in to the mean value engine sub-model to generate indicated power and torque to accelerate the vehicle. The proposed math-based torque converter sub-model contains both forward and reverse flow mode operations. The input throttle angle is a ramp function which is started at fully closed throttle angle and increased to the half-opened throttle angle. Then, the driver pulls off his/her foot from the accelerator pedal and the throttle angle sharply declines to the fully closed throttle position. Thus, the vehicle is first accelerated and then decelerated.

The torque converter volumetric flow rate plot (Figure 3.38) depicts the transition from the forward flow operation to the reverse flow operation. Consistent with expectations [47], the flow rate becomes negative during the flow reversal. Moreover, the flow characteristics during the gear shifting process are captured with the dynamic torque converter model. As shown in this plot, there are sharp peaks due to the torque changes from the transmission side (turbine torque).

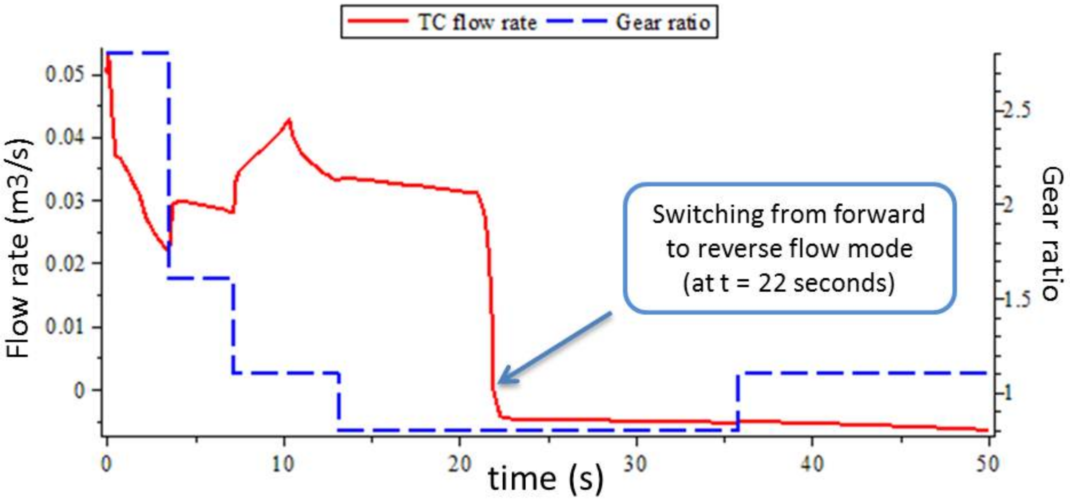

Figure 3.38: Torque converter flow rate variations during forward flow and reverse flow modes

The simulation results during the engine braking are compared with the case when the driver disconnects the engine from the transmission during the vehicle deceleration (e.g.

neutral gear). The engine rotational speed, Figure 3.39, sharply drops when the engine shaft is disconnected from the rest of the powertrain. During engine braking, the transmission shaft rotates the engine shaft, and the engine rotational speed is not decreasing as quickly as the situation without engine braking. Figure 3.40 shows how the engine braking phenomenon can slow down the vehicle during deceleration. This happens because part of the vehicle kinetic energy is used to rotate the powertrain inertias during the torque converter reverse flow operation.

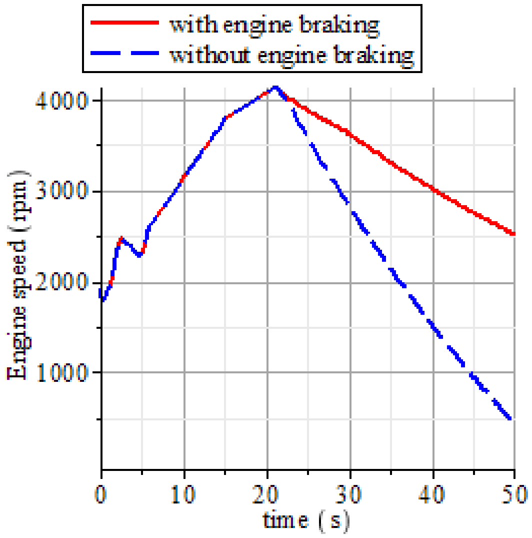

Figure 3.39: Engine braking effect on engine speed

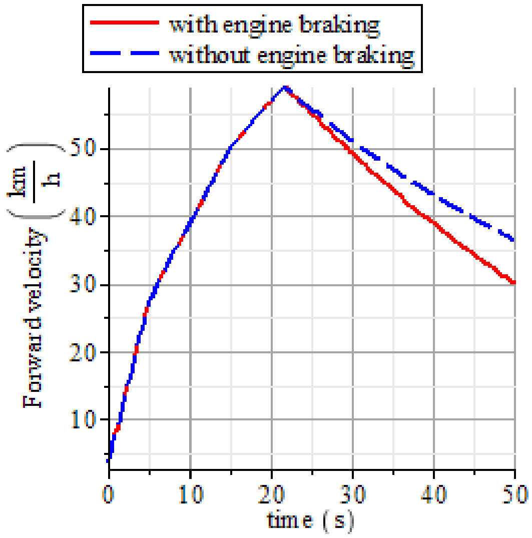

Figure 3.40: Engine braking effect on forward velocity

3.5 Chapter Summary

This chapter presents the model development and application of a hydrodynamic torque converter. The torque converter model is able to operate at all three modes, and capture both transient and steady state response for different inputs. The math-based torque converter model along with the parametric sensitivity analysis was presented at the SAE World Congress 2011 [2].

The torque converter simulation during the reverse flow operation was published in [4]. This paper includes the full evaluation of a torque converter damping characteristics. The simulation results are generated for both the linearized model as well as the original non-linear torque converter model. Then, the acausal torque converter model is integrated with the mean value engine model, automatic transmission, and vehicle longitudinal dynamics to study the torque converter characteristics in a powertrain such as lock-up clutch operation during coupling mode, and engine braking phenomenon during reverse flow operation. The simulation results were presented at the ASME Conference 2012 [3].

Chapter 4

Physics-based Spark Ignition Engine Model

This chapter presents the cycle-by-cycle spark ignition (SI) engine model. The level of complexity of the model in this study is defined such that it must be able to predict in-cylinder thermodynamic properties (e.g. pressure, burned and unburned temperature), emission gases, and mechanical torque, while having fairly fast simulation time (faster than real-time simulation time).

The proposed SI engine model contains the four strokes in the Otto cycle diagram: intake, compression, combustion-expansion (power), and exhaust. Figure 4.1 depicts the typical Otto cycle diagram in SI engine.

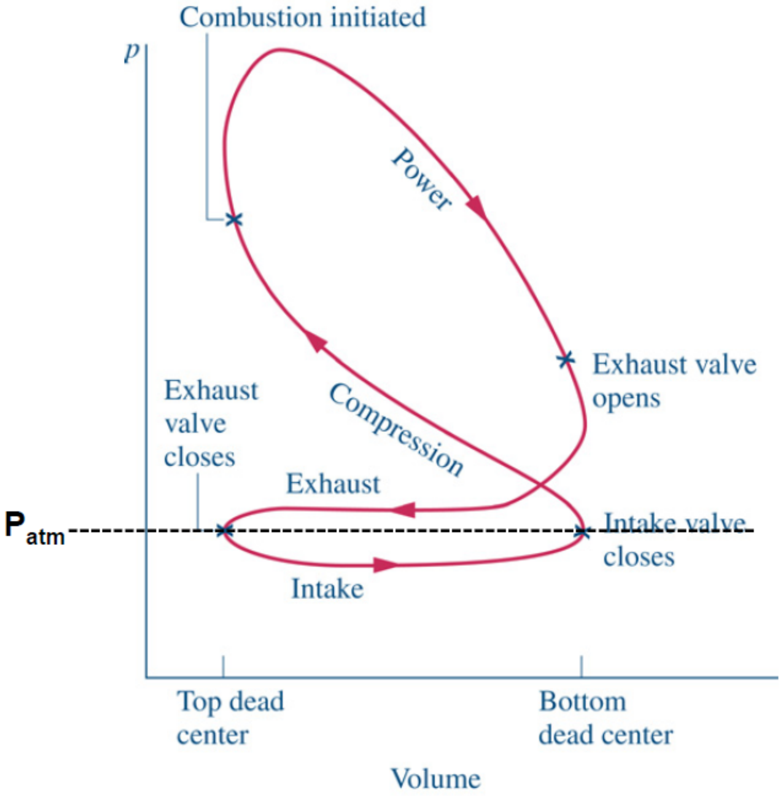

Figure 4.1: Otto cycle P-V diagram

The schematic diagram in Figure 4.2 depicts main inputs, outputs, and sub-models. The main sub-models which are discussed in this paper are the single cylinder model and emission model. The throttle body and manifold sub-model is similar to the model which is developed by Saeedi [71] in MapleSim. However, the intake manifold model is expanded to capture the manifold temperature and exhaust gas recirculation (EGR) effects. The main inputs to the cylinder sub-model are the air/fuel mixture, which is delivered from intake manifold, spark timing, which is fed to the model as a constant angle at each cycle, and the engine rotational speed (rpm). The desired outputs of the model are torque delivered to the transmission shaft, and emission gases.

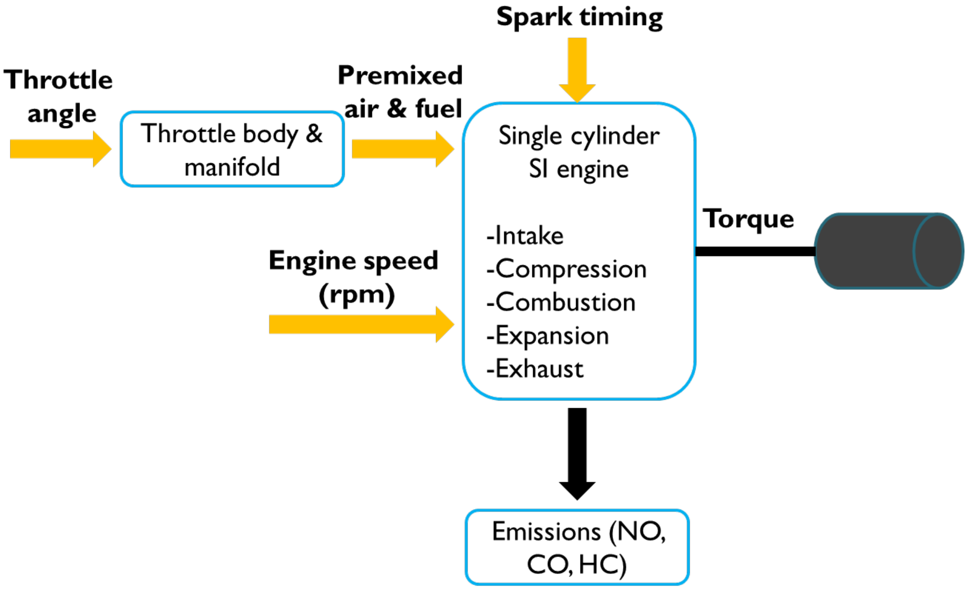

Figure 4.2: Schematic inputs/outputs diagram of single-cylinder SI engine

The details of the sub-models such as two-zone combustion, output torque, and emission gases are discussed in the following sections.

4.1 Four-cylinder Spark Ignition Engine Model

This section represents the development of four-cylinder spark ignition engine model in the MapleSim environment. The main sub-models in the four-cylinder engine model are: four-stroke cylinder model, emission gases, intake manifold, exhaust gas recirculation (EGR), spark timing, multi-body crankshaft, and dynamometer. Figure 4.3 depicts the whole sub-models in the MapleSim.

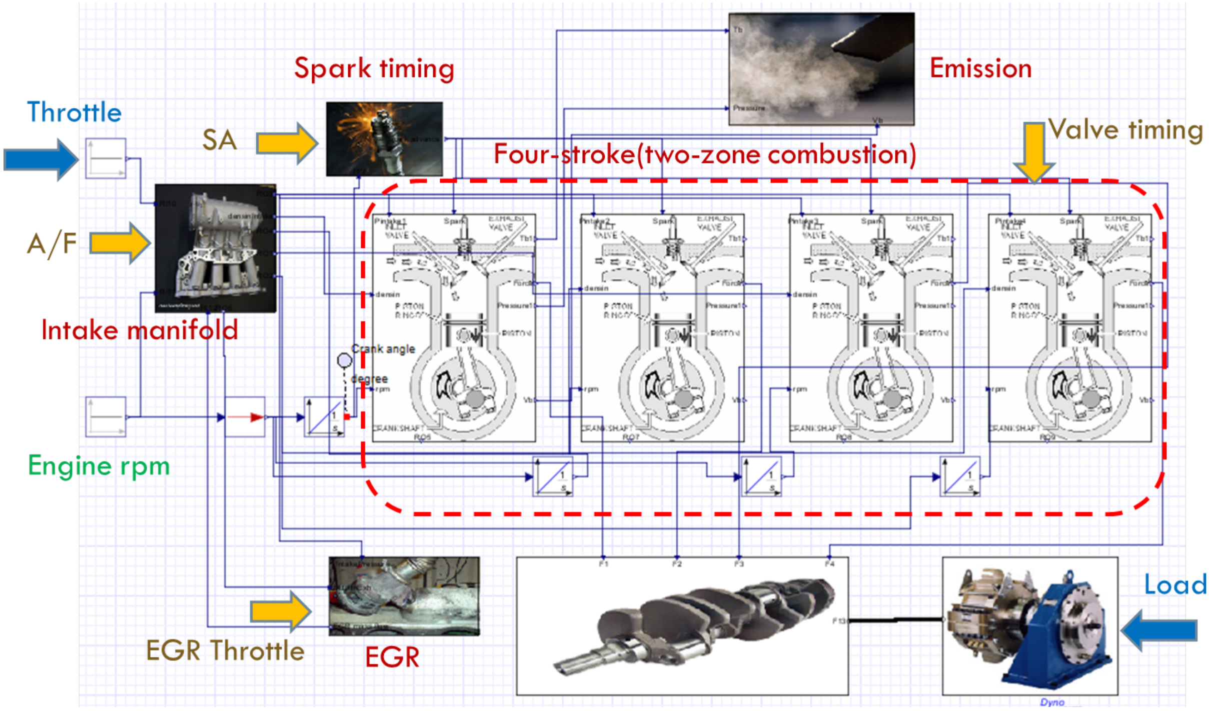

Figure 4.3: Four-cylinder SI engine model in MapleSim

The whole model consists of set of differential-algebraic equations (DAE) with variable inputs and initial conditions at each cycle simulation. MapleSim solvers are very powerful in terms of dealing with DAE systems and hybrid dynamic systems [49].

The details of the model along with the equations and inputs/outputs are described in the following sub-sections.

4.1.1 Two-zone combustion model

In a two-zone combustion modeling approach, the combustion chamber is split into burned and unburned zones [68]. The flame propagation (entrained zone) is moving from burned toward unburned zone during combustion as shown in Figure 4.4.

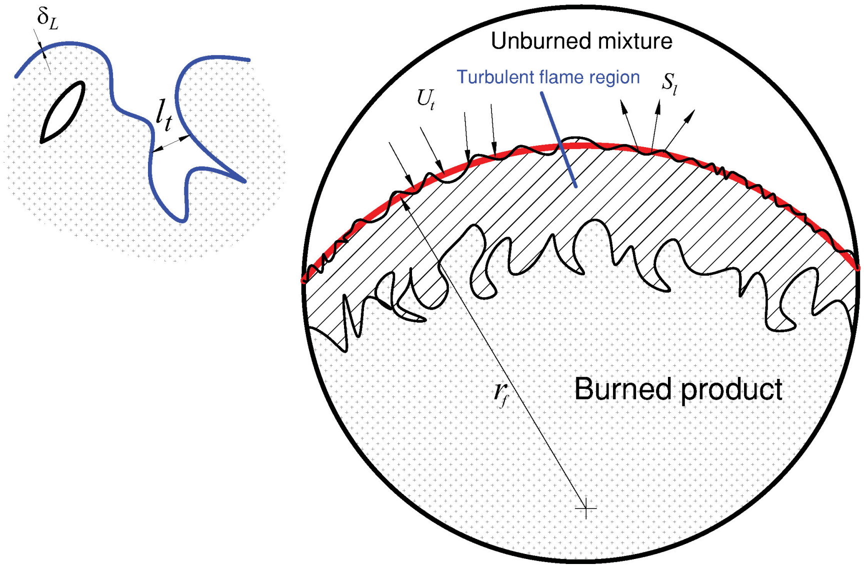

Figure 4.4: Schematic of two-zone combustion chamber

The flame propagation model in two-zone combustion has been mathematically presented in the literature [19], [45], and [77]. The well-known Blizard-Keck model [19] is employed in this study. The flame's shape is assumed spherical and the entrained zone area is assumed very small in comparison to the burned and unburned zones. Equations 4.1 and 4.2 represent physics-based model of the flame propagation through the combustion chamber. The entrained mass variation ($\dot{m}_e$) is proportional to the flame front speed, laminar speed (S_l) and characteristics speed of eddies (U_t). The eddies' length, wrinkles around the flame front in Figure 4.4, is l_t, and the time duration to burn the eddies is $t_b = \frac{l_t}{S_l}$. The eddies length (l_t) and characteristics speed (U_t) are empirically calculated from Equations 4.3 and 4.4 [19]. The mean inlet gas speed (U_i), maximum valve lift (L_{iv}), and inlet gas density (ρ_i) are constant parameters during the cycle. The unburned density defines as the ratio between unburned mass and unburned volume ($\rho_u = \frac{m_u}{V_u}$).

$$\frac{dm_e}{dt} = \rho_u A_f (U_t + S_l) \tag{4.1}$$

$$\frac{dm_b}{dt} = \rho_u A_f S_l + \frac{m_e - m_b}{t_b} \tag{4.2}$$

$$U_t = 0.08 U_i \sqrt{\frac{\rho_u}{\rho_i}} \tag{4.3}$$

$$l_t = 0.8 L_{iv} (\frac{\rho_i}{\rho_u})^{3/4} \tag{4.4}$$

The flame front area (A_f) is calculated from flame volume (V_f), and spherical flame propagation assumption (Equations 4.5 and 4.6). The sum of burned (V_b) and unburned volume (V_u) at each crank angle must be equal to the total instantaneous volume of the cylinder (V_θ). Equation 4.7 represents the instantaneous swept volume, where V_c, B, θ, r_{crank}, and L_{rod} are clearance volume, bore diameter, crank angle, crank radius, and connecting rod length, respectively. Similarly (Equation 4.8), the sum of burned (m_b) and unburned (m_u) is equal to the total in-cylinder mass (m_{Cyl}), which is aspirated during the intake stroke, from intake valve open (IVO) to intake valve close (IVC). The four physics-based DAE equations (4.1, 4.2, 4.7, and 4.8), along with an empirical Wiebe function

(S-shape mass/volume fraction) are used to find the values of burned mass (m_b), unburned mass (m_u), entrained mass (m_e), burned volume (V_b), and unburned volume (V_u) at each time step. The empirical Wiebe function has been proposed in two-zone combustion model to relate the burned mass or volume to the total mass or volume. Equation 4.9 represent the Wiebe function, where θ_{SOC} is the crank angle at start of combustion. The empirical parameters (a_1, a_2, and BD) must be identified from the experimental data. However, the burn-duration (BD) parameter can be calculated by curve fitted of experimental data (Equation 4.12). In the next section, the homotopy parameter identification method will be employed to identify the unknown empirical parameters.

$$V_f = V_b + \frac{m_e - m_b}{\rho_u} \tag{4.5}$$

$$A_f = 0.25\pi(\frac{2V_f}{\pi B^2})^2 \tag{4.6}$$

$$V_b + V_u = V_\theta = V_c + \frac{\pi B^2 r_{crank}}{8}\left(1 - cos\theta - \frac{r_{crank}}{L_{rod}}(sin\theta)^2\right) \tag{4.7}$$

$$m_b + m_u = m_{Cyl} \tag{4.8}$$

$$\frac{V_b}{V_\theta} = 1 - \exp\left(-a_1(\frac{\theta - \theta_{SOC}}{BD})^{a_2+1}\right) \tag{4.9}$$

The advantages of using two-zone combustion model with the turbulent flame propagation, in comparison with dimensional and zero-dimensional approaches, are:

- The model is more realistic than a zero-dimensional mean-value model to predict burned/unburned heat transfer, mass, pressure, and temperature.
- The model has a fairly fast simulation time; therefore it is computationally efficient to run for many cycles.
- It can be integrated to the rest of the powertrain, or can be used in conjunction with other software (e.g. GT-Power).

The main assumptions used to model a two-zone combustion SI engine model in this paper are:

- The intake and exhaust strokes are isentropic processes.
- The compression and expansion strokes are modelled based on the first thermodynamic law as a single zone model.
- The pressure distribution is uniform inside the cylinder during each stroke.
- The combustion process is modelled based on the turbulent flame propagation theory in addition to the first law of thermodynamics.
- The flame front shape is assumed to be spherical. However, the flame thickness (volume) is assumed small in comparison with burned and unburned zones.
- During the combustion, each zone has a uniform composition and temperature.

- The burned/unburned gases are considered as ideal gases.
- The engine speed (rpm) is assumed constant at each cycle.

The whole cycle simulation is described by Figure 4.5. The intake stroke starts when the piston goes from top-dead-centre (TDC) of the cylinder to the bottom-dead-centre (BDC). During the intake process the homogenous air and fuel mixture enters into the cylinder with the rate of the displaced volume ($\dot{V}_d(t)$). The intake pressure can be approximately defined as the difference between intake manifold pressure and pressure loss through the valves (ΔP_v) (Equation 4.10). The mixture's temperature during the intake process is calculated from the ideal gas law, by assuming adiabatic process (Equation 4.11). The ρ_{mix} represents the average density of the air-fuel mixture in the cylinder.

$$P_{in} = P_m - \Delta P_v \tag{4.10}$$

$$T_{in} = \frac{P_{in}}{\rho_u R_u} \tag{4.11}$$

Then, the simulation switches to the compression stroke from BDC to some angles close to the next TDC. The total mass of the mixture during the compression stroke is constant, and the thermodynamic formulation is derived by assuming single zone control volume with heat transfer towards the cylinder walls.

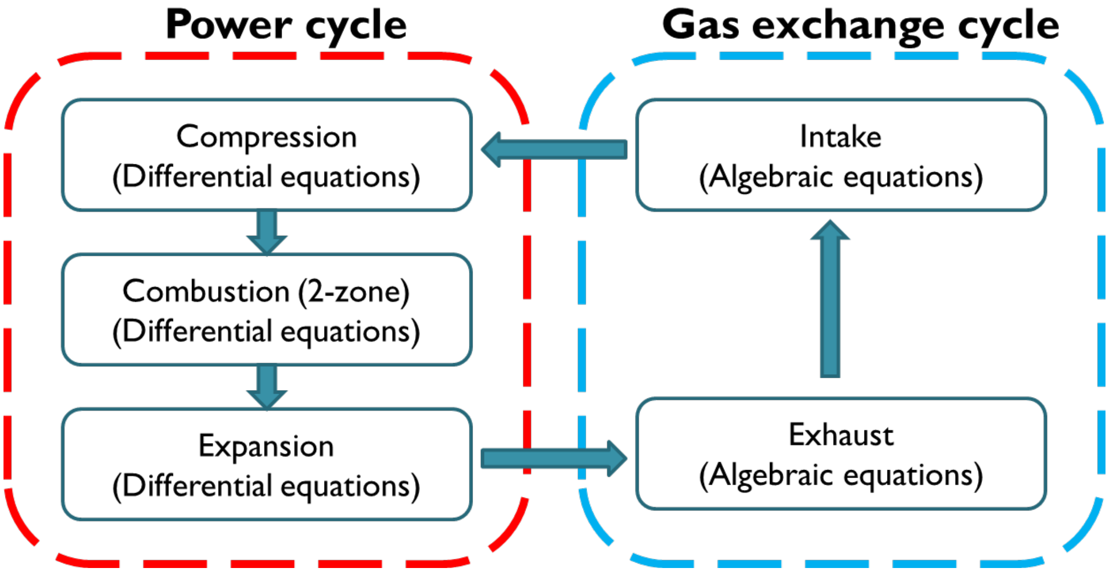

Figure 4.5: Four-stroke cycle simulation procedure

The combustion process is started when the spark plug is ignited until the total mass is burned. The burned duration (BD), as a fraction of crank angle, is empirically defined by Equation 4.12 [17]. In this equation CR , n, Φ, and SA represent compression ratio, engine speed, equivalence ratio, and spark advance angle, respectively.

$$BD^O = \left(3.2989 - 3.3612(\frac{CR}{7.5})^2 + 1.08(\frac{CR}{7.5})^2\right)\left(0.1222 + 0.9717(\frac{n}{1000}) - 0.0505(\frac{n}{1000})^2\right) \\ \left(4.311 - 5.6383(\Phi) + 2.3040(\Phi)^2\right)\left(1.068 + 0.290(\frac{SA^o}{30}) + 0.2545(\frac{SA^o}{30})^2\right) \tag{4.12}$$

The temperature variations in the burned (Equation 4.13) and unburned zones (Equation 4.14) are calculated from 1^{st} law of thermodynamics along with the conservation of mass law. In this study, the mathematical formulation from [82] is used to calculate burned

(T_b) and unburned (T_u) temperature. The in-cylinder pressure is sum of the burned and unburned pressure at each crank angle (P_{Cyl}) as expressed in the Equations 4.15.

$$\dot{T}_b = \frac{1}{c_{pb} m_b} \left(P_{Cyl}\dot{V} - (R_b T_b - R_u T_u)\,\dot{m}_b - \frac{R_u}{cpu} \left(V_u \dot{P}_{Cyl} + \dot{Q}_u \right) + \dot{P}_{Cyl} V \right) \tag{4.13}$$

$$\dot{T}_u = \frac{1}{c_{pu} m_u} \left(\dot{P}_{Cyl} V_u - \dot{Q}_u \right) \tag{4.14}$$

$$\dot{P}_{Cyl} = \frac{\gamma_b - 1}{V} \left(\frac{(Eff_{comb})(LHV)}{14.6\Phi + 1} \dot{m}_b - P_{Cyl}\dot{V} \right) - \left(\dot{Q}_u + \dot{Q}_b \right) \tag{4.15}$$

The specific heat capacity for the burned mixture at constant volume (c_{vb}), constant pressure (c_{pb}), and the ratio (γ_b) are expressed as a function of burned temperature, from empirical results [88], in Equations 4.16 and 4.17. Since the unburned temperature variations is not large, the specific heat capacity ratio (γ_u) is assumed constant (e.g. $\gamma_b = 1.35$). Then, the specific heat capacity for the unburned mixture at constant volume (c_{vu}) and constant pressure (c_{pu}) are calculated from the Equation 4.18. The specific gas constant for the burned (R_b) and the unburned (R_u) mixture are calculated from Equation 4.19. The burned (M_b) and unburned (M_u) mixture has different molecular weight.

$$\gamma_b = -0.013(\frac{T_b}{1000})^3 + 0.088(\frac{T_b}{1000})^2 - 0.214(\frac{T_b}{1000}) + 1.432 \tag{4.16}$$

$$c_{pb} = \frac{\gamma_b R_b}{\gamma_b - 1}, \qquad c_{vb} = c_{pb} - R_b \tag{4.17}$$

$$c_{pu} = \frac{\gamma_u R_u}{\gamma_u - 1}, \qquad c_{vu} = c_{pu} - R_u \tag{4.18}$$

$$R_b = \frac{\bar{R}}{M_b}, \qquad R_u = \frac{\bar{R}}{M_u} \tag{4.19}$$

The heat transfer rate between mixture and cylinder walls for burned, $\dot{Q}_b$, and unburned, $\dot{Q}_u$, zones are calculated from the semi-empirical model developed by Hohenberg [46] as shown in Equation 4.20. The heat transfer area (A_w) includes both cylinder head area, which is constant, and cylinder wall area which is the function of a crank angle.

$$\dot{Q}_i = 130(A_w)\frac{(P_{Cyl}^{0.8})(\bar{U}_p^{0.8})}{(V^{0.06})(T_i^{0.4})}\left(T_i - T_w\right), \qquad i = b, u \tag{4.20}$$

The expansion stroke starts at the end of the combustion process and finishes when the piston reaches to the BDC. The expansion and compression strokes are modeled based on the single-zone control volume including heat transfer between the mixture and cylinder walls. The mathematical formulation of the expansion and compression strokes are simplified version of the two-zone model during the combustion process. The total mass during the compression stroke is assumed constant and unburned, and during the expansion is constant and fully burned mixture [15].

Finally, the exhaust valve is opened and the piston moves from the BDC to the TDC and the exhaust gases are driven out through exhaust valve. The exhaust stroke is assumed adiabatic process, no heat transfer, and the cylinder pressure is slightly above the atmospheric pressure (Equation 4.21).

$$P_{exh} = (1.05 \quad ... \quad 1.25)P_0 \tag{4.21}$$

The exhaust gas temperature is calculated based on the burned gas temperature (T_b) at the end of the expansion stroke. Equation 4.22 represents the relation between exhaust gas temperature (T_{exh}) and burned gas temperature at the end of the expansion stroke.

$$T_{exh} = \left(\frac{P_{exh}}{P_{expansion}}\right)^{0.3} T_b \tag{4.22}$$

4.1.2 Intake manifold model

The proposed intake manifold model in this research is developed based on the mean-value engine formulation in [35]. Saeedi [71] created intake manifold model along with throttle body in the MapleSim. The model in [71] does not include exhaust gas recirculation (EGR) effect and intake manifold's temperature variations. Figure 4.6 depicts the components (e.g. custom components and look-up tables) along with the main inputs and outputs of the sub-model. The main custom components in this sub-model are: throttle area calculation, throttle air mass flow, and intake manifold.

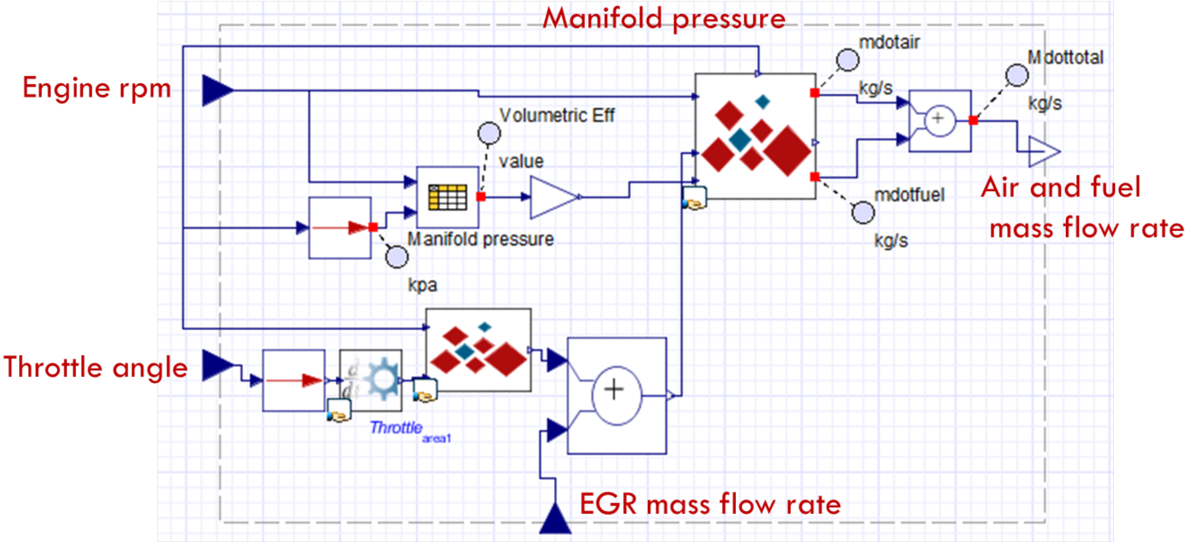

Figure 4.6: Intake manifold sub-model in MapleSim

The driver's command, which is introduced as a throttle angle, is fed to the throttle area custom component to be used for throttle area calculation (Equation 4.23) [39]. The throttle area, which is the projected area of the oval shape throttle butterfly in the flow direction, is function of a throttle bore (D), throttle pin (d), and throttle angle (ϕ). The initial value of the throttle angle (ϕ_0) at fully closed position is set to 7 degrees.

$$\begin{aligned} A_{Th} &= \frac{\pi D^2}{4}(1 - \frac{cos\phi}{cos\phi_0}) + \frac{d}{2cos\phi}\sqrt{D^2cos^2\phi - d^2cos^2\phi_0} \\ &+ \frac{D^2cos\phi}{2cos\phi_0}arcsin(\frac{dcos\phi_0}{Dcos\phi}) - \frac{d}{2}\sqrt{D^2 - d^2} + \frac{D^2}{2}arcsin(\frac{d}{D}) \end{aligned} \tag{4.23}$$

The throttle area and the intake pressure are used to calculate throttle air mass flow rate (Equation 4.24).

$$\overset{\bullet}{m}_{Th} = \begin{cases} \left(C_{DTh}.A_{Th}.P_0\right) \Big/ \left(\sqrt{R.T_0}\right) \left({}^{2\gamma}\!/\!_{(\gamma-1)} \left(1 - \left({}^{P_m}\!/\!_{P_0} \right)^{\frac{\gamma-1}{\gamma}} \right) \right)^{0.5} \left({}^{P_m}\!/\!_{P_0} \right)^{\frac{1}{\gamma}} \\ \text{when } {}^{P_m}\!/\!_{P_0} > \left({}^{2}\!/\!_{(\gamma+1)} \right)^{\frac{\gamma}{\gamma-1}} \\ \\ \left(C_{DTh}.A_{Th}.P_0\right) \Big/ \left(\sqrt{R.T_0}\right) \left({}^{2}\!/\!_{(\gamma+1)} \right)^{\frac{(\gamma+1)}{2(\gamma-1)}} \gamma^{0.5} \\ \text{when } {}^{P_m}\!/\!_{P_0} \leqslant \left({}^{2}\!/\!_{(\gamma+1)} \right)^{\frac{\gamma}{\gamma-1}} \end{cases} \tag{4.24}$$

The intake manifold is assumed as a constant volume chamber with inflow mass ($\dot{m}_{Th}$) and outflow mass ($\dot{m}_{Cyl}$). Therefore, the physics-based model of the intake manifold can be derived from the first thermodynamics law as well as the conservation of mass law in the manifold control volume [59]. The schematic of the intake manifold control volume is shown in Figure 4.7.

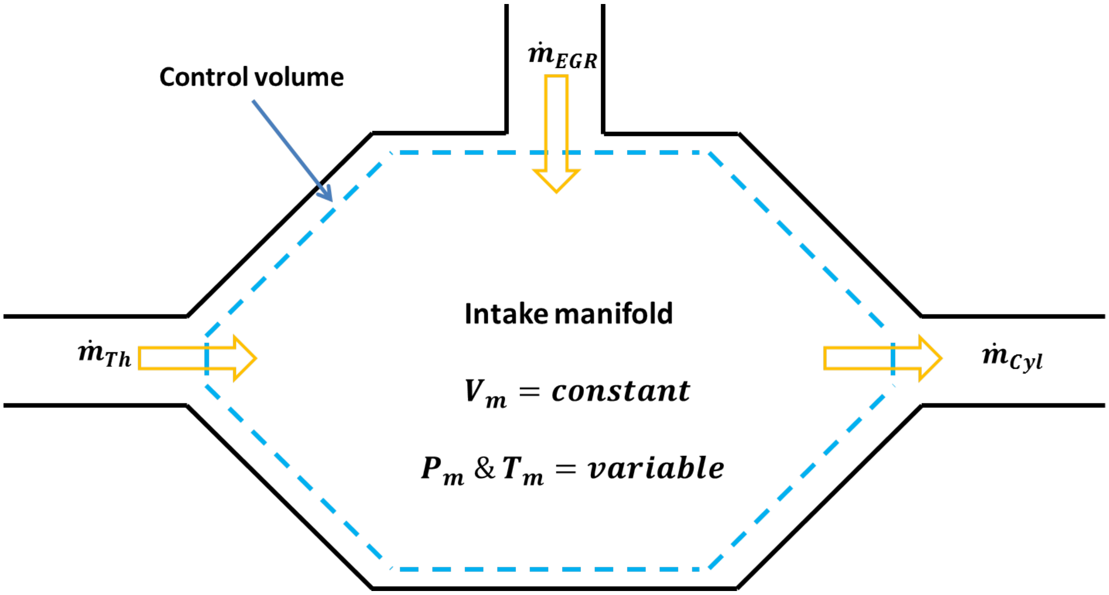

Figure 4.7: Intake manifold control volume

According to the conservation of mass law, the control volume mass variations can be derived from Equation 4.25. The calculation of the EGR mass flow rate ($\dot{m}_{EGR}$) is shown in the next section.

$$\frac{dm_{cv}}{dt} = \dot{m}_{Th} + \dot{m}_{EGR} - \dot{m}_{Cyl} \tag{4.25}$$

The manifold pressure and temperature as well as the outflow mass, which flows toward the cylinders, are calculated from Equations 4.26, 4.27, and 4.28. The ideal gas assumption in the control volume is fairly reasonable assumption, since the manifold temperature and pressure variations are not very significant.

$$\frac{dP_m}{dt} = \frac{\gamma R T_m}{V_m} \left(\dot{m}_{Th}(\frac{T_{Th}}{T_m}) + \dot{m}_{EGR}(\frac{T_{EGR}}{T_m}) - \dot{m}_{Cyl} \right) \tag{4.26}$$

$$\frac{dT_m}{dt} = \frac{R(T_m)^2}{P_m V_m}(\dot{m}_{Th}(\gamma\frac{T_{Th}}{T_m} - 1) + \dot{m}_{EGR}(\gamma\frac{T_{EGR}}{T_m} - 1) - \dot{m}_{Cyl}(\gamma - 1)) \tag{4.27}$$

$$\dot{m}_{Cyl} = \frac{\eta_v S \pi B^2 n P_m}{120 R T_m} \tag{4.28}$$

The volumetric efficiency (η_v) in Equation 4.28 is introduce as the empirical look-up table data, which is the function of the engine speed (n) and the manifold pressure (P_m). The volumetric efficiency is represented in different empirical equations (correlation models) [71]. In this study, the volumetric efficiency model is depicted in Figure 4.8 [41].

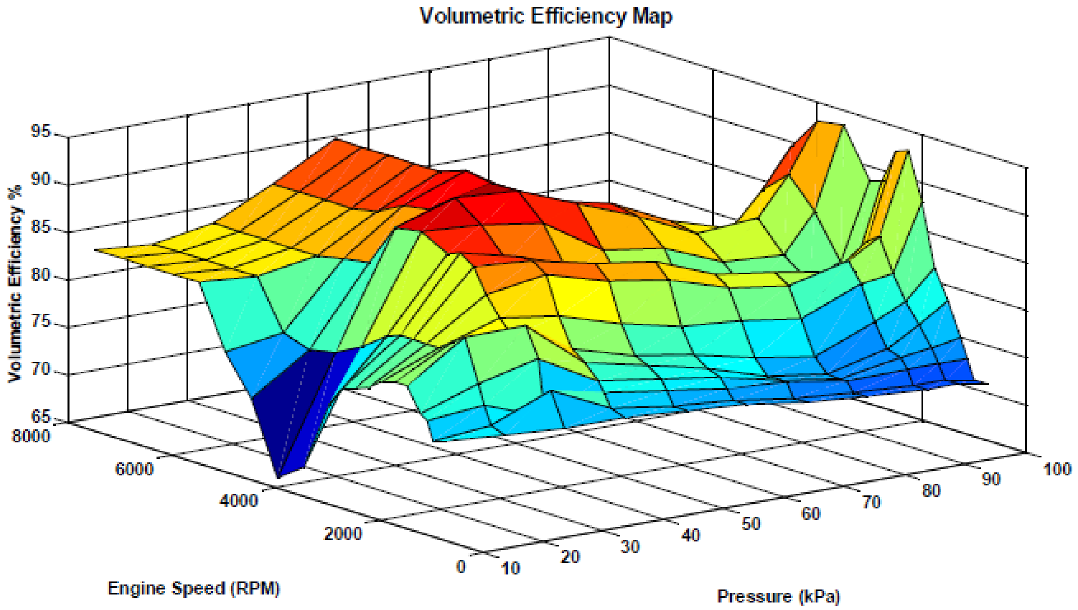

Figure 4.8: Volumetric efficiency map [41]

The fuel injector is assumed to be placed in either intake manifold chamber or after that (port injection). The amount of fuel mass rate ($\dot{m}_{Fuel}$) is calculated based on the air mass flow rate ($\dot{m}_{Cyl}$) and equivalence ratio (Φ) as shown in Equation 4.29.

$$\dot{m}_{Fuel} = \frac{\dot{m}_{Cyl}}{14.6\Phi} \tag{4.29}$$

The equivalence ratio is defined as a ratio between stoichiometric air-fuel ratio and actual air-fuel ratio (Equation 4.30). The stoichiometric air-fuel ratio for SI engines is typically around 14.6, and consequently the stoichiometric equivalence ratio is 1 .

$$\Phi = \frac{(\frac{A}{F})_{Stoichiometric}}{(\frac{A}{F})_{Actual}} \tag{4.30}$$

The air and fuel mass flow rate are the inputs to the cylinder models during the intake stroke.

4.1.3 Exhaust gas recirculation (EGR) model

The objective of using exhaust gas recirculation (EGR) mechanism is reducing NO_x emission by feeding back part of the exhaust gas (5% to 25%) into the intake manifold. The EGR mechanism decreases the amount of the mass flow rate into the cylinders ($\dot{m}_{Cyl}$), and consequently peak pressure and adiabatic temperature will be reduced. Therefore NO_x emission, which is very sensitive to the adiabatic temperature, will be significantly reduced. The EGR mechanism is usually active at medium load and engine speed (rpm) operation such as vehicle cruising on highways. However, at high load operation (e.g. uphill traveling) and low engine speed (e.g. ideal operation) the EGR mechanism is not useful and must be switched off.

Likewise intake manifold models, there are different EGR models in different level of complexity. In this study, the EGR model is formulated based on the mean value engine model development from [35]. The schematic exhaust manifold model is shown in Figure 4.9. The exhaust gas is assumed to be an ideal gas, and the inflow exhaust mass flow rate ($\dot{m}_{exIN}$) is assumed to be equal to the outflow intake mass flow rate ($\dot{m}_{Cyl} + \dot{m}_{Fuel}$).

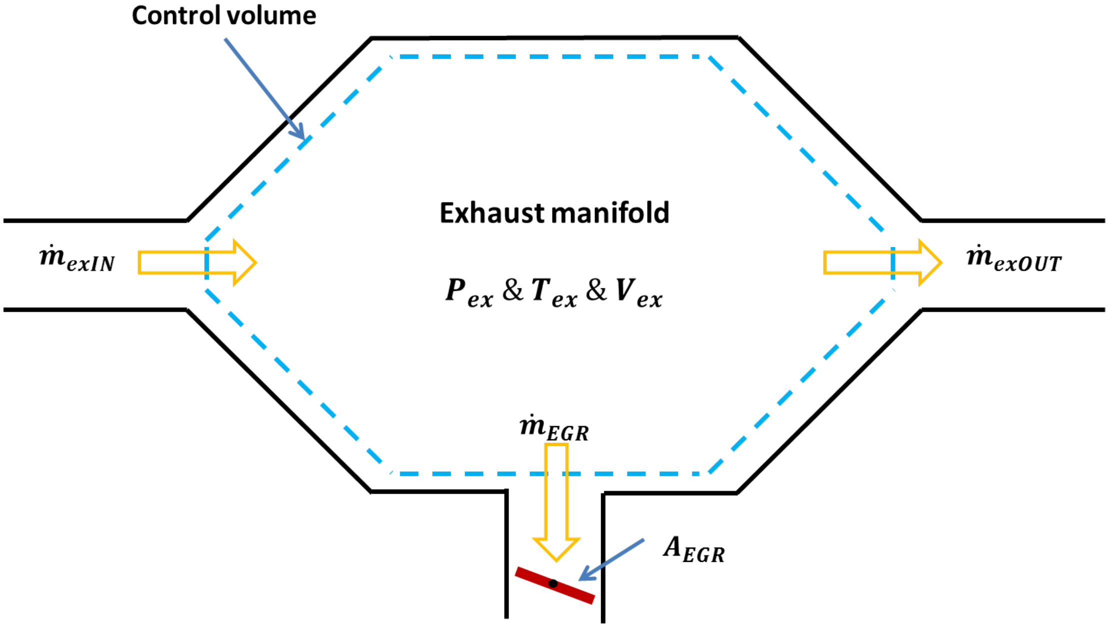

Figure 4.9: Exhaust manifold control volume

The exhaust manifold mathematical equations from [35] are employed to calculate exhaust manifold thermodynamic state variables (e.g.P_{exh}) (Equation 4.31), exhaust mass flow rate ($\dot{m}_{exhOUT}$) (Equation 4.32), and EGR mass flow rate ($\dot{m}_{EGR}$) (Equation 4.33). $C_{D_{ex}}$ and $C_{D_{EGR}}$ are empirical discharge coefficient through the exhaust (catalytic converter) and EGR valves. The amount of EGR mass flow rate can be controlled by regulating the EGR throttle as shown in Figure 4.9. The EGR throttle control is introduced as the EGR projected area (A_{EGR}) in Equation 4.33.

$$\frac{dP_{exh}}{dt} = \frac{RT_{exh}}{V_{exh}}(\dot{m}_{exhIN} - \dot{m}_{exhOUT} - \dot{m}_{EGR}) \tag{4.31}$$

$$\dot{m}_{exhOUT} = C_{D_{exh}} A_{exh} \sqrt{\frac{2P_{exh}}{RT_{exh}}(P_{exh} - P_0)} \tag{4.32}$$

$$\dot{m}_{EGR} = C_{D_{EGR}} A_{EGR} \sqrt{\frac{2P_{exh}}{RT_{exh}}(P_{exh} - P_m)} \tag{4.33}$$

4.1.4 Emission model

The emission sub-model, which is created along with the two-zone combustion model, takes the in-cylinder pressure, burned temperature, and volume as inputs and calculates the emission gases (e.g. NO and CO). The emission calculation procedure is shown in Figure 4.10.

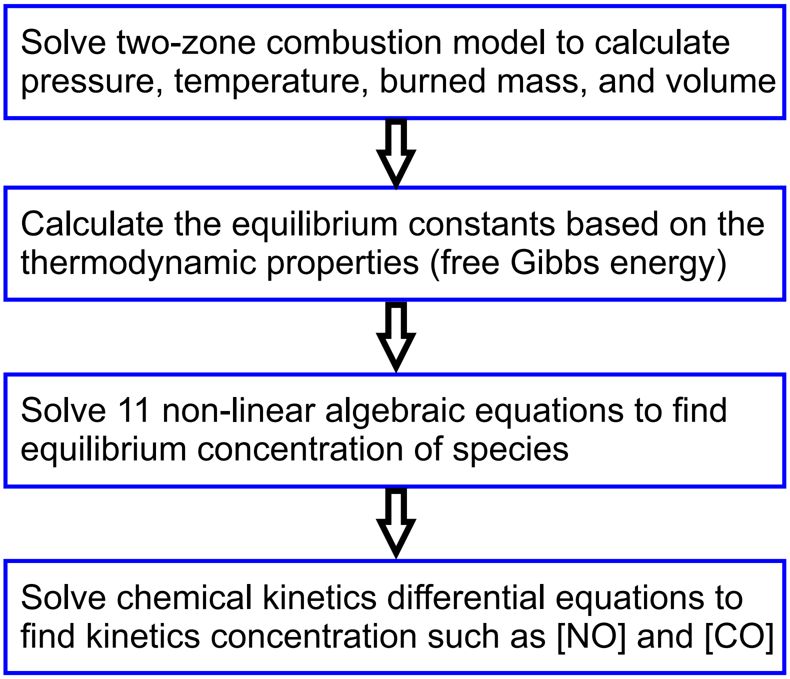

Figure 4.10: Emission calculation procedure

The general formulation of air and fuel reaction is shown in Equation 4.53, where Υ_1 and Υ_2 represent type of the hydrocarbon fuel and Υ is given by Equation 4.35, and Φ introduces equivalence ratio (the ratio between stoichiometric and real air-fuel ratio).

$$C_{\Upsilon_1}H_{\Upsilon_2} + \Upsilon(O_2 + 3.46N_2) \rightarrow \chi_{CO_2}CO_2 + \chi_{CO}CO + \chi_{H_2O}H_2O + \chi_{H_2}H_2 + \\ \chi_H H + \chi_{OH}OH + \chi_{N_2}N_2 + \chi_{NO}NO + \chi_N N + \chi_{O_2}O_2 + \chi_O O \tag{4.34}$$

$$\Upsilon = \frac{\Upsilon_1 + \frac{\Upsilon_2}{4}}{\Phi} \tag{4.35}$$

The products of the reaction are eleven species, and the coefficients χ_i represent the mole fraction of each species during the reaction [81]. The proposed emission eleven species are assumed in equilibrium, so four atom balance and seven equilibrium reaction equations are derived to calculate equilibrium species at each time step. Four atom balance equations for C, H, O, and N are listed in the set of equations in Equation 4.36.

$$\begin{aligned}
C: &\quad \Upsilon_1 = \chi_{CO_2} + \chi_{CO} \\
H: &\quad \Upsilon_2 = 2\chi_{H_2O} + 2\chi_{H_2} + \chi_H + \chi_{OH} \\
O: &\quad 2\Upsilon = 2\chi_{CO_2} + \chi_{CO} + \chi_{H_2O} + \chi_{OH} + \chi_{NO} + 2\chi_{O_2} + \chi_O \\
N: &\quad 7.52\Upsilon = 2\chi_{N_2} + \chi_{NO} + \chi_N
\end{aligned} \tag{4.36}$$

The seven equilibrium reactions are shown in Equation 4.37, where the molar fraction of each species is represented by X_i. κ_{P_i} represents the equilibrium constant of the i^{th} equilibrium reaction. The equilibrium constant is calculated based on the Gibbs free energy (GB_i) and combustion temperature (Equation 4.38). P_{Cyl} and P_0 are in-cylinder pressure at each time step and ambient (reference) pressure respectively.

$$\begin{aligned}
&H_2 \leftrightarrow H + H \qquad X_H = \sqrt{\frac{\kappa_{P_1}}{\frac{P_{Cyl}}{P_0}}}\sqrt{X_{H_2}} \\
&O_2 \leftrightarrow O + O \qquad X_O = \sqrt{\frac{\kappa_{P_2}}{\frac{P_{Cyl}}{P_0}}}\sqrt{X_{O_2}} \\
&N_2 \leftrightarrow N + N \qquad X_N = \sqrt{\frac{\kappa_{P_3}}{\frac{P_{Cyl}}{P_0}}}\sqrt{X_{N_2}} \\
&H_2O \leftrightarrow H_2 + 0.5O_2 \qquad X_{H_2} = \frac{\kappa_{P_4}}{\frac{P_{Cyl}}{P_0}}\frac{X_{H_2O}}{\sqrt{X_{O_2}}} \\
&H_2O \leftrightarrow 0.5H_2 + OH \qquad X_{OH} = \frac{\kappa_{P_5}}{\frac{P_{Cyl}}{P_0}}\frac{X_{H_2O}}{\sqrt{X_{H_2}}} \\
&CO_2 \leftrightarrow CO + 0.5O_2 \qquad X_{CO} = \frac{\kappa_{P_6}}{\frac{P_{Cyl}}{P_0}}\frac{X_{CO_2}}{\sqrt{X_{O_2}}} \\
&0.5O_2 + 0.5N_2 \leftrightarrow NO \qquad X_{NO} = \kappa_{P_7}\sqrt{X_{N_2}X_{O_2}}
\end{aligned} \tag{4.37}$$

The specific Gibbs energy is a property of each species which varies with temperature. Therefore, the specific Gibbs energy values of species (for eleven species) are modelled as group of look-up tables based on physical properties [81].

$$\kappa_{P_i} = exp\left(\frac{-\Delta GB_i}{\bar{R}.T_b}\right) \tag{4.38}$$

The equilibrium concentration of each species at each time step is calculated by solving four algebraic atom balance and seven nonlinear algebraic equilibrium concentration equations. Then, the well-known extended Zeldovich mechanism is employed to calculate the kinetic concentration of NO (Equation 4.39) and a similar formulation is derived in [11] for CO (Equation 4.40).

$$\frac{1}{V_b}\frac{d[NO]}{dt} = \frac{2\Gamma_1(1-(\frac{[NO]}{X_{NO}})^2)}{1+\frac{[NO]}{X_{NO}}\frac{\Gamma_1}{\Gamma_2+\Gamma_3}}$$

$$\begin{aligned}
\Gamma_1 &= 7.6\times 10^{13} exp(\frac{-38000}{T_b})X_O X_{N_2}\\
\Gamma_2 &= 1.5\times 10^{9} exp(\frac{-19500}{T_b})X_O X_{NO}\\
\Gamma_3 &= 2\times 10^{14} exp(\frac{-23650}{T_b})X_{NO} X_H
\end{aligned} \tag{4.39}$$

$$\frac{1}{V_b}\frac{d[CO]}{dt} = (\Gamma_1+\Gamma_2)(1-\frac{[CO]}{X_{CO}})$$

$$\begin{aligned}
\Gamma_1 &= 6.76\times 10^{10} exp(\frac{T_b}{1102})X_{CO} X_{OH}\\
\Gamma_2 &= 2.5\times 10^{12} exp(\frac{-24055}{T_b})X_{O_2} X_{CO}
\end{aligned} \tag{4.40}$$

4.1.5 Friction model

In some studies on spark ignition engine modeling, the effect of friction has been neglected for simplicity. In some engine operating conditions (e.g. full load and low engine speed condition) the friction effect is small enough to be neglected, but at high engine speed the friction effect is significant. Therefore, the friction effect in mechanical parts as well as piston-cylinder interactions must be considered in math-based thermodynamic calculations.

The main sources of power losses during the engine operation are:

- Pumping losses: this is significant power loss during part load operation (part load throttling), and is included in the “intake manifold” sub-model.
- Heat transfer: this happens due to the temperature difference between in-cylinder mixture and cylinder walls. The heat transfer is significant at low engine speed, since the cycle time is more at low engine speed. The heat transfer model including both convection and radiation are mentioned in the previous section.
- Mechanical losses: the damping coefficient in mechanical joints (crankshaft revolute joints) is introduced to represent joint friction. The crankshaft multi-body model is fully described in the next section.
- Piston friction: piston back and forth motion inside the cylinder generates power loss. The piston friction is categorized into skirt friction and pressure ring friction [87].

The piston friction in this study is based on the mathematical model developed in [1]. The friction effect is introduced as a resistant pressure, negative pressure, in the four-stroke formulation. The piston friction work, skirt and pressure ring friction, is mathematically derived from Newton's viscosity law (Equation 4.41). The oil dynamic viscosity (μ) is assumed constant parameter during the four-stroke operation (e.g. $SAE30$ at 100^oC). However in more realistic cases the dynamic viscosity should be variable with in-cylinder temperature, but its value is not significantly changed from the value at 100^oC at higher temperatures. The piston speed (m/s) as a function of crank angle is defined in Equation 4.42, where the average piston speed is proportional to the engine angular speed ($\bar{U}_p = \frac{1}{15} r_{crank} n_{rpm}$).

$$\delta W_f = \mu U_p(\theta) \pi B \Delta x \left(\frac{L_{skirt}}{C_{skirt}} + \frac{L_{ring}}{\varepsilon_{oil}} \right) \tag{4.41}$$

$$U_p(\theta) = \bar{U}_p \frac{\pi}{2} sin(\theta) \left(1 + \frac{cos(\theta)}{\sqrt{\frac{L_{rod}}{r_{crank}} - sin^2(\theta)}} \right) \tag{4.42}$$

The skirt length (L_{skirt}), ring length (L_{ring}), and skirt clearance (C_{skirt}) are assumed constant parameters in the Equation 4.41 [1]. The parameter ε_{oil} represents the oil film thickness between the ring and cylinder wall. The oil film distribution is variable with piston position. For instance, the thickness is minimum at TDC and BDC and it reaches to the maximum value at the middle position. Equation 4.43 represents the semi-empirical relation between oil film thickness and crank angle [38], where A_1 and A_2 are constant parameters.

$$\varepsilon_{oil} = A_1 + A_2 \mid sin(\theta) \mid \tag{4.43}$$

The mean effective friction pressure, which is introduced in the thermodynamic equations, can be calculated by Equation 4.44, where ΔV_d is the displaced volume.

$$f_{mep} = \frac{\delta W_f}{\Delta V_d} \tag{4.44}$$

The cycle simulation including piston friction effects along with parameters are discussed in the "Multi-cycle Simulation" section.

4.1.6 Crankshaft multi-body model

The crankshaft mechanism is converting thermodynamic power to the rotational mechanical power (or break torque). In the cylinder model, the two-zone combustion was employed to calculate in-cylinder pressure at each crank angle. The net force acting on the piston area is calculated from Equation 4.45. P_{Cyl}, P_{atm}, and A_p represent in-cylinder pressure at each crank angle, atmospheric pressure, and piston area respectively as shown in Figure 4.11.

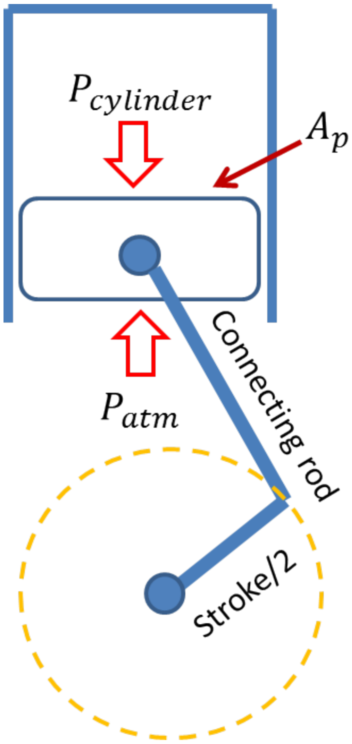

Figure 4.11: Schematic model of piston-cylinder

$$F_p = (P_{Cyl} - P_{atm})A_p \tag{4.45}$$

The calculated piston force from each cylinder is the input to the multi-body model. The multi-body model includes four sub-model for four cylinders, flywheel, and revolute joint which is connected to the dynamometer through flange connections (Figure 4.12).

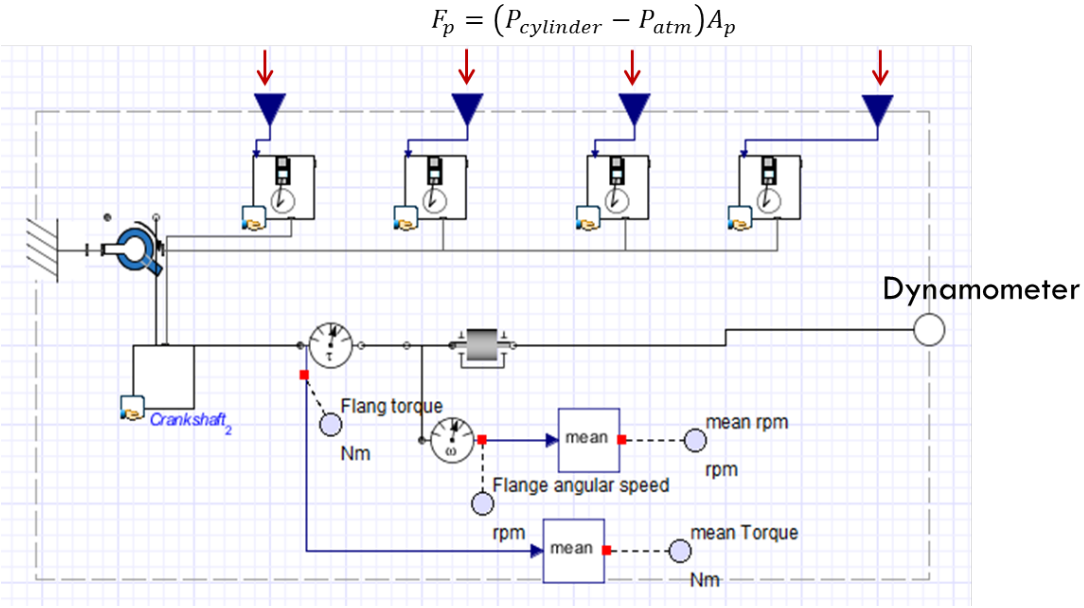

Figure 4.12: Multi-body sub-model in MapleSim

Each cylinder sub-model consists of piston, connecting rod, and crank which are connected together through revolute joints as shown in Figure 4.13.

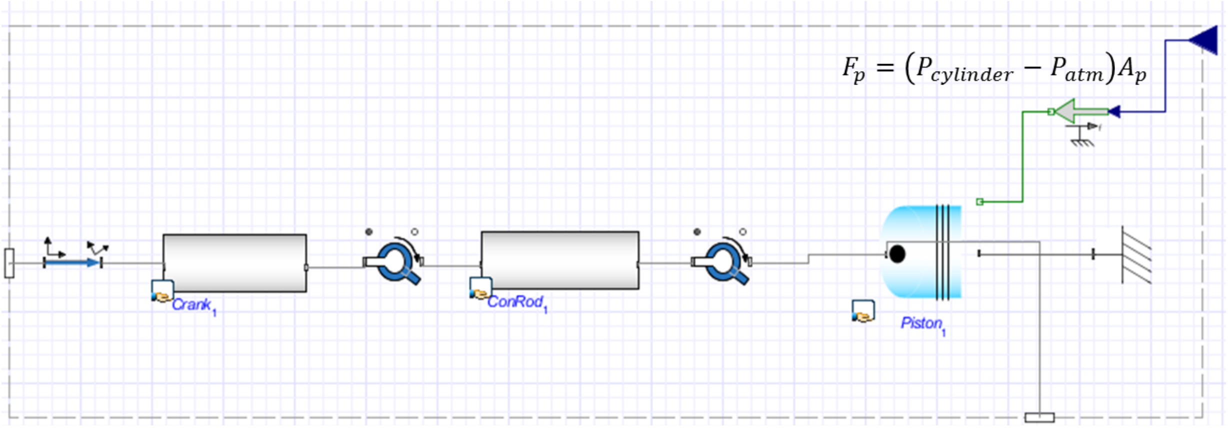

Figure 4.13: Multi-body cylinder model

Piston motion inside the cylinder is back and forth vertical motion. Thus, the piston is modeled as a prismatic joint. Figure 4.14 shows the piston sub-model. The piston force, Equation 4.45, is the input to the prismatic joint. The piston mass and inertia are added to the prismatic joint and the image file (CAD file) is attached to animate the multi-body model. MapleSim is very powerful advanced modeling environment to handle large systems and generate animation file gives a better insight of complex systems.

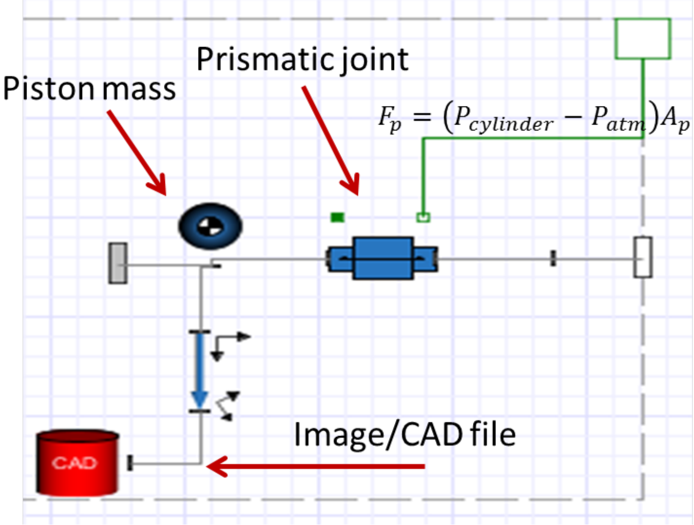

Figure 4.14: Multi-body piston model

The connecting rod and crank are simply modeled by combining rods and mass (inertia) from the MapleSim multi-body library (Figure 4.15).

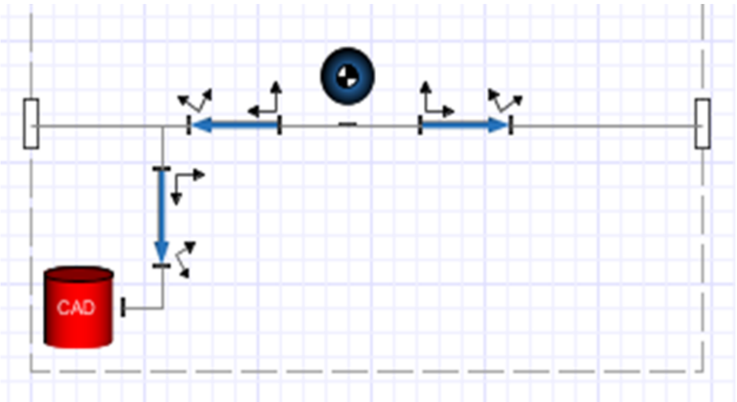

Figure 4.15: Multi-body model of crank and connecting rod

The whole multi-body model can be visualized in the MapleSim as shown in Figure 4.16. The firing order of the four-cylinder model is 1-2-4-3.

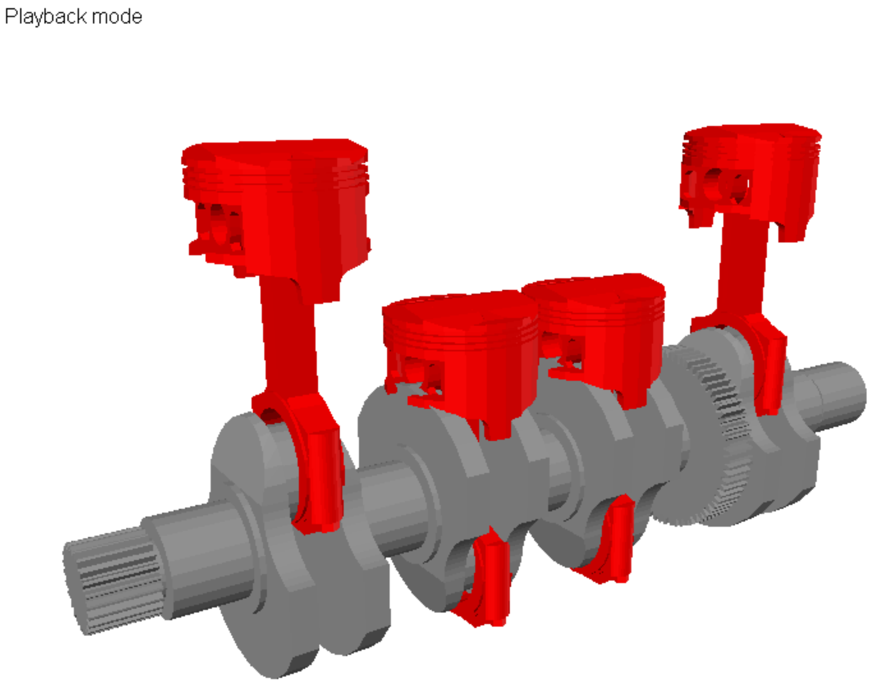

Figure 4.16: 3D animation of the four-cylinder engine model

4.1.7 Dynamometer

Dynamometers are usually employed to test rotational components such as IC engine, torque converter, and tires. Dynamometer can operate in both motor and generator modes. In the motor mode, driver mode, dyno generates mechanical torque (positive torque) to test the component. In the generator mode, driven mode, dyno absorbs mechanical energy and can convert it to electrical energy.

The proposed dynamometer in this research is the permamnent magnet DC motor (PMDCM) which generates mechanical torque to keep the engine's shaft angular speed close to the reference angular speed. The engine's shaft rotational speed must be kept constant during the simulation, because the four-cylinder model based on the two-zone combustion needs the constant rotational speed (rpm) at each cycle.

The dyno sub-model is shown in Figure 4.17. The input to the PMDCM is source of current (i_{dyno}), and the output is resistant torque (load). The shaft's angular speed is controlled with tuning the PID controller so that it tracks the constant reference angular speed (e.g. $n_{Ref} = 3000rpm$). The PID gains are tuned with trial and error method ($K_P = 50$, $t_I = 1s$, and $t_D = 5s$). Equation 4.46 represent the relation between source of current ($i_{dyno}(t)$) with angular speed error signal ($n(t) - n_{Ref}$).

$$i_{dyno}(t) = K_P(n(t) - n_{Ref}) + \frac{K_P}{t_I}\int (n(t) - n_{Ref})dt + K_P t_D \frac{d(n(t) - n_{Ref})}{dt} \tag{4.46}$$

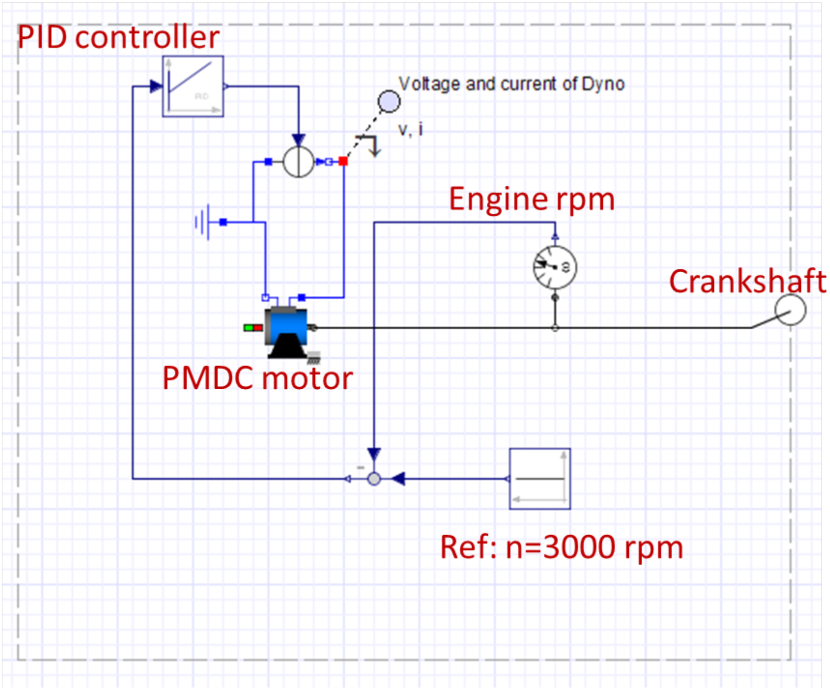

Figure 4.17: Dynamometer sub-model in MapleSim

The resistant torque (τ_R),which delivers to the engine crankshaft, is calculated (Equation 4.47) from the PMDCM electromagnetic torque ($\tau_{ElecMag}$), and armature inertia (I_{arm}) and damping (β_{arm}). The angular velocity of the armature is represented by w_{arm}.

$$\tau_R = \tau_{ElecMag} - I_{arm}\frac{dw_{arm}}{dt} - \beta_{arm}w_{arm} \tag{4.47}$$

The electromagnetic torque ($\tau_{ElecMag}$) is proportional to the input current (i_{dyno}) as shown in Equation 4.48. The torque constant (K_{dyno}) is dependent on the flux density of the electromagnetic field and geometry of the armature.

$$\tau_{ElecMag} = K_{dyno} i_{dyno} \tag{4.48}$$

The simulation results of the multi-body model with dynamometer at different engine angular speeds are presented in the next section.

4.2 Multi-cycle Simulation

In the first step, the integrated two-zone combustion engine model along with the emission prediction model are simulated for one full cycle (720 degrees of crank angle). In the simplest scenario, the single cylinder model with three inputs is simulated. The inputs to the single cylinder model are in-cylinder mass (m_{Cyl}), spark advanced angle (SA), and engine speed (n). The simulation time for four-stroke operation, including emission prediction, in one cycle is faster than real time. The simulations are executed on a 64-bit Windows 7 computer with Intel (R) Core (TM) Duo 3.33 GHz CPU. For instance, the simulation time for one cycle at 3000 rpm is about 0.035 seconds which is faster than real time (0.04 seconds). The single cylinder parameter values, as well as fuel properties, are provided in Table 4.1.

The in-cylinder pressure and volume during four-stroke operation of the single cylinder model are shown as the Otto cycle simulation in Figure 4.18. The P-V diagram, which is similar to the Figure 4.1, depicts the characteristic of the SI engine model.

Table 4.1: SI engine model parameters and values

Fuel ($C_{\Upsilon_1}H_{\Upsilon_2}$)	$\Upsilon_1 = 8, \Upsilon_2 = 18$	Rod length	$0.17[m]$
Equivalence ratio (Φ)	1	Bore diameter	$0.085[m]$
Gas universal constant ($\bar{R}$)	$8.314[J.(mol.K)^{-1}]$	Compression ratio (CR)	10 : 1
Ambient pressure (P_0)	$1[bar]$	Engine speed (n)	$3000[rpm]$
Ambient temperature (T_0)	$293[K]$	Spark advance (SA)	$-30[deg]$
Cylinder wall temperature	$473[K]$	In-cylinder trapped mass	$0.0005[kg]$
Stroke length	$0.1[m]$	Average heat capacity ratio (γ)	1.35

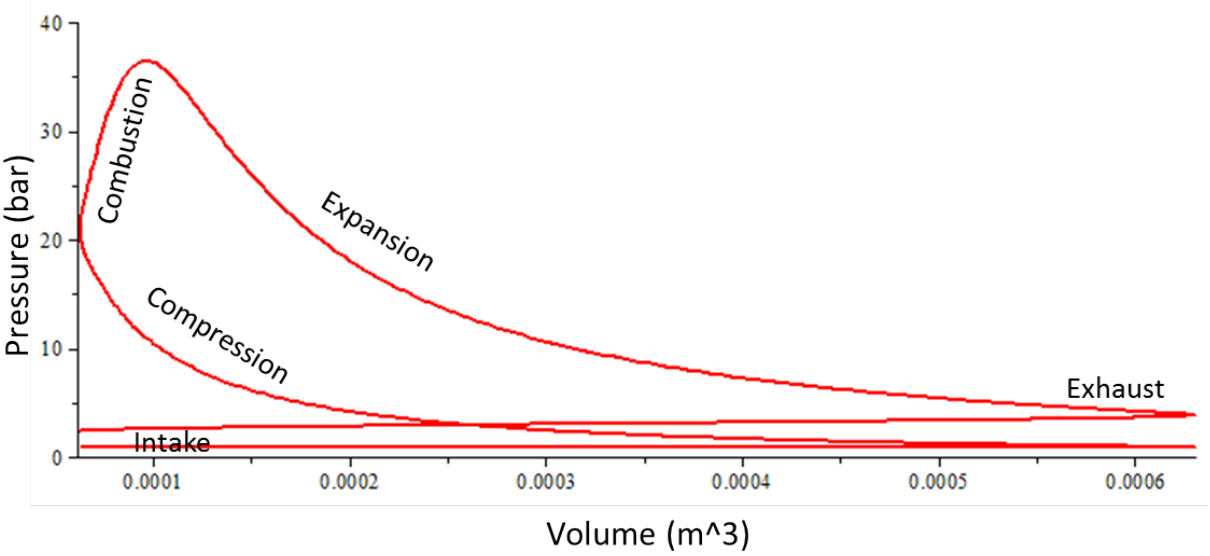

Figure 4.18: P-V Otto cycle simulation of four-stroke operation

The unburned temperature is defined during the intake, compression, and combustion (Figure 4.19). However, the total mixture is fully burned at the end of combustion process and the burned temperature is defined from start of the combustion process to the end of the exhaust stroke as shown in Figure 4.20.

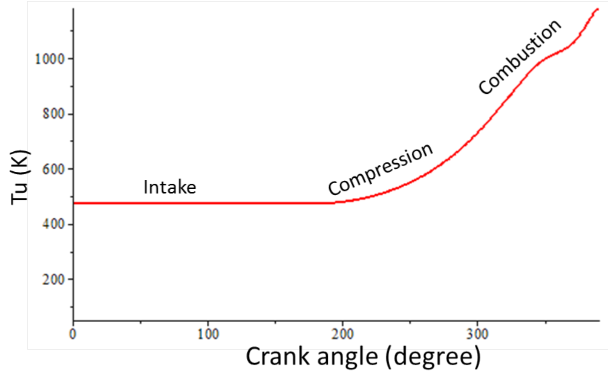

Figure 4.19: Unburned temperature

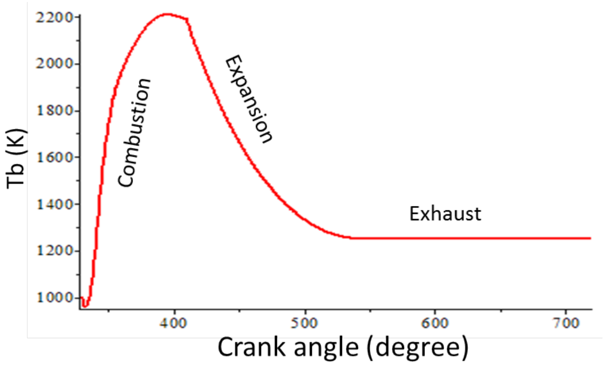

Figure 4.20: Burned temperature

The initial dip in the burned temperature is due to the initial condition. Figure 4.21 depicts that the burned temperature curve is insensitive to the initial conditions, since the simulations converge after the initial combustion time step (or 0.4 degrees of crank angle). That is the initial transient in the burned temperature plot does not affect the final conclusion of the simulation results. The most important data from the burned temperature plot are the overall trend, peak temperature value, and exhaust temperature which are used to calculate the engine performances (e.g. power, emission, and fuel consumption).

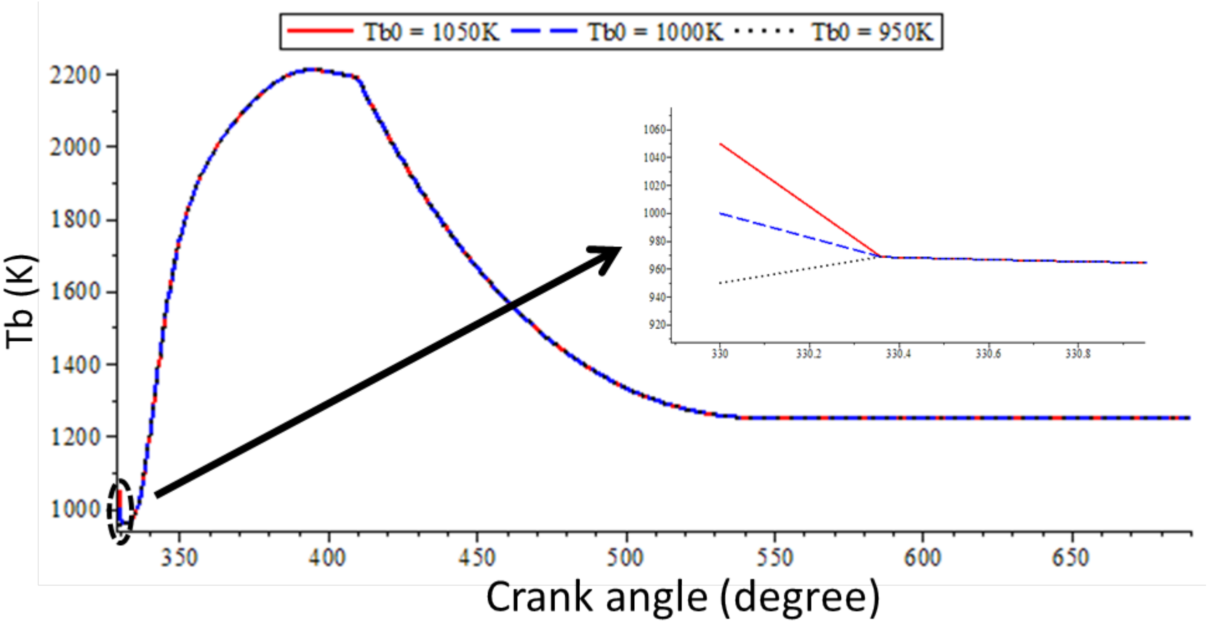

Figure 4.21: Burned temperature profiles for three different initial burned temperature estimates at the start of combustion (i.e. initial conditions for combustion)

The engine torque, which is calculated based on the in-cylinder pressure and volume, is shown in Figure 4.22. The negative torque during compression and exhaust introduces negative work to move the piston from BDC to TDC to compress the mixture during the compression stroke, or to drive out the exhaust gases during the exhaust stroke.

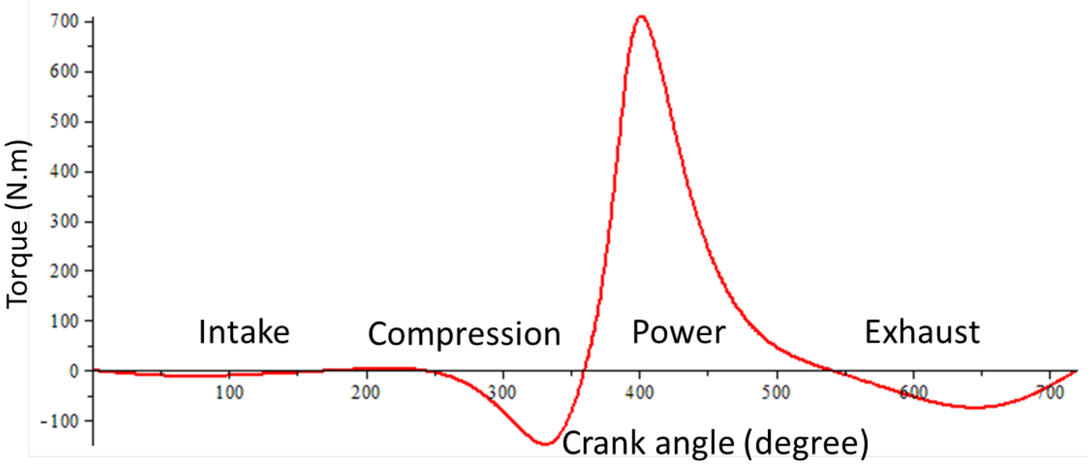

Figure 4.22: Mechanical/brake torque generated during the four-stroke operation

The emission sub-model generates the concentration of eleven species in equilibrium, as shown in Figure 4.23, as well as the solution of chemical kinetics equations (Equations 4.39 and 4.40) for NO and CO as shown in Figure 4.24 and 4.25 respectively. The trends of the emission gases are similar to the literature results [9].

The N_2 equilibrium concentration has the highest molar fraction value at stoichiometric condition, which is in agreement with the molar concentration of the fresh air in the reactants. The H_2O and CO_2 are the next major species in the equilibrium products. The rest of the products have the minor molar fraction contribution in the product as shown in the Figure 4.23. The emission calculation can be repeated at each cycle with different inputs such as spark timing and air-fuel ratio for many simulation cycles.

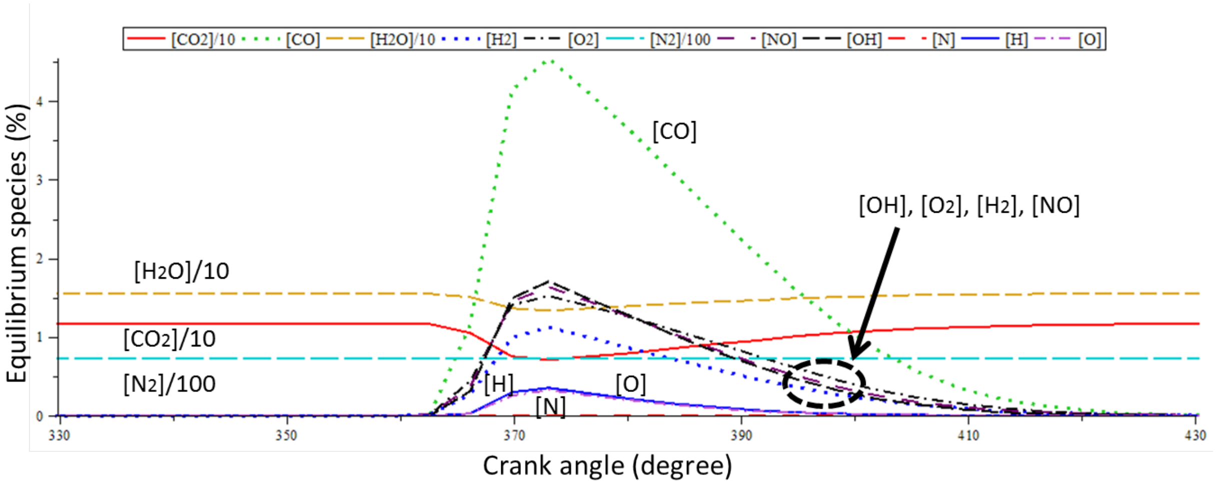

Figure 4.23: Molar fraction of equilibrium species concentration

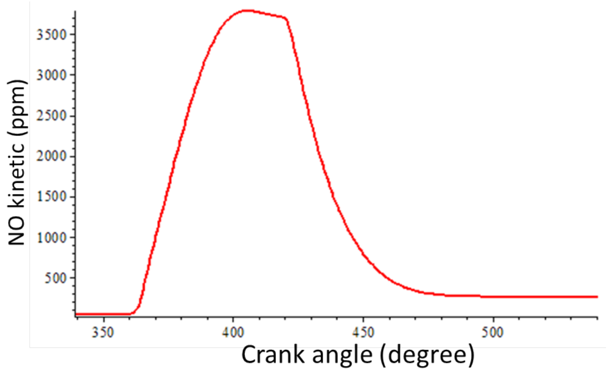

Figure 4.24: Kinetic NO emission

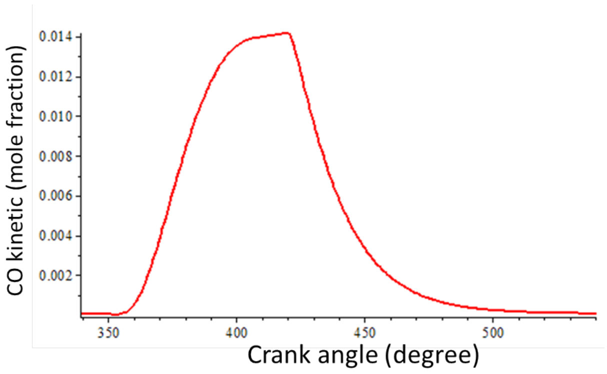

Figure 4.25: Kinetic CO emission

The proposed model can be used to simulate many simulation cycles with variable spark timing. In other words, the spark timing can be changed at any cycle for control purposes. Figure 4.26 represents the in-cylinder pressure simulation of two consecutive cycles in one simulation run with variable spark timing. The in-cylinder pressure curves for two different spark advanced angle at constant engine speed show the significant effect of the spark timing on the engine performance, and the optimum spark advanced angle is defined to obtain the best performance (maximum brake torque/power). For instance, more advanced spark angle, at this specific engine operation, increases the cylinder temperature and consequently the peak pressure is increased. However, much more advanced spark angle burns the air-fuel mixture before piston rises, which causes imperfect and inefficient combustion. The crank angle ($\theta(t)$) is used as a criterion to switch from one cycle to the other cycle. Each cycle takes two full rotations of crank, which is equal to 720 degrees. The floor function in Equation 4.49 is used to define the start of intake stroke at each cycle, and the start of other strokes (e.g. compression, combustion, expansion, and exhaust) is defined based on the start of the previous stroke. For instance, the simulation starts from zero crank angle ($\theta(t) = 0$) and $StartofIntake(t) = 0$, then the whole cycle evolves during 720 degrees. At the end of the first cycle (at $\theta(t) = 720$), the value of the floor function is one, and the value of $StartofIntake(t)$ becomes 720. The whole process of four-stroke operation with new inputs (spark timing) is repeated for the new cycle simulation.

$$\begin{aligned}
&StartofIntake(t) = \lfloor\frac{\theta(t)}{720}\rfloor.720\\
&StartofCompression(t) = StartofIntake(t) + 180\\
&StartofCombustion(t) = StartofCompression(t) + 180 + SA(t)\\
&StartofExpansion(t) = StartofCombustion(t) + BD(t)\\
&StartofExhaust(t) = StartofExpansion(t) + 180\\
&EndofExhaust(t) = StartofExhaust(t) + 180
\end{aligned} \tag{4.49}$$

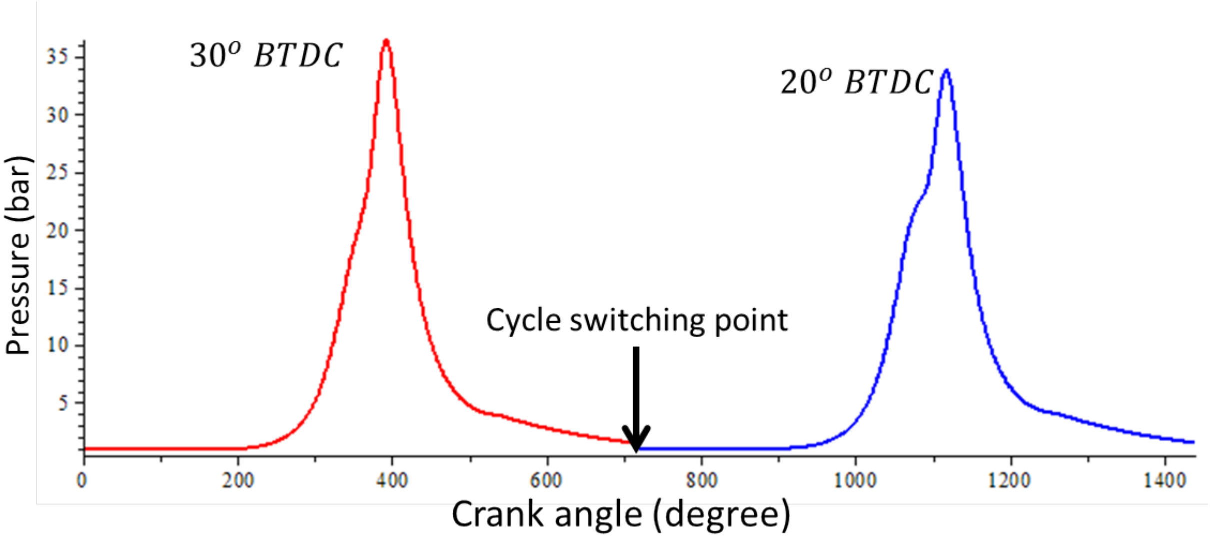

Figure 4.26: Many cycles simulation (variable spark timing) in one simulation time frame

The above simulation results are generated just based on the four-stroke thermodynamic formulation. The more realistic model must include the crankshaft inertia and friction model. The details of the whole components and sub-models are described in the previous section. The following simulation results are generated based on the full model, including multi-body and friction sub-models, at constant engine speed. The main inputs to the four-cylinder engine model are throttle angle and dynamometer load torque. Moreover, the engine speed during the simulation is assumed constant. The spark timing, valve timing, and EGR mass flow rate can be varied from one cycle to the other one.

The model is able to generate many cycles simulation results in one simulation time frame. However, the two-zone combustion assumptions are applied at each cycle (or two fully rotations of the crankshaft). Therefore, the continuous input variables must be discretized at each cycle. The cycle time is defined as a time duration for two fully rotations of the crankshaft. Equation 4.50 represents the relation between the cycle time (*seconds*) and engine speed (*rpm*). For instance, the cycle time at 3000 *rpm* is 0.04 *seconds*.

$$\Delta t_{cycle} = \frac{120}{n} \tag{4.50}$$

The mass flow rate, the output of the intake manifold sub-model, is the input to the cylinders. The total air-fuel mixture is assumed homogenously mixed in the intake manifold. In other words, the injection model is just assumed as the homogenous port injection model. Figure 4.27 shows the mass flow rate delivered into the cylinders and discretized mass flow rate at each cycle. The plot shows the engine operation during 1 *seconds* at 3000 *rpm*, which represents 25 cycles. The discretized curve is identical to the actual continuous mass flow rate after 0.4 *seconds* when the intake manifold state variables (e.g. mass flow rate and pressure) reach to the steady state operation.

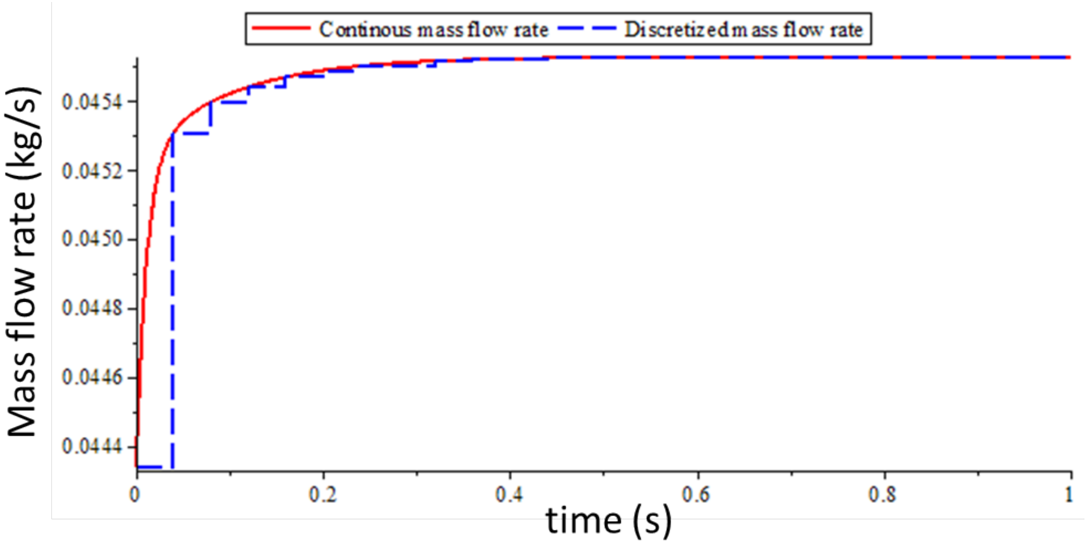

Figure 4.27: Mass flow rate delivered from the intake to the cylinders

The in-cylinder mass during four-stroke operation is shown in Figure 4.28. The mass flow enters to the cylinders during the intake stroke. The mass flow rate in proportional to the piston speed. The rate of the exhaust mass, which leaves the cylinder during the exhaust stroke, is assumed proportional to the piston speed as well. During the compression, combustion, and expansion strokes the intake and exhaust valves are assumed fully closed and the total in-cylinder mass remains constant.

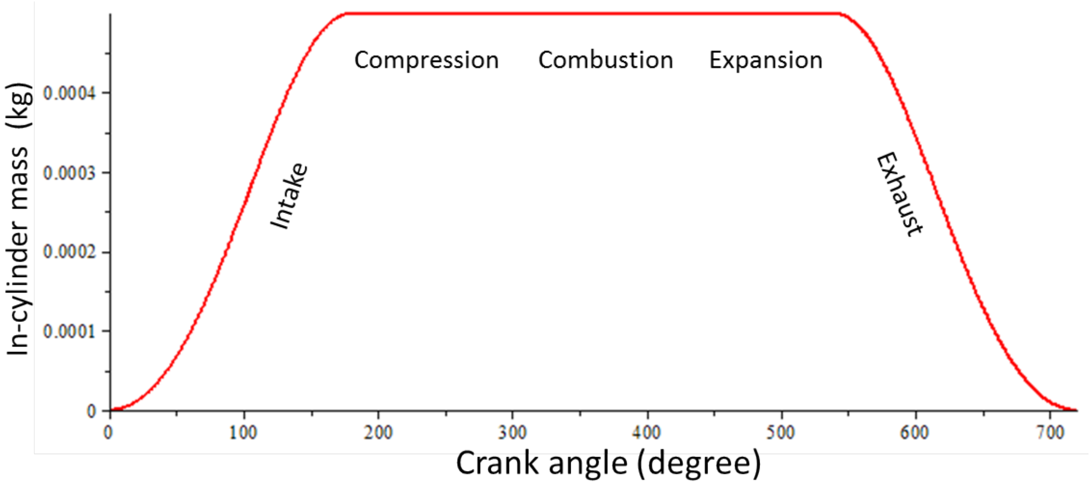

Figure 4.28: In-cylinder mass of the air-fuel mixture during four-stroke operation

In the other hand, the dynamometer generates the load torque to keep the engine shaft's speed as close as possible to the engine operating speed (reference engine speed). Figure 4.29 shows the engine shaft's speed (rpm) and reference engine speed (3000 rpm) at full load operation. The dynamometer, which includes controller and PMDC motor, works well to keep the engine shaft's speed at 3000 rpm. The error, the difference from the actual engine speed and the reference engine speed, is about 0.7 rpm, and the relative error is 0.0002%.

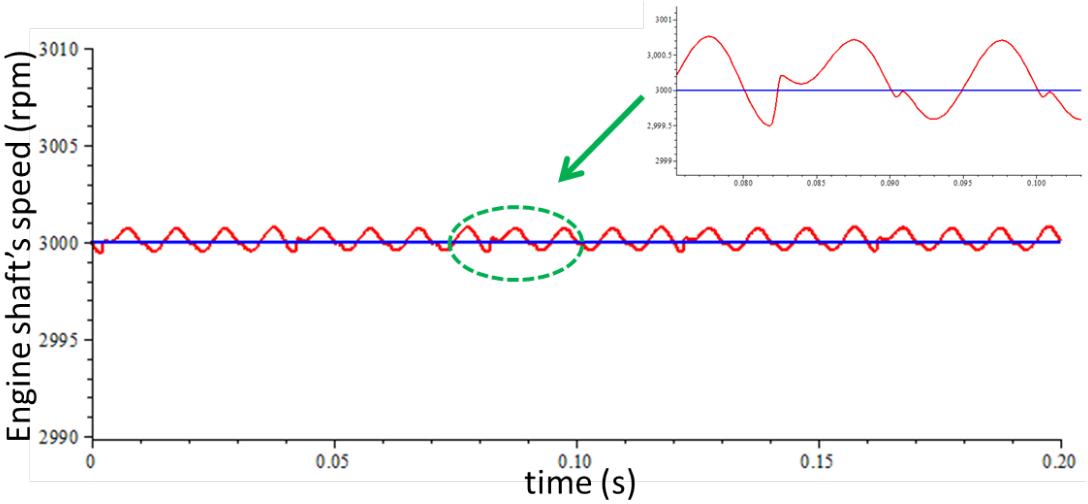

Figure 4.29: Engine shaft's speed (connected to the dynamometer)

The engine brake torque, or shaft's torque, at 3000 *rpm* shows similar oscillations (Figure 4.30). The oscillations are due to the piston movement in a cylinder. In other words, the piston back and forth motion generates the oscillations with two different frequencies as shown in Equation 4.51.

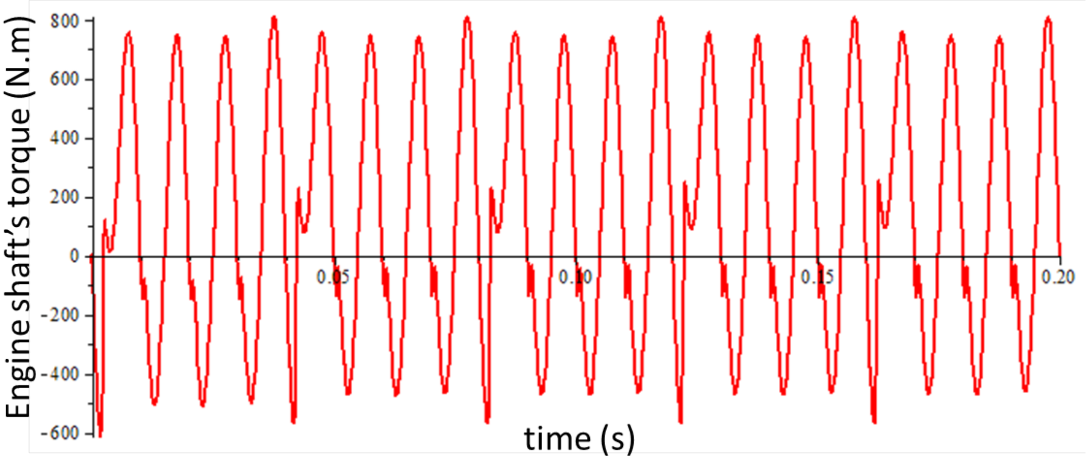

Figure 4.30: Engine shaft's torque (brake torque)

$$U_p(\theta) = \bar{U}_p \frac{\pi}{2} sin(\theta) + \bar{U}_p \frac{\pi}{4} \frac{sin(2\theta)}{\sqrt{\frac{L_{rod}}{r_{crank}} - sin^2(\theta)}} \tag{4.51}$$

The friction model, which is discussed in the previous section by Equations 4.41, 4.42, 4.43, and 4.44, is introduced as the resistant mean effective pressure. The simulation result (Figure 4.31) at different engine speed shows that the in-cylinder friction effect is more significant at higher engine speed (rpm). The friction mean effective pressure is proportional to the piston speed (U_p), and the piston speed is proportional to the engine speed (n). Thus, the friction mean effective pressure is increased by increasing the engine speed. The variation is almost linear as shown in Figure 4.31, which corresponds to the typical experimental plots [1].

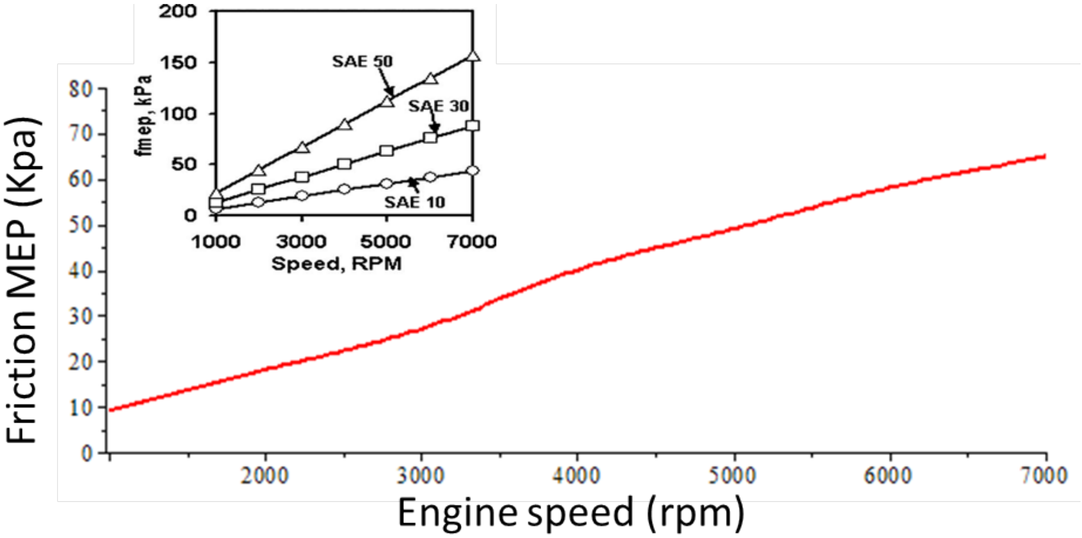

Figure 4.31: Friction mean effective pressure at different engine speed (rpm)

4.3 Model Validation

In this section the developed SI engine model, in MapleSim, is validated against the simulation results from the GT-Power software [34]. GT-Power software, which is the product of Gamma Technology Inc., has been widely used in automotive industry. The models in GT-Power are calibrated and validated with experimental results. Therefore, GT-Power can be used as a reliable reference for validation purposes.

The spark ignition engine models in GT-Power are developed based on the four-stroke with two-zone combustion modelling approach. This makes the GT-Power software more suitable for our SI engine model validation, since our model in the MapleSim is developed based on the two-zone combustion approach. However, the exact mathematical equations can not be viewed in the GT-Power models, but the nature of the equations is same in both GT-Power and MapleSim models. Figure 4.32 shows the full spark ignition model in the GT-Power environment. The model includes all sub-components such as four in-line cylinders, catalytic converter, throttle body, intake and exhaust manifold body.

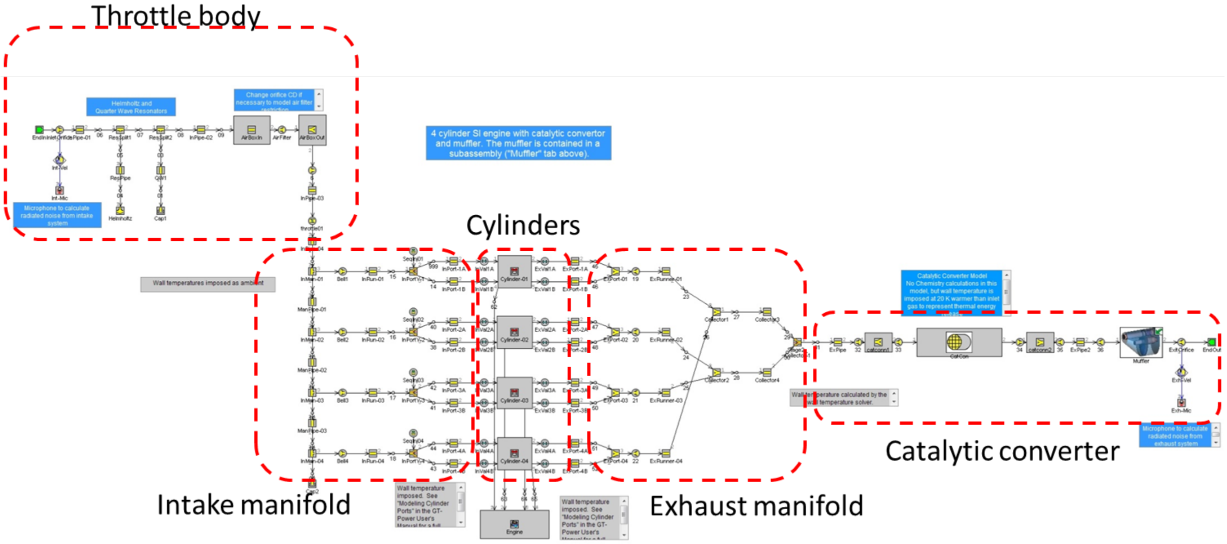

Figure 4.32: Four-cylinder spark ignition engine model in the GT-Power environment

Since the intake and exhaust manifold sub-models in the GT-Power are modeled based on the detailed formulation of the one-dimensional fluid flow, each sub-model must be validated separately. The focus of our study is on in-cylinder variations of the SI engine model such as in-cylinder pressure, burned and unburned temperature. Therefore to validate the cylinder variables during the four-stroke operation, the single cylinder model must be evaluated. For this purpose the simplified model of the SI engine based on the two-zone combustion approach is employed as the reference GT-Power model (Figure 4.33) to validate our SI engine model. The inputs to the single cylinder model is the air and fuel mixture. The model is operating at wide-open-throttle (WOT) at different engine speed (e.g. 3000 rpm)

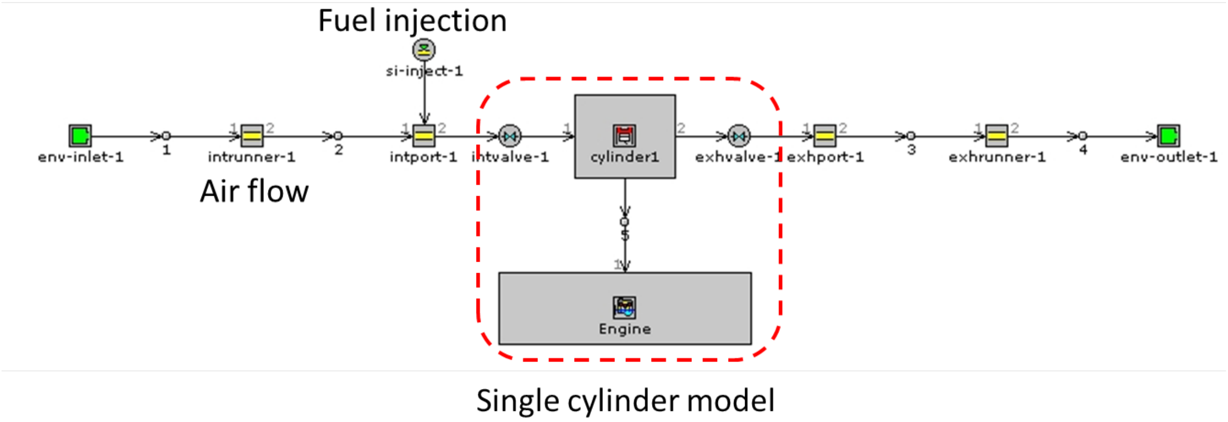

Figure 4.33: Single cylinder spark ignition engine model in the GT-Power environment

The diagram in the Figure 4.34 depicts the validation steps. In the first step, the engine operating condition must be determined. Typically the engine operation is defined by the engine speed and the load acting on the engine (or throttle angle). In this model, the engine is running at wide-open-throttle (WOT) in all cases. The second step is specifying values for the geometrical parameters (e.g. bore, stroke, compression ratio, and connecting rod length) and environmental parameters (ambient temperature, pressure, and cylinder wall temperature). The geometrical and environmental parameters are kept constant during the simulation in both models (MapleSim and GT-Power). The third step is feeding an identical mass flow (or mass flow rate) as the main input to the cylinder.

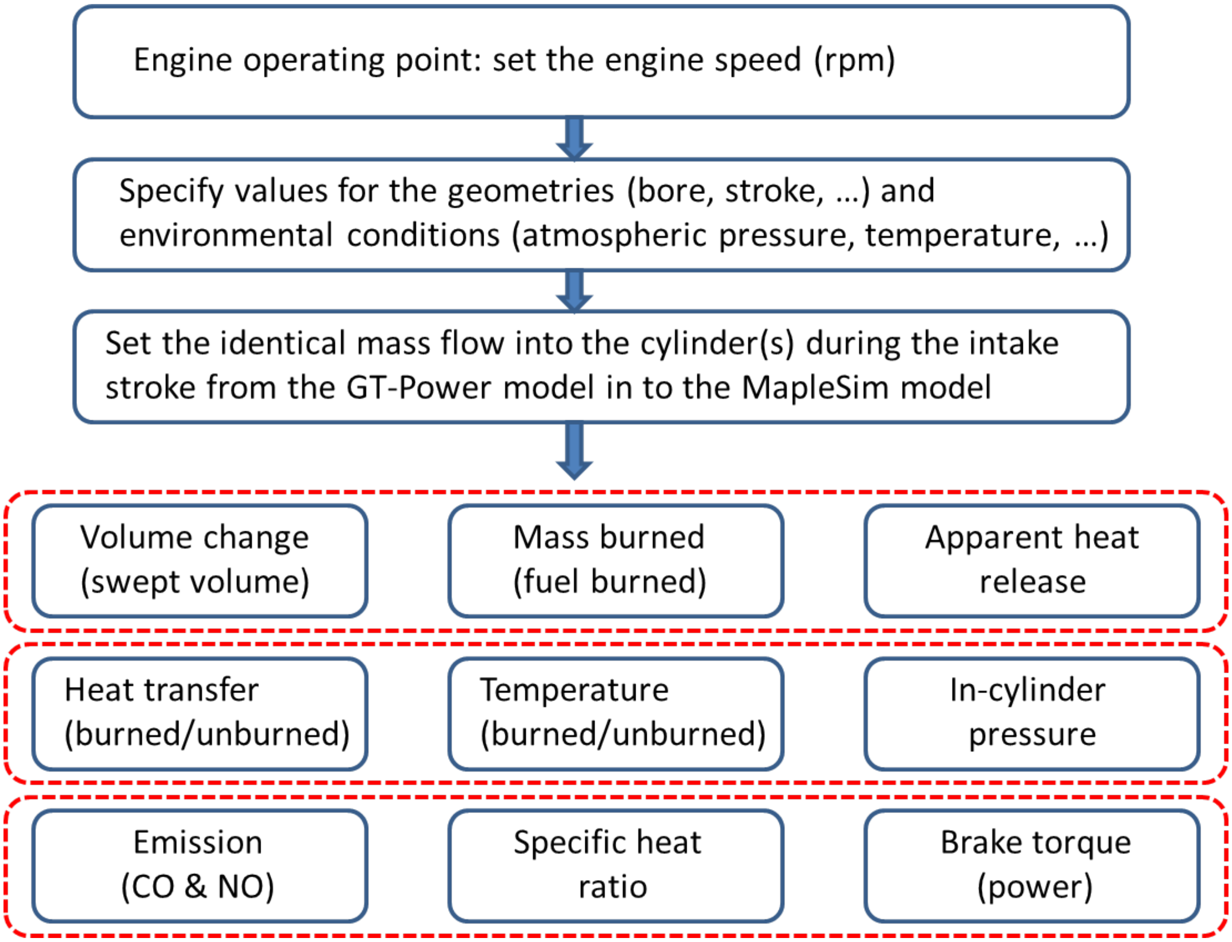

Figure 4.34: Validation steps

The validation variables are categorized in three levels as shown inside the dashed lines (Figure 4.34). In the first level the volume change (swept volume), which purely depends on the geometrical parameters, along with the mass burned rate and heat release during the two-zone combustion process are validated. These variables must be validated precisely, since the next level variables are highly dependent on the first level variables. The second level variables represents the in-cylinder pressure, temperate and heat transfer of the burned and unburned zones. The last set of variables somehow depends on the pressure and temperature. For instance, the NO variation is very sensitive to the peak burned (adiabatic) temperature.

The engine specifications are listed in the Table 4.2. The simulation results are generated at the constant engine speed (e.g. 3000 rpm). Figure 4.35 shows the instantaneous volume, swept volume, during four-stroke operations. The plots are identical, since the swept volume is just function of the engine geometries.

Table 4.2: SI engine model parameters and values (MapleSim and GT-Power model)

In-cylinder trapped mass	$0.0005[kg]$	Engine speed (n)	$3000[rpm]$
Equivalence ratio (Φ)	1	Bore diameter	$0.085[m]$
Gas universal constant ($\bar{R}$)	$8.314[J.(mol.K)^{-1}]$	Compression ratio (CR)	10
Ambient pressure (P_0)	$1[bar]$	Stroke length	$0.1[m]$
Ambient temperature (T_0)	$293[K]$	Inertia	$Ignored$
Cylinder wall temperature	$473[K]$	Rod length	$0.18[m]$

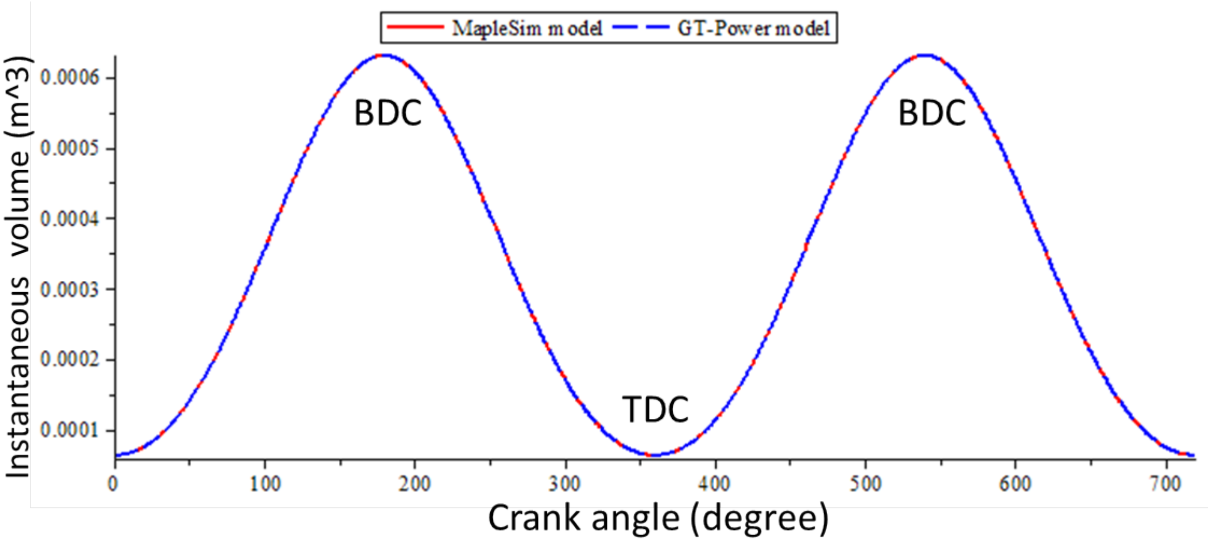

Figure 4.35: Instantaneous in-cylinder volume (MapleSim vs. GT-Power model)

The mass fraction burned is the key variable which significantly affect the in-cylinder thermodynamic properties such as pressure and temperature. Figure 4.36 shows the mass fraction burned of the MapleSim model and GT-Power model (reference model) during the combustion process. The S-shape of the both curves along with the start and the end points are fairly match. The empirical parameters in the Wiebe function (4.9) must be tuned at each operating point. The parameter identification technique, which is presented in the next section, is used to tune the empirical parameters more efficiently. The apparent heat release, the amount of chemical energy released during the combustion process, is shown in the Figure 4.37. The heat release curve follows the S-shape Wiebe function.

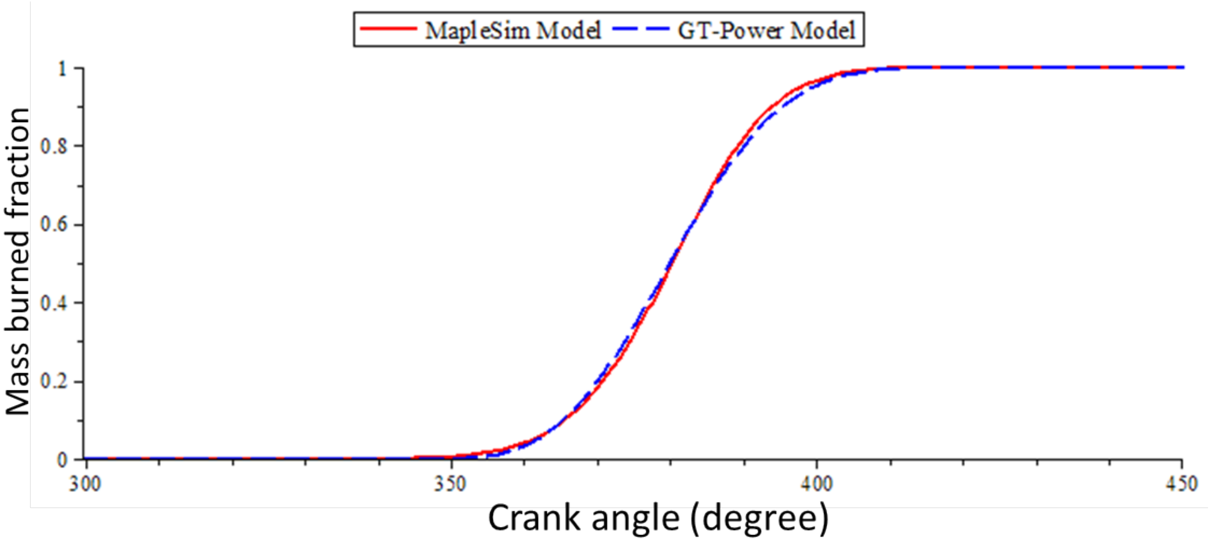

Figure 4.36: Mass fraction burned (MapleSim vs. GT-Power model)

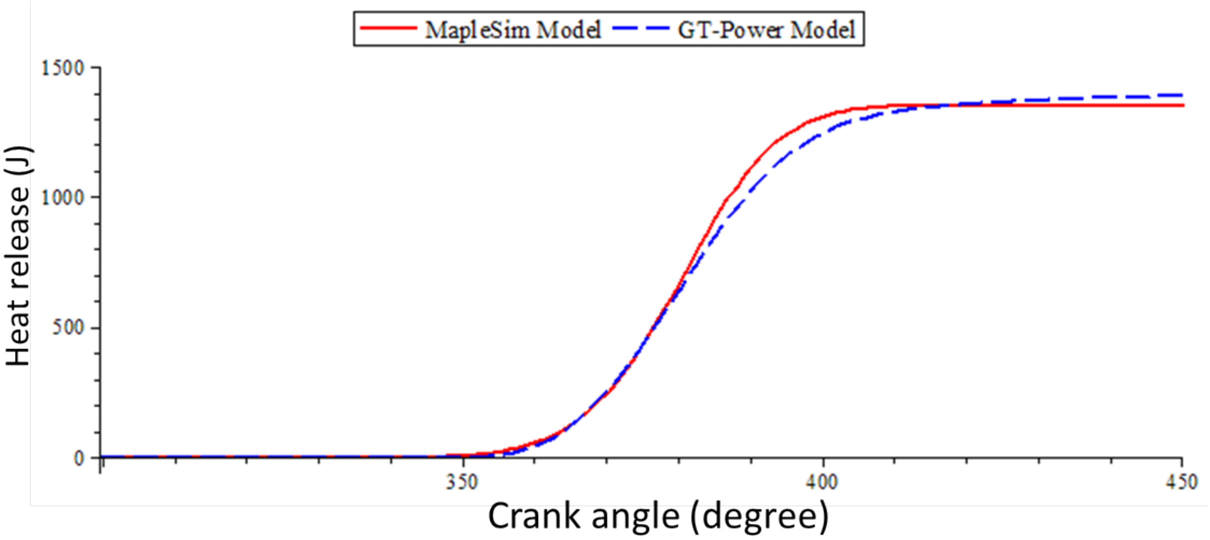

Figure 4.37: Apparent heat release (MapleSim vs. GT-Power model)

The in-cylinder pressure variation during the power stroke is one of the main thermodynamic variable which is measured with pressure sensors. Figure 4.38 compares the in-cylinder pressure during the compression and power strokes of the MapleSim cylinder model against the GT-Power model. The peak pressure and the trend of the pressure curve are very sensitive to the trapped mass and mass fraction burned profile (Wiebe function). The slight difference in the mass burned curve (Figure 4.36), between the MapleSim and GT-Power model, induces the differences in the pressure plots.

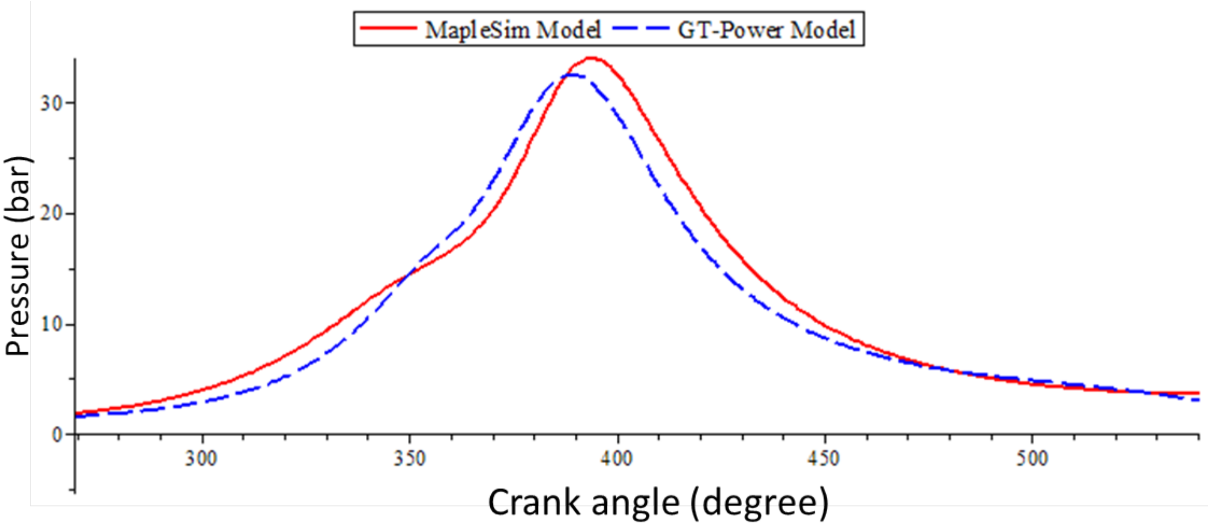

Figure 4.38: In-cylinder pressure (MapleSim vs. GT-Power model)

The heat transfer rate between the burned zone and the cylinder wall affects the burned zone temperature. Figure 4.39 depicts the heat transfer variation during the power stroke (combustion and expansion) based on the Hohenberg correlation model [46]. The corresponding temperature of the burned zone is shown in the Figure 4.40. The temperature during the exhaust stroke is not significantly changed and reaches to 1200 K.

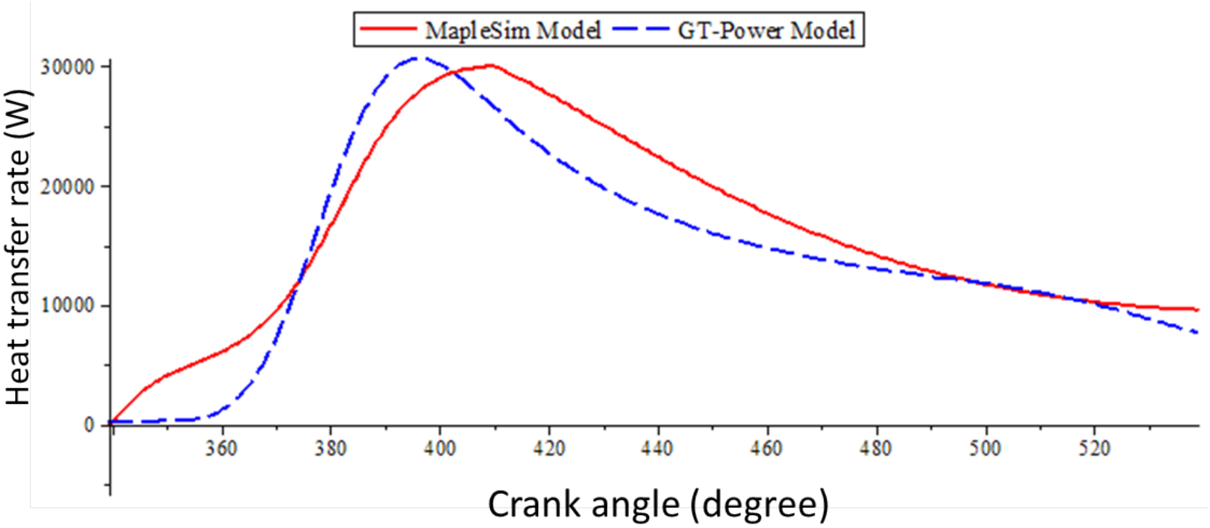

Figure 4.39: Heat transfer rate between burned zone and cylinder wall (MapleSim vs. GT-Power model)

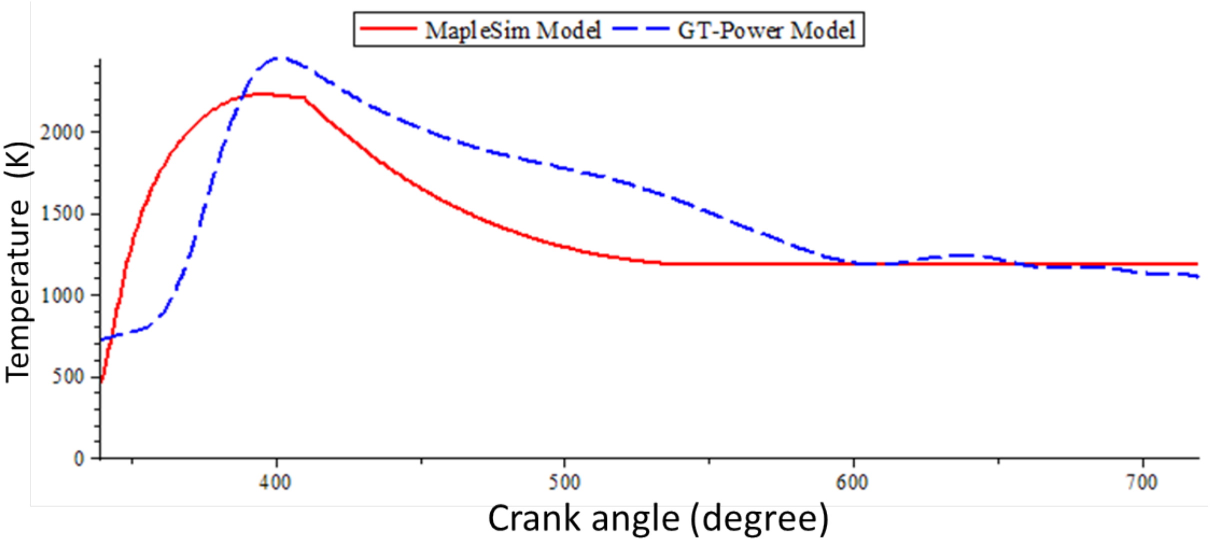

Figure 4.40: Temperature of the burned zone during power and exhaust strokes (MapleSim vs. GT-Power model)

The specific heat ratio varies significantly at high combustion temperature. The unburned specific heat ratio is assumed constant due to the low temperature of the unburned zone, but the burned specific heat ratio is formulated as a function of the burned temperature (Equation 4.16). Figure 4.41 shows the variation of the specific heat ratio during the combustion and expansion process. The specific heat ratio drops at the peak combustion temperature and rises during the expansion stroke.

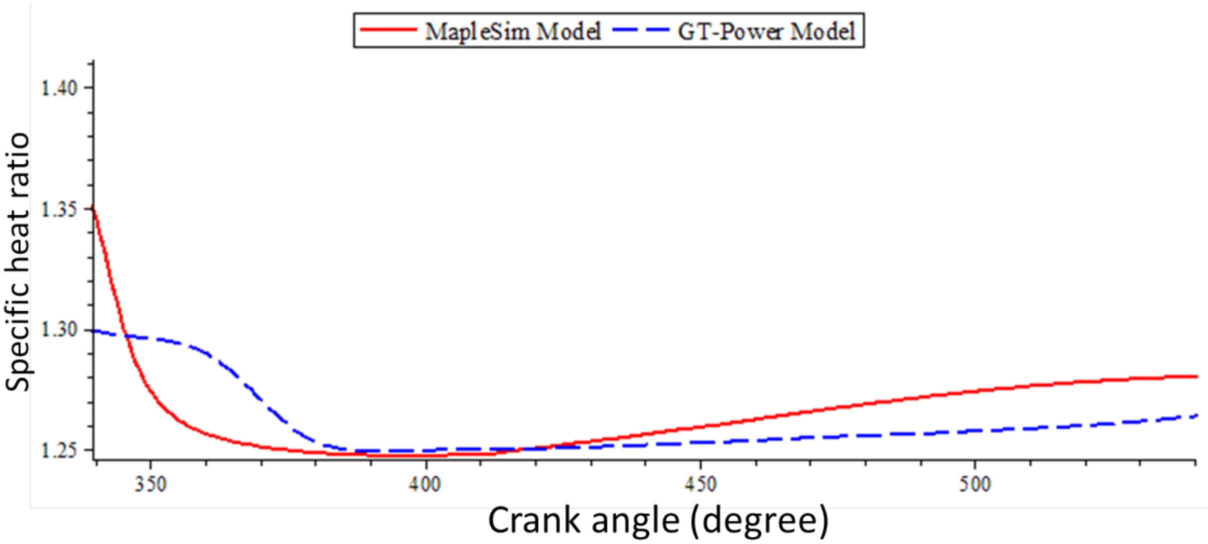

Figure 4.41: Specific heat ratio variation (MapleSim vs. GT-Power model)

The brake torque, or mechanical torque, of the single cylinder model is plotted in the Figure 4.42. The negative part of the torque represents the work needed to compress the in-cylinder mixture during the compression stroke. Then, the spark is ignited and the positive torque (positive work) is generated during the power stroke. The trend of the torque curve is similar to the in-cylinder pressure curve. Moreover, the peak pressure difference between the MapleSim and GT-Power model (Figure 4.38), which is about 2 *bar*, generates the peak torque difference.

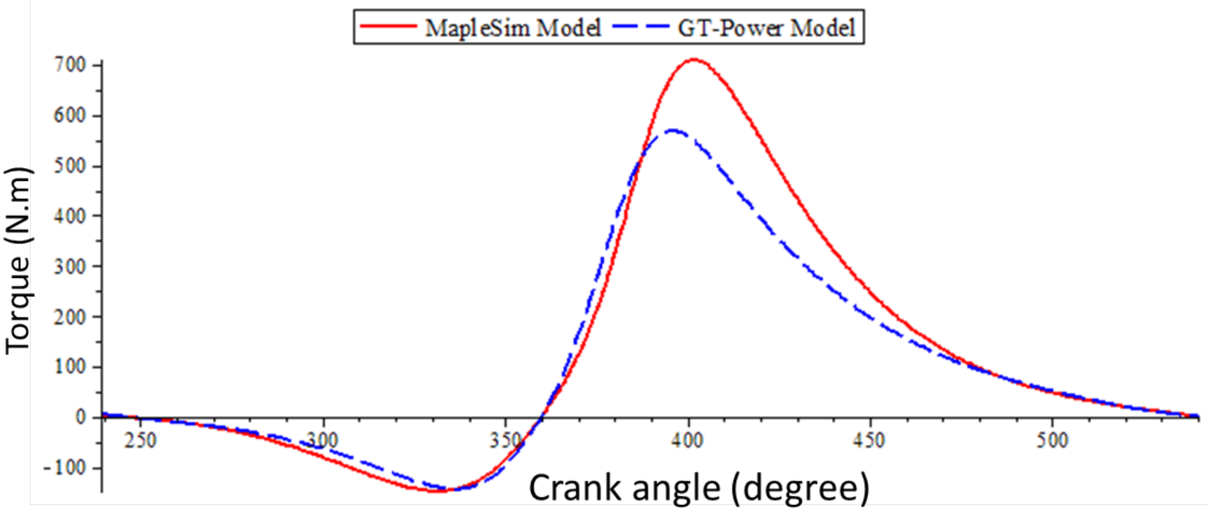

Figure 4.42: Brake torque (mechanical torque) (MapleSim vs. GT-Power model)

The emission sub-model generates the concentration of eleven species in equilibrium as well as the solution of chemical kinetics equations for NO and CO as shown in the Figures 4.43 and 4.44. The trend of both curves (MapleSim and GT-Power model) are fairly similar, but the values are not identical. The differences in the in-cylinder pressure and temperature affect the emission variation.

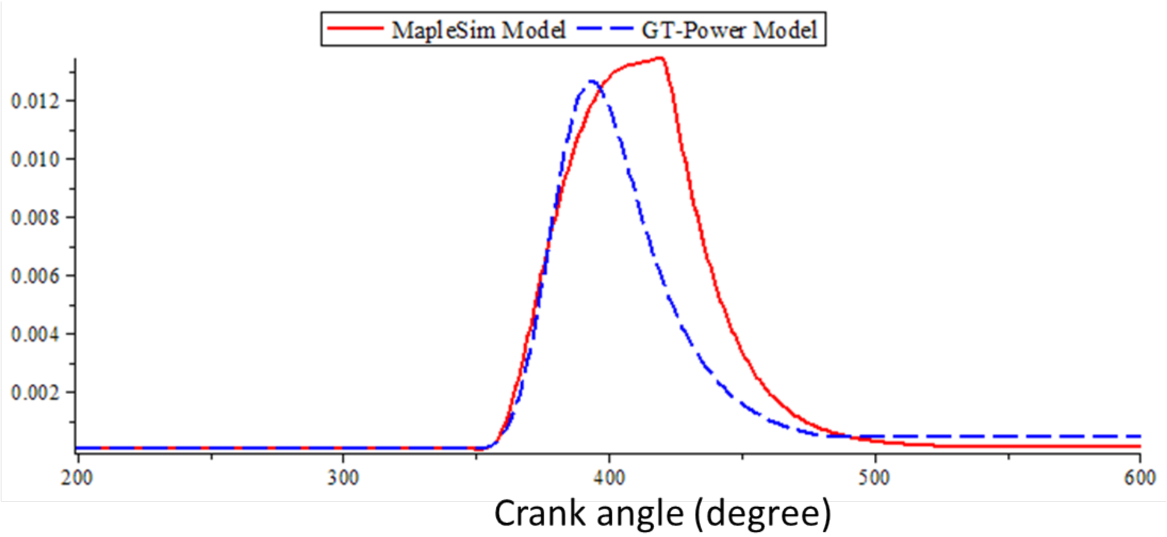

Figure 4.43: Kinetic CO emission (MapleSim vs. GT-Power model)

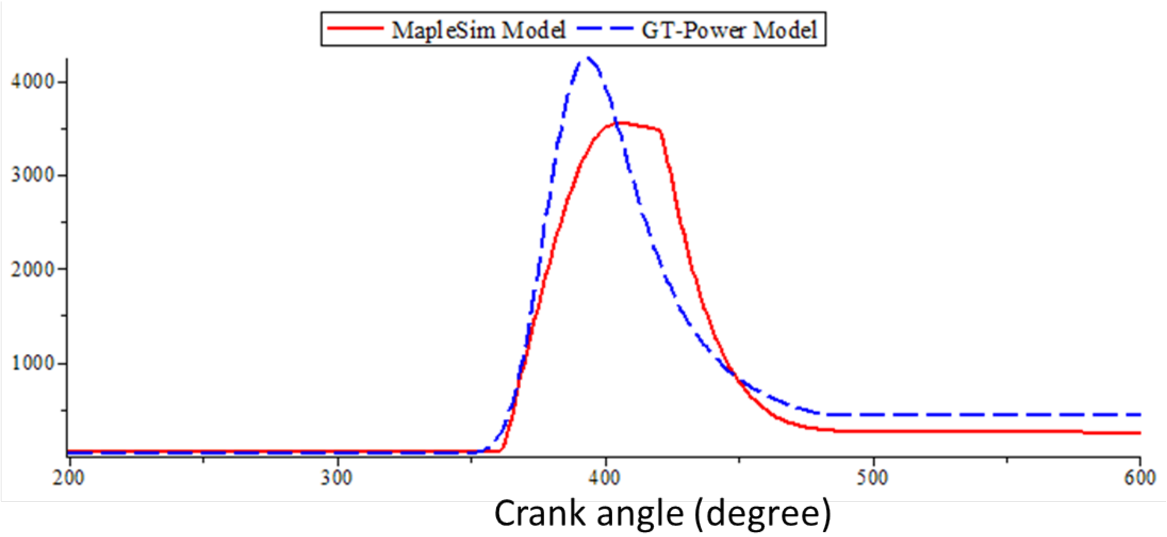

Figure 4.44: Kinetic NO emission (MapleSim vs. GT-Power model)

The above simulation plots depicted a cycle simulation of the developed SI engine model in MapleSim, and cross-validation between the model and the GT-Power model. The following plots show the characteristics (or performance) plots of the models at five engine operating points (1000, 2000, 3000, 4000, and 5000 rpm). Then, the plots are generated by fitting the best curve through the operating points. The brake power in Figure 4.45 is calculated from Equation 4.52, where the brake mean effective pressure (BMEP) is proportional to the average brake torque during a cycle (Figure 4.42). The trends of both MapleSim and GT-Power models are almost identical. However, the brake power in the MapleSim model is slightly more than GT-Power model due to the differences in the brake mean effective pressure (BMEP) or average brake torque value (e.g. see Figure 4.42).

$$Power_{brake} = BMEP.V_d.n \tag{4.52}$$

The brake specific fuel consumption (BSFC), which represents somehow the engine efficiency, is shown in Figure 4.46. Equation 4.53 shows the relation between BSFC and brake power. The fuel mass flow rate ($\dot{m}_{fuel}$) is the identical input to both MapleSim and GT-Power models, and burring condition is assumed stoichiometric at all operating points. Therefore, the BSFC of the developed MapleSim model is lower than the GT-Power model due to the differences in the brake power curves(Figure 4.45).

$$BSFC = \frac{\dot{m}_{fuel}}{Power_{brake}} \tag{4.53}$$

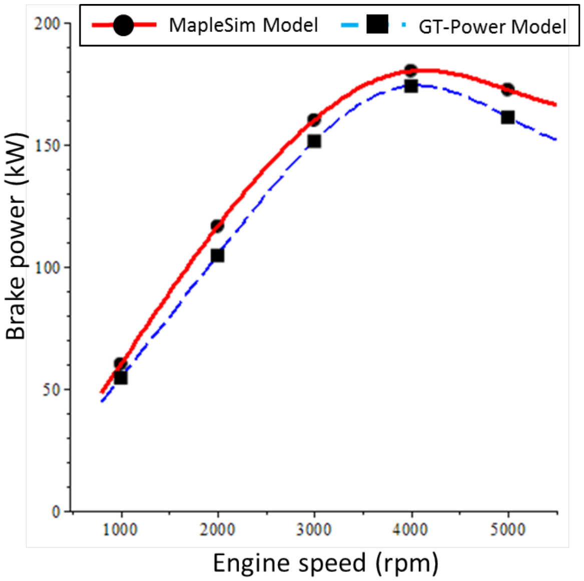

Figure 4.45: Brake power

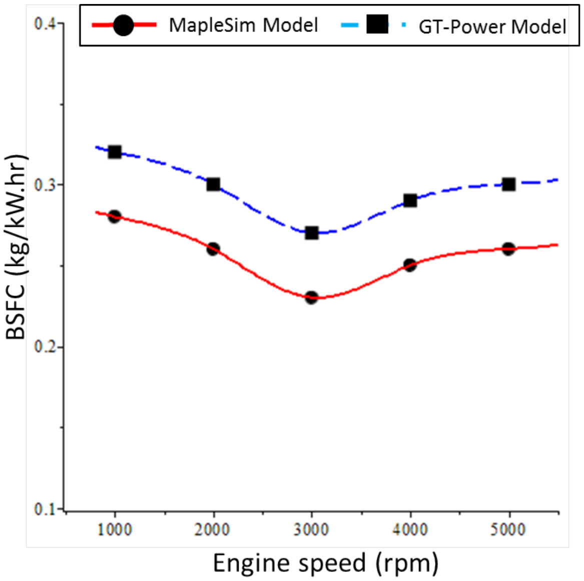

Figure 4.46: Brake specific fuel consumption

Similarly, the specific kinetic emission (CO and NO) is calculated by Equation 4.54 and represented in Figures 4.47 and 4.48. The plots of both MapleSim and GT-Power models show a good agreement in trends, but the values are different due to the differences in the specific fuel consumption (Figure 4.46) as well as mass fraction (e.g. see Figure 4.43 and 4.44).

$$[CO]_{specific} = [\%CO]\frac{\dot{m}_{exhaust}}{Power_{brake}} \tag{4.54}$$

$$[NO]_{specific} = [\%NO]\frac{\dot{m}_{exhaust}}{Power_{brake}} \tag{4.55}$$

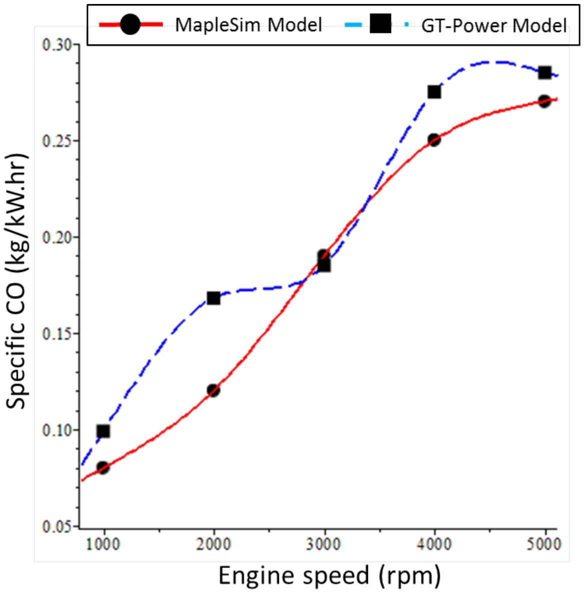

Figure 4.47: Specific CO emission

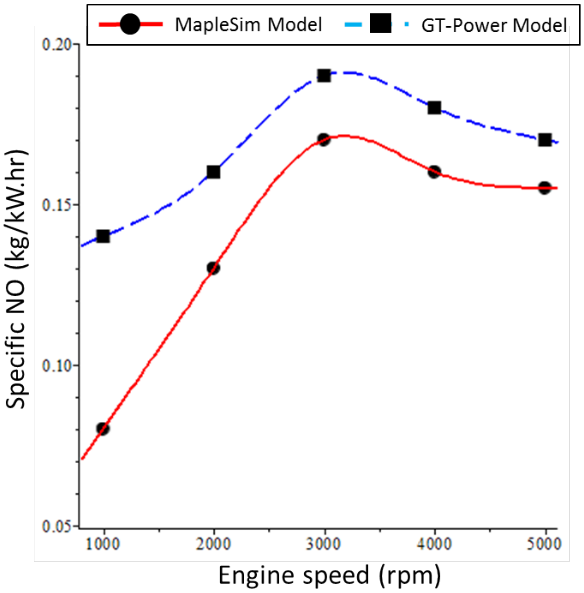

Figure 4.48: Specific NO emission

4.4 Parameter Identification

This section presents parameter identification technique to identify the empirical coefficients in the two-zone combustion SI engine model. The parameter identification technique can be applied to the correlation coefficients of the mass burned model, Hohenberg heat transfer model, intake and exhaust manifold model (e.g. discharge coefficient), and emission chemical kinetic model. The focus of this study is on identifying Wiebe function coefficients to match the mass burned profile with experimental mass burned curve. As discussed earlier, the simulation results of the flame propagation model in the MapleSim are cross validated with the simulation results from the GT-Power software.

The mass burned profile is one of the main inputs which is used to calculate in-cylinder thermodynamic state variables (e.g. pressure, temperature), mechanical torque, and emission gases. Therefore, it is in great importance that the mass burned profile during the combustion process must be calculated accurately.

For this purpose, homotopy optimization method is employed to minimize the error between the experimental data, or GT-Power result, and the result from the math-based SI engine model. Homotopy optimization procedure along with the details of the algorithm steps are described in the reference [83, 84]. Homotopy optimization procedure, in which the original differential equations is modified by coupling the experimental data to the mathematical model using the homotopy parameter and the gains, has been utilized in this research work to guarantee achieving a global minimum. The method has been successfully applied for simple dynamic models [83] and complex dynamic systems [78] for parameter identification purposes.

The following equations show the homotopy formulation to optimize states of a dynamic system. Although more details of the homotopy formulation are provided in the references [24, 29, 83]. A typical dynamic physical system is represented as a combination of ordinary differential equations and algebraic constraints (Equation 4.56), which makes the set of differential-algebraic equations (DAEs). The algebraic constrains must be satisfied at each time step to update the new states (x). The objective of using parameter identification technique is to identify some unknown parameters (ξ) of the system (DAEs).

$$\begin{cases} \dot{x}(t,\xi) = f(t,x,\xi) \quad , x(0,\xi) = x_0 \\ g(t,x,\xi) = 0 \end{cases} \tag{4.56}$$

In a homotopy formulation, the dynamic equation of a system is rearranged to include the homotopy gain (K_{HT}) and the homotopy parameter (ς_{HT}) as shown in the Equation 4.57. The homotopy parameter (ς_{HT}) is set to one at the start of the optimization, and decrements at each time step during the optimization. At the end of the optimization the homotopy parameter is zero and the objective function (Equation 4.58) reaches to its global minima.

$$\dot{x}(t,\xi) = f(t,x,\xi) + \varsigma_{HT} K_{HT} \left(x_{Ref} - x\right) \tag{4.57}$$

$$J(\xi) = \frac{1}{2} \sum_{j=1}^{n} \left(\int_0^T \left(x_{Ref}^j - x^j(\xi,t)\right) dt \right) \tag{4.58}$$

The equations are derived in the Maple worksheet and the homotopy optimization simulation is executed in the Matlab environment by collaboration with Dr. Ramin Masoudi [57]. The homotopy gain is set to one ($K_{HT} = 1$), and the homotopy parameter is decrementing with fixed value ($\Delta\varsigma_{HT} = 0.25$). As mentioned before, the goal of applying homotopy optimization is identifying empirical parameters (a_1 and a_2) of the Wiebe function (Equation 4.9). The initial guess of the unknown (empirical) parameters are chosen arbitrary. For instance, in this simulation the initial values of the empirical Wiebe parameters are set to one for both a_1 and a_2. The final values of the Wiebe empirical parameters, at the end of the simulation, are $a_1 = 2.2248$ and $a_2 = 2.1169$. The normalized mass burned rate, during the combustion process, of the GT-Power model (reference data) and the MapleSim model with initial guesses and optimized parameters are plotted in the Figure 4.49.

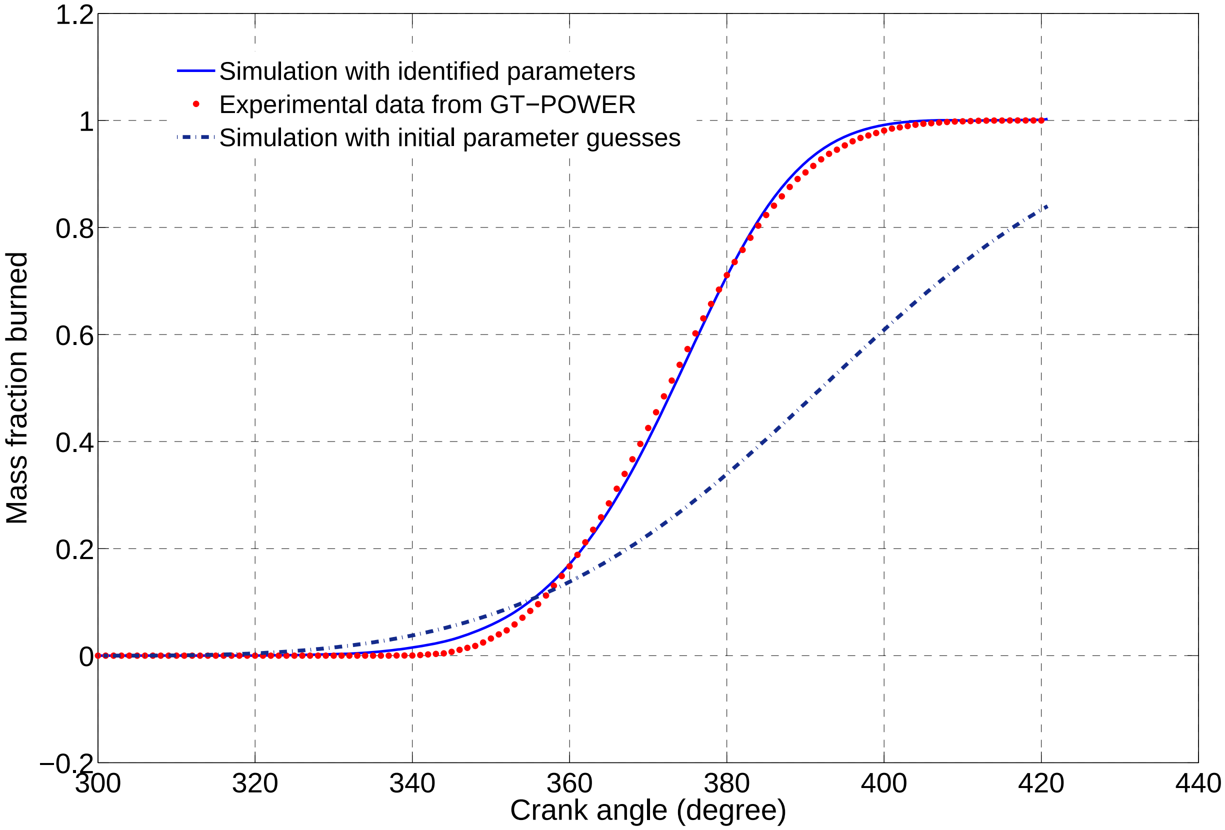

Figure 4.49: Mass fraction burned (homotopy optimization simulation)

4.5 Sensitivity analysis

This section presents parametric sensitivity analysis of the single cylinder SI engine model. Sensitivity analysis is the study of the model's parameters, and their effect on the model outputs or performance [72]. Cylinder design parameters such as bore, stroke, and compression ratio, play an important role to achieve higher performance (e.g. power) and reduce undesirable in-cylinder phenomenon (e.g. knocking). A symbolic sensitivity analysis is used to study the effect of the design parameters on the SI engine performance. The symbolic nature of the Maple/MapleSim environment results in very fast and efficient simulation [73]. It also facilitates a sensitivity analysis that identifies the critical parameters for design and control purposes. Among various schemes used in the sensitivity analysis of dynamical systems, internal differentiation is used in this research project due to its reliability and robustness [63].

In this research [6], sensitivity of the flame propagation states (e.g. turbulent flame speed, mass burned rate), in-cylinder pressure, and mechanical torque through the combustion process with respect to the design parameters such as bore diameter and stroke length are evaluated. However, the sensitivity analysis can be extended for the whole four-stroke operation as well as emission sub-model.

A two-zone modeling formulation can be categorized into the flame propagation model and in-cylinder thermodynamic formulation. However, the state variables of the flame propagation model is used as the inputs to the in-cylinder thermodynamic model to calculate pressure, temperature, and power. The flame propagation model includes two differential and three algebraic equations, which must be solved simultaneously at each crank angle to calculate flame propagation state variables such as burned/unburned mass, burned/unburned volume, and entrained flame mass. The in-cylinder thermodynamic model adds three differential equations to the flame propagation DAEs to calculate in-cylinder pressure, burned and unburned temperature. The set of DAEs is expressed in the Equation 4.59, and a dynamic sensitivity equation is derived in the Equation 4.60. $\L_j$ is the vector represents of the state variables with respect to the j^{th} parameters (ξ_j). The sensitivity equations are generated in the Maple worksheet by collaboration with Dr.

Ramin Masoudi, and then the whole DAEs are solved in the MapleSim software.

$$\begin{cases} \dot{x}(t,\xi) = f(t,x,\xi) \quad , x(0,\xi) = x_0 \\ g(t,x,\xi) = 0 \end{cases} \tag{4.59}$$

$$\dot{\text{Ł}}_j = \left(\frac{\partial f}{\partial x}\right) \text{Ł}_j + \left(\frac{\partial f}{\partial \xi_j}\right) \tag{4.60}$$

The set of DAE equations of the flame propagation model and the in-cylinder thermodynamic model are solved simultaneously with an appropriate stiff solver to generate sensitivity functions. The parameters value of the two-zone combustion model is listed in the Table 4.1, and the sensitivity functions of the state variables are generated with respect to the bore diameter and stroke length. The nominal value of the bore diameter ($\bar{B}$) and the stroke length ($\bar{L}$) are $0.085m$ and $0.1m$ respectively. However, by changing the nominal values the new sensitivity functions are regenerated. In other words, the sensitivity function simulation result is just valid for the specific values of the bore diameter and stroke length.

The sensitivity of the mass burned profile with respect to the cylinder bore diameter and the stroke length, through the combustion process, is shown in Figures 4.50 and 4.51. The sign of the sensitivity function (e.g. negative for bore) means that by increasing the bore diameter the amount of mass is decreased at the same crank angle. Similarly, the positive sign of sensitivity plot with respect to the stroke length shows that the mass burned value is increases by increasing the stroke length from the nominal value. Moreover, the peak value of the plots indicates the maximum sensitivity happens at the specific crank angle corresponding to the peak value. Figure 4.52 shows the mass burned variations (kg) at nominal bore and stroke values ($\bar{B}, \bar{L}$) and the small perturbation from the nominal values ($\bar{B} \pm \Delta B, \bar{L} \pm \Delta L$). The curves of the Figure 4.52 from the nonlinear DAEs flame propagation model approve the trend and the sign of the sensitivity functions.

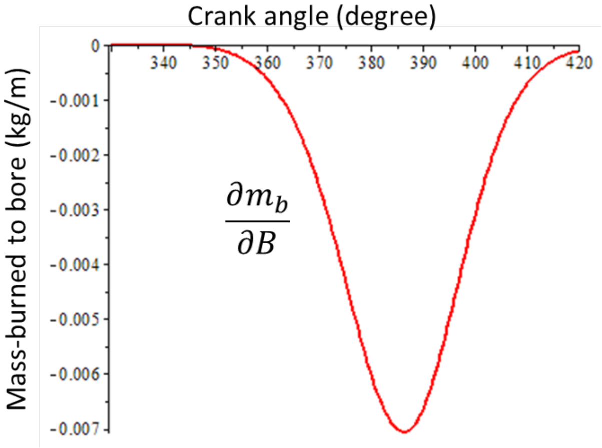

Figure 4.50: Mass burned sensitivity function with respect to the bore diameter

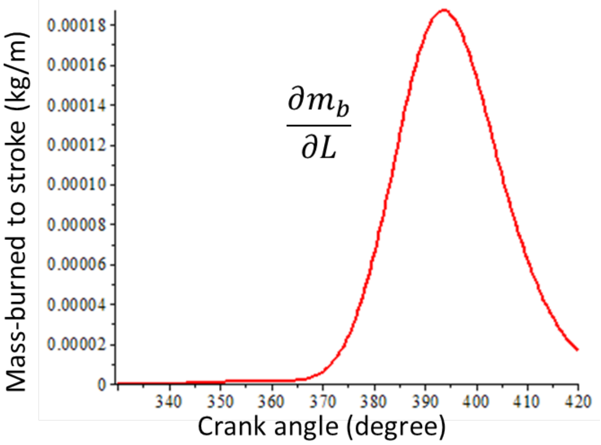

Figure 4.51: Mass burned sensitivity function with respect to the stroke length

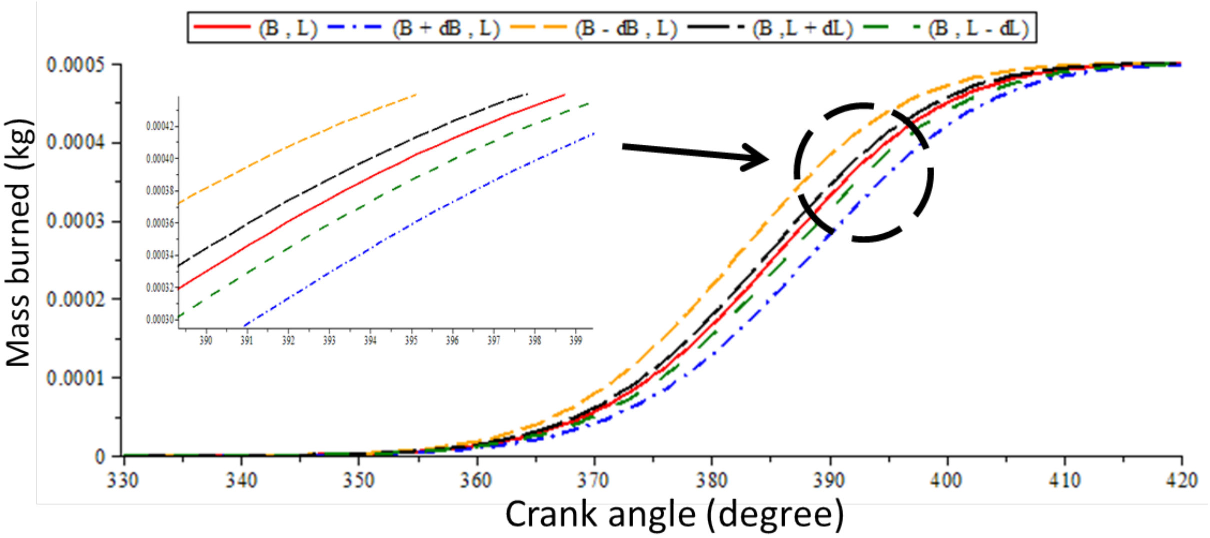

Figure 4.52: Mass burned variations for different perturbations from the nominal values

The turbulent flame speed model is an algebraic equation in the flame propagation DAEs formulation. The turbulent flame speed (U_t) is explicitly represented as a function of unburned density in the Equation 4.3, which is a function of the main state variables of the model (e.g. m_b). Therefore, the sensitivity function of the turbulent flame speed with respect to the bore (or stroke) parameter can be formulated as shown in the Equation 4.61, where f^{U_t} is the right hand side of the Equation 4.3. The sensitivity function of the turbulent flame speed respect to the bore diameter, Figure 4.53, shows that the turbulent flame speed decreases at the start of the combustion and then increases by increasing the bore diameter. Figure 4.54 depicts the sensitivity of the turbulent flame speed with respect to the stroke length. The negative sign of the curve during the combustion process means that the turbulent flame speed decreases through the combustion chamber by increasing the stroke length and vice versa. The characteristics of the sensitivity functions are verified in the Figure 4.55, which shows variation of the turbulent flame speed curve for positive/negative deviation of the design parameters (bore/stroke) from the nominal values.

$$\frac{\partial U_t}{\partial \xi_j} = \left(\frac{\partial f^{U_t}}{\partial m_b}\right) \L_j^{m_b} + \left(\frac{\partial f^{U_t}}{\partial \xi_j}\right) \tag{4.61}$$

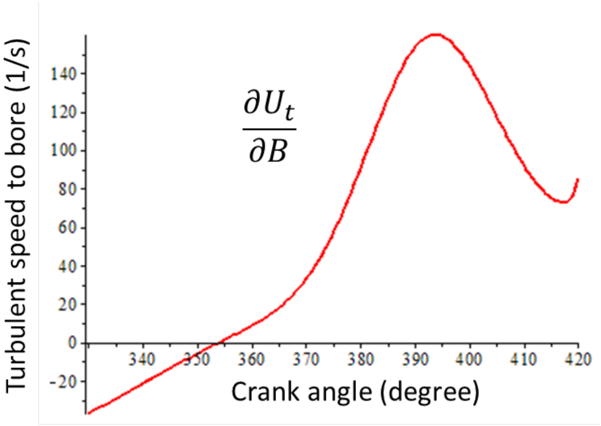

Figure 4.53: Turbulent flame speed sensitivity with respect to the bore diameter

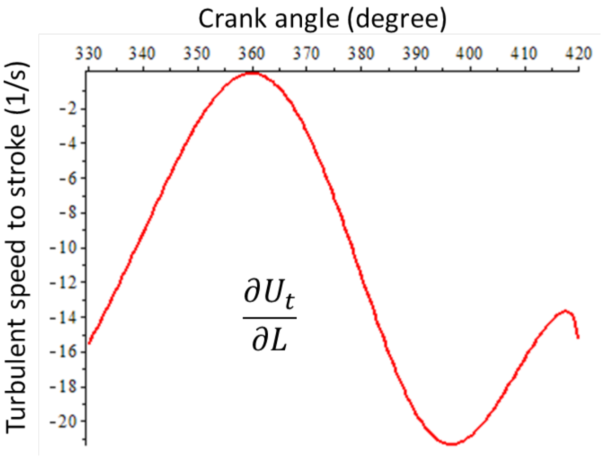

Figure 4.54: Turbulent flame speed sensitivity with respect to the stroke length

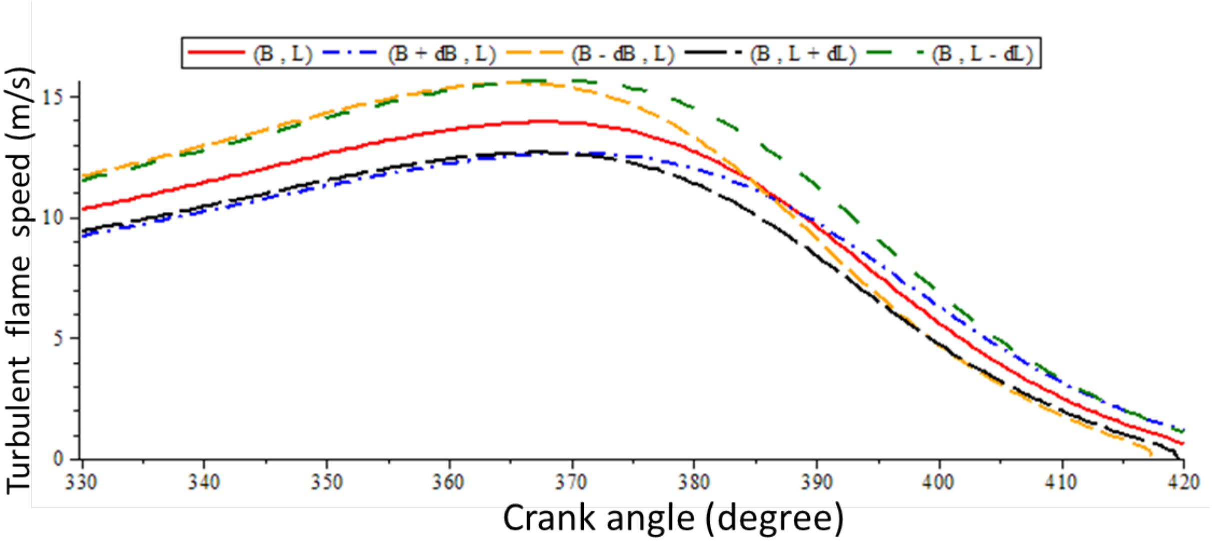

Figure 4.55: Turbulent flame speed variations for different perturbations from the nominal values

The simulation results are extended for the in-cylinder pressure and mechanical torque variation with respect to the design parameters during the combustion process. Since the pressure, burned temperature, and unburned temperature are all nonlinear first order differential equations, the corresponding sensitivity functions of the new states are integrated with the flame propagation sensitivity functions ($Ł_j^x$) to symbolically generate the sensitivity graphs of the DAEs (Equation 4.62). Figures 4.56 and 4.57 represent the solution of the sensitivity equations of the in-cylinder pressure with respect to the bore diameter and stroke length. The peak pressure during the combustion process is very sensitive to both bore diameter and stroke length. The total mass inside the combustion chamber is constant during the combustion process. Therefore by increasing the combustion chamber volume, the peak pressure drops at the same operating conditions (Figure 4.58).

$$\begin{pmatrix} \dot{\text{Ł}}_j^{m_e} \\ \dot{\text{Ł}}_j^{m_b} \\ \dot{\text{Ł}}_j^{P} \\ \dot{\text{Ł}}_j^{T_b} \\ \dot{\text{Ł}}_j^{T_u} \end{pmatrix} = \begin{pmatrix} \frac{\partial f^{m_e}}{\partial m_e} & \frac{\partial f^{m_e}}{\partial m_b} & \frac{\partial f^{m_e}}{\partial P} & \frac{\partial f^{m_e}}{\partial T_b} & \frac{\partial f^{m_e}}{\partial T_u} \\ \frac{\partial f^{m_b}}{\partial m_e} & \frac{\partial f^{m_b}}{\partial m_b} & \frac{\partial f^{m_b}}{\partial P} & \frac{\partial f^{m_b}}{\partial T_b} & \frac{\partial f^{m_b}}{\partial T_u} \\ \frac{\partial f^{P}}{\partial m_e} & \frac{\partial f^{P}}{\partial m_b} & \frac{\partial f^{P}}{\partial P} & \frac{\partial f^{P}}{\partial T_b} & \frac{\partial f^{P}}{\partial T_u} \\ \frac{\partial f^{T_b}}{\partial m_e} & \frac{\partial f^{T_b}}{\partial m_b} & \frac{\partial f^{T_b}}{\partial P} & \frac{\partial f^{T_b}}{\partial T_b} & \frac{\partial f^{T_b}}{\partial T_u} \\ \frac{\partial f^{T_u}}{\partial m_e} & \frac{\partial f^{T_u}}{\partial m_b} & \frac{\partial f^{T_u}}{\partial P} & \frac{\partial f^{T_u}}{\partial T_b} & \frac{\partial f^{T_u}}{\partial T_u} \end{pmatrix} \begin{pmatrix} \text{Ł}_j^{m_e} \\ \text{Ł}_j^{m_b} \\ \text{Ł}_j^{P} \\ \text{Ł}_j^{T_b} \\ \text{Ł}_j^{T_u} \end{pmatrix} + \begin{pmatrix} \frac{\partial f^{m_e}}{\partial \xi_j} \\ \frac{\partial f^{m_b}}{\partial \xi_j} \\ \frac{\partial f^{P}}{\partial \xi_j} \\ \frac{\partial f^{T_b}}{\partial \xi_j} \\ \frac{\partial f^{T_u}}{\partial \xi_j} \end{pmatrix} \tag{4.62}$$

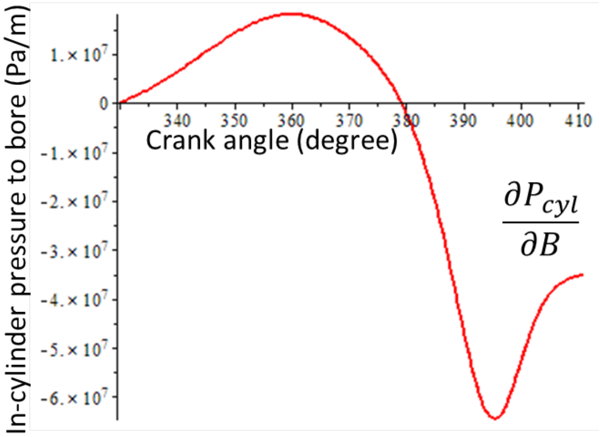

Figure 4.56: Turbulent flame speed sensitivity with respect to the bore diameter

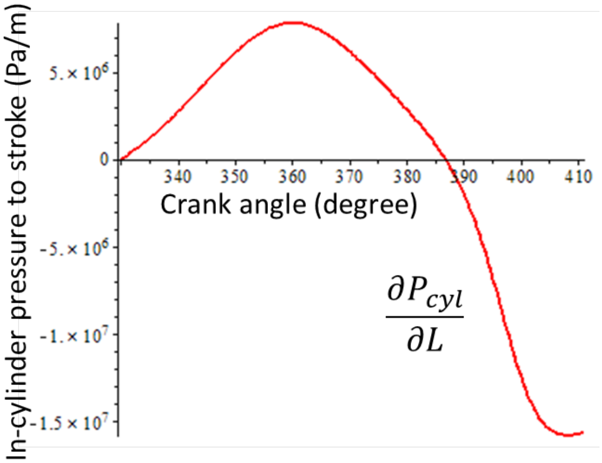

Figure 4.57: Turbulent flame speed sensitivity with respect to the stroke length

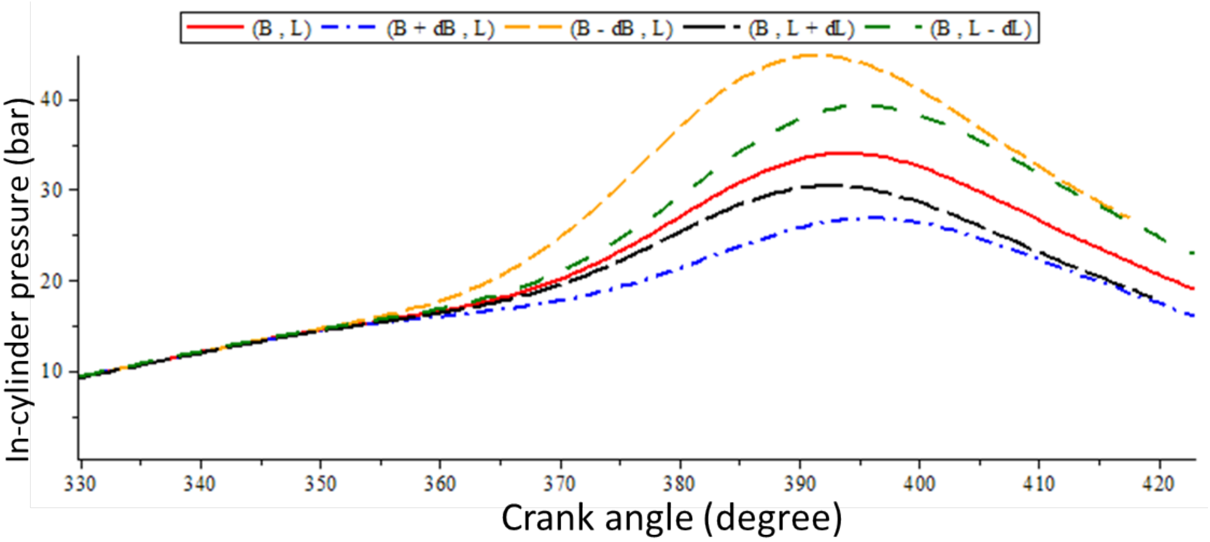

Figure 4.58: In-cylinder pressure variations for different perturbations from the nominal values

The similar approach, which used to generate turbulent flame speed sensitivity function, is employed to derive mechanical torque sensitivity with respect to the design parameters (Equation 4.63). The plots in Figure 4.61 show that the torque variations during the combustion process is not as sensitive as the in-cylinder pressure. The main reason is that the mechanical torque is proportional to product of the in-cylinder pressure and volume at each crank angle. Therefore by increasing either the bore diameter or stroke length, the peak pressure drops and the combustion chamber volume increases.

$$\frac{\partial \tau}{\partial \xi_j} = \left(\frac{\partial f^{\tau}}{\partial P}\right) \text{Ł}_j^P + \left(\frac{\partial f^{\tau}}{\partial \xi_j}\right) \tag{4.63}$$

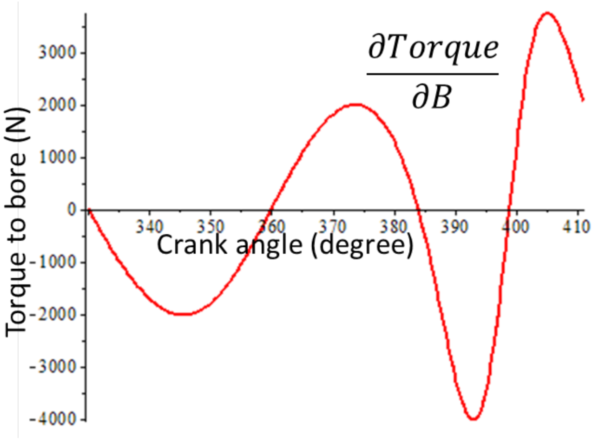

Figure 4.59: Turbulent flame speed sensitivity with respect to the bore diameter

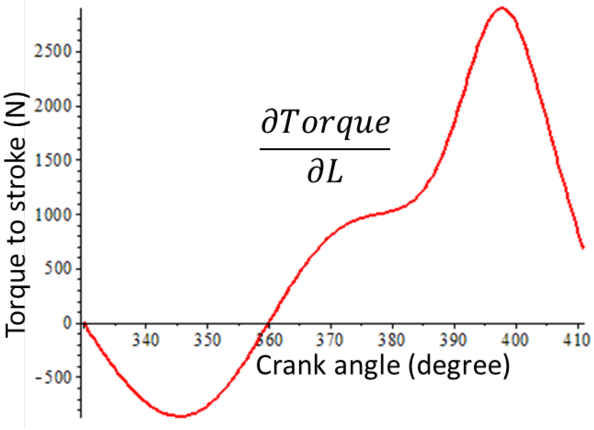

Figure 4.60: Turbulent flame speed sensitivity with respect to the stroke length

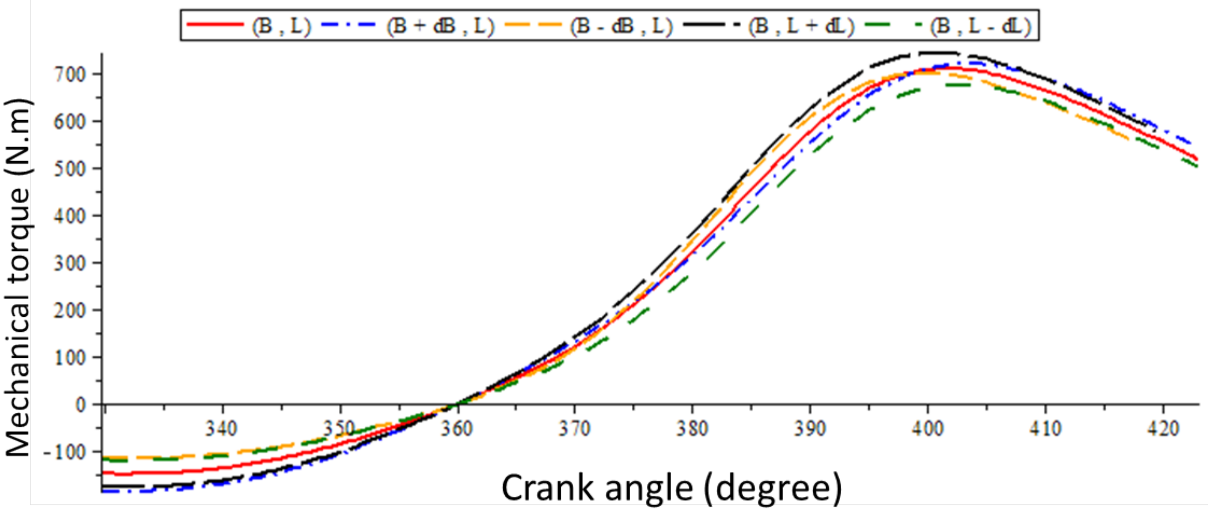

Figure 4.61: Mechanical torque variations for different perturbations from the nominal values

4.6 Chapter Summary

This chapter presents the detailed four-stroke spark ignition (SI) engine model. The model is developed based on the four-stroke in-cylinder operation such as intake, compression, power, and exhaust. The power stroke includes combustion and expansion processes. The combustion process is modeled based on the two-zone combustion (burned/unburned) and turbulent flame propagation theory. The model consists of different sub-models such as piston-cylinder, intake/exhaust manifold, EGR, emission gases, multi body dynamics, and dynamometer (load). The model is able to generate many cycles simulation in one simulation frame, and the inputs can be varied from cycle to cycle. The single-cylinder model is cross-validated against the GT-Power single-cylinder SI engine model, and the results were submitted to the International Journal of Mathematical and Computer Modeling of Dynamical Systems [5].

The symbolic sensitivity analysis is applied to study the effect of the design parameters on the SI engine performance. The symbolic nature of the Maple/MapleSim coding environment helps to study the symbolic manipulation much faster and easier than any other modeling tools. Moreover, the parameter identification technique is employed to identify the empirical Wiebe function parameters. The mass burned during the combustion process plays an important role to define the trend and peak values of the in-cylinder pressure and temperature. Therefore, the empirical parameters must be precisely identified to obtain accurate mass burned shape plot (S-shape).

Chapter 5

Integrated Powertrain Model

This chapter presents the integrated acausal powertrain model, and the application of the model to simulate powertrain characteristics with variable engine speed. The high-fidelity physics-based powertrain model represents a suitable virtual prototype of a real powertrain (physical prototype). Therefore, the proposed powertrain model can be explored and validated virtually in the software to reduce the cost of making physical prototypes and to design more robust and reliable powertrains. In the first section, the physics-based SI engine model and the torque converter are integrated along with the vehicle's longitudinal dynamics. Then, the high-fidelity powertrain model is simulated for a period of time with defined inputs to show the engine speed variations, multi-cycle simulation, and torque converter's impeller torque. Moreover, the proposed model shows the power of acausal components to build a system model more efficiently.

5.1 Modelling

In the previous chapters the details of the physics-based spark ignition engine model and the torque converter model are discussed. The models are evaluated at different operating conditions, and part of the results are validated against experimental results either from the literature or industrial calibrated software (GT-Power software).

The high-fidelity SI engine model is connected to the torque converter model through an acausal connection. The torque converter turbine's shaft is connected to the automatic transmission model, which is uses a gear shifting schedule. The automatic transmission model is connected to the rear wheel of the vehicle. The fixed gear ratio between the automatic transmission and the rear wheel introduces the final drive ratio (also called differential gear ratio). The vehicle model includes the vehicle's mass, inertia, and resistant forces (e.g. aerodynamic and gravitational forces). Figure 5.1 depicts the powertrain model in the MapleSim environment. The sub-models are connected through flange connections, which are mechanical acausal connections.

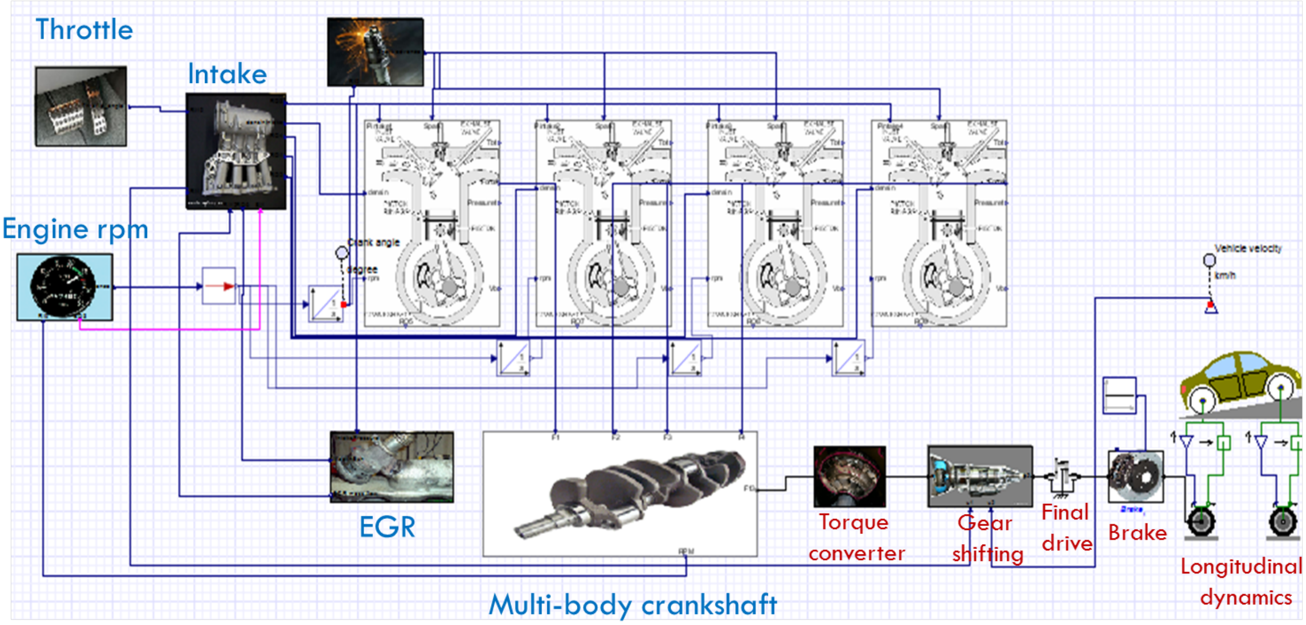

Figure 5.1: Acausal powertrain model in the MapleSim environment

The four-cylinder SI engine model is able to generate simulation results for many cycles simulation, as discussed in the previous chapter. One of the main assumptions in the proposed engine model is running the model at constant engine speed (rpm). This assumption is modified in this section to simulate the powertrain model with variable loads. In other words, in the previous chapter the dynamometer (load) is controlled to keep the engine's shaft speed at some reference speed. In the more realistic case, the powertrain model, the load from the environment and road surface can not be controlled. Therefore, the load on the engine's shaft is variable and consequently the engine's shaft speed is variable. However, the assumption of constant engine speed at each cycle is valid due to the two-zone combustion modeling assumption. In other words, the engine speed is kept constant during a four-stroke operation (720 degrees of crankshaft rotation), then the new cycle runs with new value of the shaft speed.

The idea to combine both variable engine speed during the simulation and constant engine speed during the cycle, is using triggered sampler to discretize the multibody crankshaft's speed and hold it constant during the cycle. In other words, the actual engine speed from the engine's shaft sensor is discretized with variable sampling time. Figure 5.2 show the schematic triggered sampler to discretize the engine speed at each sampling time. The sampling time is varied as a function of the engine speed (rpm), as shown in Equation 5.1. The cycle time (Δt_{cycle}) represents the time duration for 720 degrees of crankshaft rotation at the engine speed of $nrpm$.

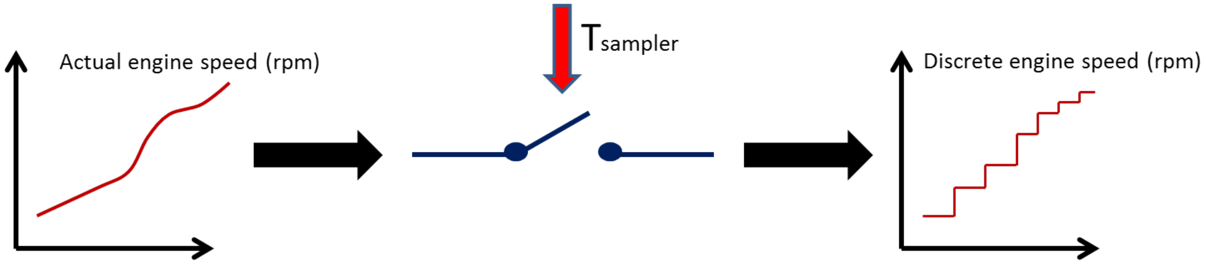

Figure 5.2: Schematic diagram of triggered sampler to discretize engine speed

$$T_{sampler} \equiv \Delta t_{cycle} = \frac{120}{n} \tag{5.1}$$

The automatic transmission model includes physics-based torque converter model and rule-based gear shifting schedule. The torque converter model, which is discussed in detail in Chapter 3, can capture the forward and reverse flow operation. The gearbox model with rule-based gear shifting schedule is represented by Equations 5.2 and 5.3. The input torque to the gearbox is the torque converter turbine torque (τ_{in}) and the output torque (τ_{out}) is multiplied by the final drive ratio (or differential gear ratio) and delivered to the rear wheels.

$$\tau_{out} = \tau_{in} G_i E_i \tag{5.2}$$

$$w_{in} = G_i w_{out} \tag{5.3}$$

The variations of each gear ratio based on the vehicle longitudinal velocity and the engine speed is listed in Table 3.3.

The brake model generates the resistant torque to decelerate the vehicle. For this purpose, the brake model is placed between the differential model, final drive ratio, and the tire model through acausal connection. The model is developed based on the Coulomb friction theory. Equation 5.4 represents the resistant brake torque, which is available in the MapleSim library [56]. The resistant braking torque is proportional to the geometry of rotational discs (C_{geo}), velocity-dependent friction coefficient (μ_ω), and normal force acting on the discs by pushing the brake pedal (driver's command).

$$\tau_{brake} = C_{geo} \mu_\omega F_n \tag{5.4}$$

The brake geometry constant (C_{geo}) represents the brake's disc geometry as shown in Equation 5.5, where r_i, r_o, and N_{disc} are inner and outer radius of the disc as well as the number of friction interfaces, respectively.

$$C_{geo} = \frac{N_{disc}}{2}(r_i + r_o) \tag{5.5}$$

The normal force (F_n) is actually the input signal to the brake model and shows the driver's push on the brake pedal. Equation 5.6 shows the normalized form of the normal force, where the $F_{n_{max}}$ is provided as a constant parameter during the simulation. The normalized signal ($F_{normalized}$) is varied from zero (no braking) to one (fully braking) to show the driver's command to decelerate a vehicle.

$$F_n = F_{n_{max}} F_{normalized} \tag{5.6}$$

The output torque from the differential, final drive ratio, rotates the wheels and axle. In the vehicle longitudinal dynamics model, there are two tires instead of four tires. Since the lateral dynamics is not considered, so each tire (front/rear) represents the properties of two tires. Figure 5.3 shows the schematic tire model including the inputs. The axle torque (τ_{axle}) is acting on the tire's axle to drive the wheels. The tire model is connected to the vehicle longitudinal dynamics model through two flanges, which is shown by F_x and F_z in Figure 5.3. F_x and F_z represent the axle longitudinal flange force and axle vertical force, respectively.

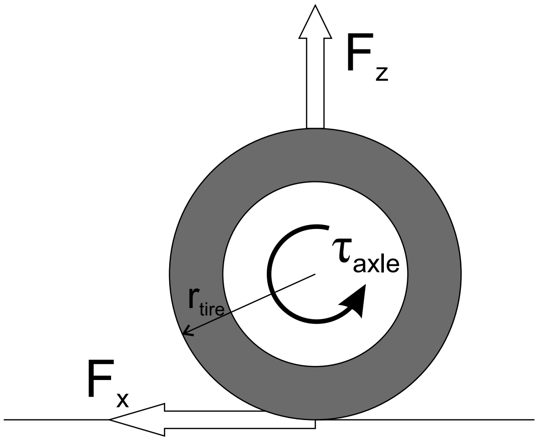

Figure 5.3: Schematic tire model

Equation 5.7 represents the rotational motion of a tire, where I_{tire} and r_{tire} are tire inertia and radius.

$$I_{tire}\dot{\omega}_{tire} = \tau_{axle} - F_x.r_{tire} \tag{5.7}$$

There are different mathematical tire models such as Magic formula and linear saturation model [64]. The linear saturation tire model is used in this study to calculate tire contact force as shown in Equation 5.8. F_{z0}, F_{x0}, and ζ_0 represent the nominal vertical load acting on the tire, traction force at nominal vertical load, and the tire slip ratio at peak traction force, respectively.

$$F_x = \begin{cases} 0 & F_z < 0 \\ \begin{cases} F_z \frac{F_{x0}}{F_{z0}} \frac{\zeta}{\zeta_0} & |\zeta| < \zeta_0 \\ F_z \frac{F_{x0}}{F_{z0}} \frac{\zeta}{|\zeta_0|} & |\zeta| \geq \zeta_0 \end{cases} & F_z > 0 \end{cases} \tag{5.8}$$

The slip ratio (ζ), one of the key variables in tire modeling, is approximated by Equation 5.9.

$$\zeta = \frac{r_{tire}\omega_{tire} - \nu_x}{max\left(|r_{tire}\omega_{tire}|, |\nu_x|\right)} \tag{5.9}$$

The vehicle longitudinal dynamics model includes the vehicle geometry, mass, and resistant forces such as aerodynamic force (F_{aero}), rolling resistance (F_{roll}), and gravitational force (F_{grav}). The front and rear tires introduce the rolling resistant forces. The tire contact force (Equation 5.8) is a function of a vehicle's weight and road friction coefficient. Figure 5.4 shows the schematic vehicle model traveling on an inclined road.

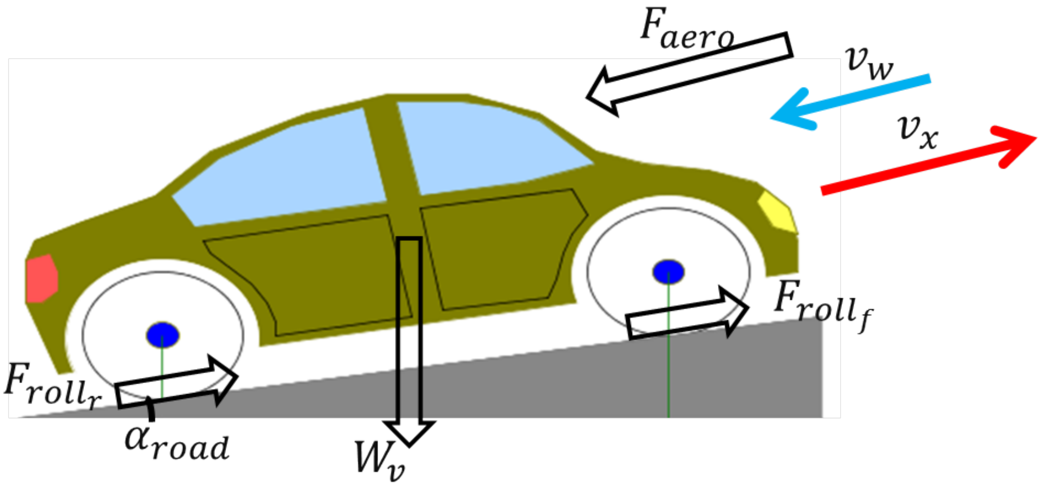

Figure 5.4: Schematic vehicle longitudinal dynamics model

The effect of a vehicle's weight and road inclination and friction appears in the gravitational and rolling resistant forces as derived in Equations 5.10 and 5.11.

$$F_{grav} = M_v g \sin(\alpha_{road}) \tag{5.10}$$

$$F_{roll} = F_{roll_f} + F_{roll_r} = \mu_{road} M_v g \cos(\alpha_{road}) \tag{5.11}$$

The aerodynamic force is proportional to the squared forward velocity of the vehicle and is represented by Equation 5.12.

$$F_{aero} = \frac{1}{2} D_{air} \rho_{air} A_{front} |\nu_x - \nu_w| (\nu_x - \nu_w) \tag{5.12}$$

Equation 5.13 represents the equation of motion of the vehicle in the longitudinal dynamics.

The traction force (F_x) is calculated from the tire model.

$$M_v \dot{\nu}_x = F_x - F_{roll} - F_{aero} - F_{grav} \tag{5.13}$$

5.2 Simulation

The proposed physics-based powertrain model is able to capture both transient and steady state characteristics. Moreover, the model is able to generate results for almost all operating conditions such as travelling up/down hills, with full/partial load, at low/high engine speed for different vehicles. The whole powertrain model includes both casual and acausal connections. The main causal connections are related to the gas exchange process in the SI engine model. However, the powertrain sub-models are connected through acausal connections such as rotational and translational ports. Unlike the causal modelling approach which the physics of a model is hidden under the signal-flow connections, the acausal modelling approach gives better insight of a physical meaning sub-models, parameters, and connections [62].

The parameters and values of the vehicle including the chassis and the tire model are provided in Table 5.1. The SI engine and torque converter specifications are listed in Table 4.1 and 3.1, respectively. The vehicle is travelling on a flat road (no road inclination), and the engine is operating at fully-opened throttle angle (full load operation). As mentioned before, the load acting on the vehicle's chassis and tires are variable and consequently the engine speed (rpm) is variable. Figure 5.5 shows the actual engine speed from the engine's shaft rpm sensor and discretized engine speed, which is used to run the SI engine model at each sampling time. The engine speed is assumed started from 600 rpm. Therefore, the first engine cycle (or 720 degrees) takes 0.2 seconds as calculated in Equation 5.1. The next engine cycle is repeated based on the engine speed at time equal to 0.2 seconds. The sampling time is proportional to the inverse of the engine speed, so at higher engine speeds the sampling time is shorter. Therefore, the approximated engine speed (discretized engine speed) is much closer to the actual engine speed.

Table 5.1: Parameters for a compact sedan

Vehicle mass	1417 kg
Tire mass	10 kg
Coefficient of air drag	0.35
Frontal area	2.58 m^2
Rolling radius of tire	0.3 m
Final drive ratio	3.64
Longitudinal tire slip ratio at max force	0.1
Inertia of wheel and axle	1 $kg.m^2$
Ground inclination angle	0 $degrees$
Air density	1.2 $kg.m^{-3}$
Road friction coefficient	0.02
Gravitational acceleration	9.81 $m.s^{-2}$

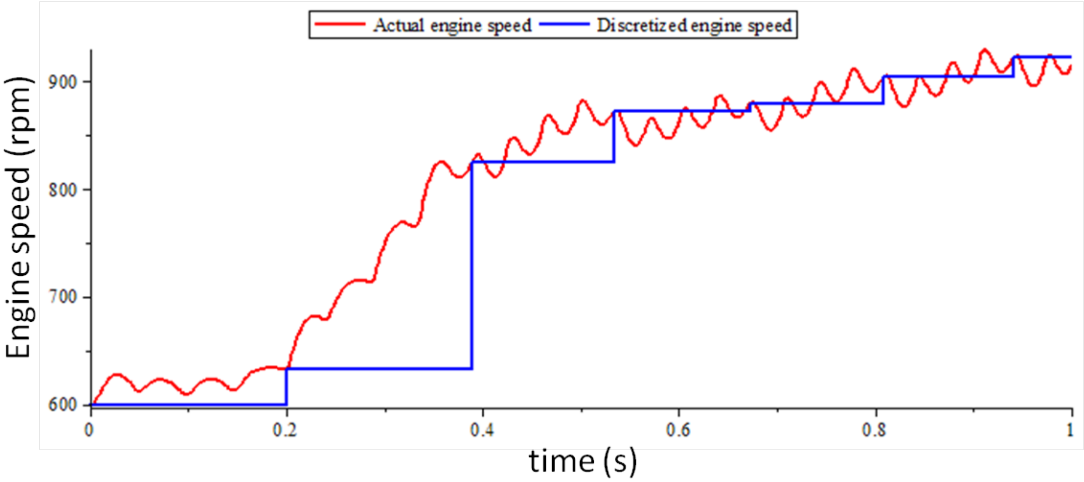

Figure 5.5: Variable engine speed in powertrain simulation

The vehicle forward velocity and acceleration is shown in Figure 5.6. The vehicle starts from rest position (the initial velocity is zero). There is an acceleration peak at the start of the motion. The acceleration curve shows some vibration with low amplitude and high frequency, which is due to the engine pulsation (cranking). Although the longitudinal powertrain vibration is out of scope of this research, the model can be used as a suitable plant model to study longitudinal vibration of a powertrain due to the engine pulsation, gear shifting, and environmental disturbances.

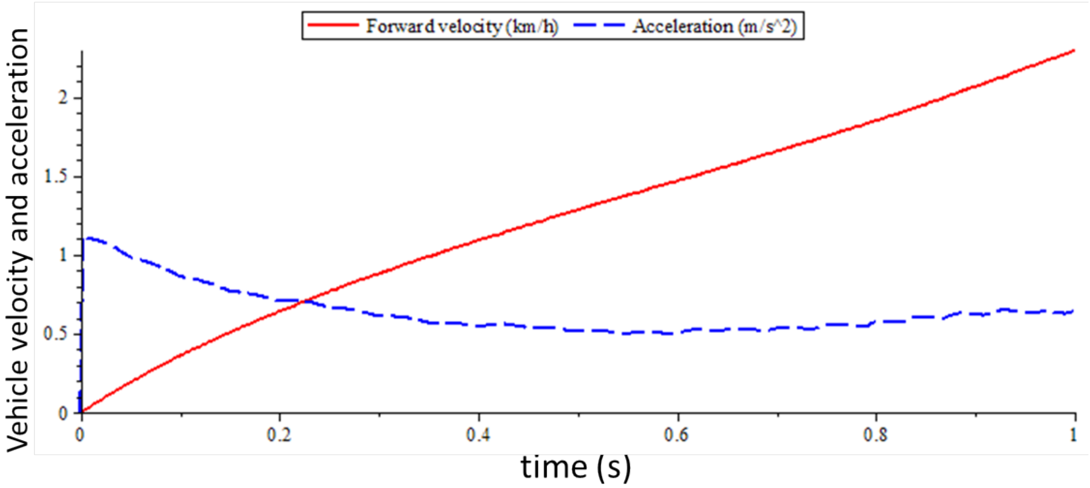

Figure 5.6: Vehicle forward velocity and acceleration

Figure 5.7 shows the pump's torque and turbine's torque of the math-based torque converter model. As discussed in the Chapter 3, one of the main advantages of using a torque converter in an automatic transmission is its capability to filter disturbances introduced from the engine side (e.g. engine cranking). In other words, the torque converter model works as a filter to deliver smooth torque to the transmission shaft.

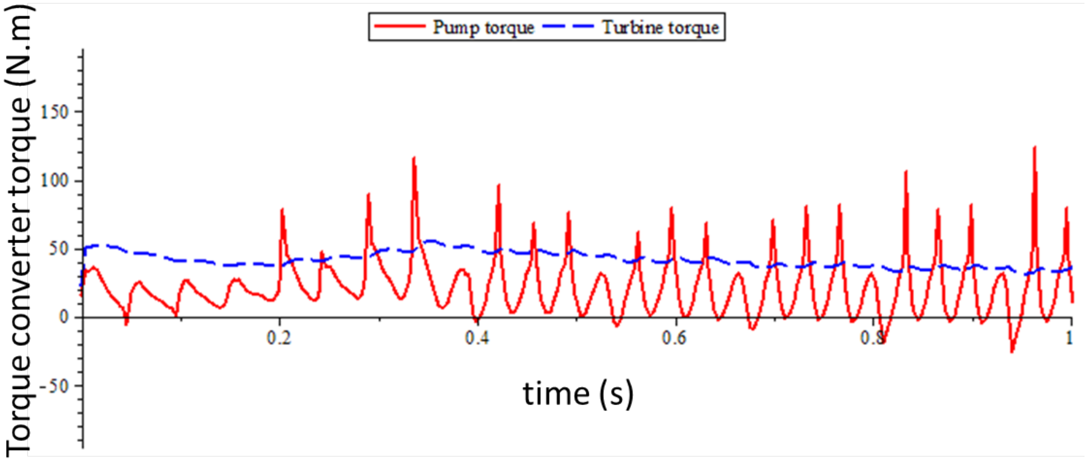

Figure 5.7: Torque converter pump and turbine shaft's torque

5.3 Chapter Summary

This chapter presents the acausal powertrain model including vehicle longitudinal dynamics. The developed four-cylinder SI engine model (see Chapter 4) is connected to the acausal torque converter model (see Chapter 3), and the torque converter turbine's shaft is connected to the rest of the powertrain such as automatic transmission with rule-based gear shifting schedule, braking system, final drive ratio, wheels, and vehicle chassis. The engine speed and load are variable during the powertrain simulation. Therefore, the assumption of predefined load and speed in the previous chapter is modified by developing triggered sampler circuit to discretize the engine's shaft speed at each cycle. The proposed powertrain model works in a wide range of engine speed and load, and can be adopted for different types of vehicles.

Chapter 6

Conclusions and Future Work

6.1 Conclusions

In this research, the physics-based powertrain model is developed in the MapleSim software. The major modeling approach in this study is based on an acausal modeling rather than causal, signal-flow, modeling approach. However, some physical phenomenon is event-based, and can not be represented as an acausal model. For instance, the energy conversion from the combustion chemical reactions to mechanical work is a unidirectional process and can not be reversed.

The main focus of this dissertation is on developing physics-based hydrodynamic torque converter model, SI engine model, and the integrated powertrain model. These three topics are presented in detail in Chapter 3, Chapter 4, and Chapter 5 respectively. The following sub-sections summarize the thesis and highlight the main contributions of this research.

Acausal physics-based torque converter model :

The hydrodynamic torque converter is modelled at different operating modes such as torque multiplication, coupling, and reverse flow operation. The model is fully physics-based by deriving angular momentum equations of the impellers and the conservation of the energy. The parametric sensitivity analysis and damping characteristics of the torque converter model are evaluated at different operating modes. The frequency response analysis shows that the torque converter can significantly damp high frequency disturbances transferred from the pump side to the turbine side and vice versa for all operating modes.

Engine braking due to a torque converter reverse flow operation :

The torque converter model can be integrated with vehicle longitudinal dynamics to evaluate the torque converter transient characteristics during gear shifting and the flow transition in the hydrodynamic torque converter. The transition happens when the torque converter turbine's shaft starts rotating faster than the pump's shaft. This phenomenon in the powertrain, which is called engine braking, can assist the braking system to slow down the vehicle. The simulation results confirm the ability of the model to represent the engine braking phenomenon in the automatic driveline, which slows the forward speed during vehicle coasting.

Physics-based four-cylinder SI engine model :

The four-cylinder SI engine model is developed based on the two-zone combustion and turbulent flame propagation theory along with the multi-body modeling approach for the mechanical parts. The model can predict fuel consumption, brake power/torque, and kinetic emission gases (e.g. NO and CO) at different engine speed and throttle angle. The model is able to generate multi-cycle simulation for different inputs from one cycle to the other one. The whole model, including intake manifold, EGR, multibody crankshaft, and cylinders, consists of a set of differential-algebraic equations (DAEs) with variable inputs and initial conditions at each cycle. MapleSim solvers are very powerful in terms of handling the DAEs and hybrid dynamic system. Also, by taking advantages of the symbolic nature of MapleSim in modeling, a symbolic sensitivity analysis can be easily evaluated for design purposes.

Acausal powertrain model working at a wide range of speeds and loads :

The four-cylinder SI engine model is connected to the automatic transmission through the hydrodynamic torque converter model. The automatic transmission model is connected to the vehicle's chassis and rear tires through a differential gear. Moreover, the braking system is connected to the tires and can be controlled by the driver. All components are connected through the rotational flange port, which represents an acausal connection in MapleSim. The proposed physics-based powertrain model is able to capture both transient and steady state characteristics. Moreover, the model is able to generate results for almost all operating conditions such as travelling up/down hills, with full/partial load, at high/low engine speed for different vehicles.

6.2 Future Work

The physics-based powertrain is a plant model that can be used for different purposes. Each sub-model in the integrated powertrain (e.g. IC engine and automatic transmission) can be separately evaluated as well. Moreover, the whole powertrain model or the components can be upgraded based on different vehicle parameters and even the new technologies. For instance, the SI engine model can be replaced by a diesel engine or HCCI technology [90] to evaluate the performance and operation of the powertrain. The mathematical formulation of the dynamic powertrain model allows users to easily modify the equations of the system for different purposes. The following subjects could be considered as potential future research based on the current study:

Parametric sensitivity analysis of the powertrain :

The parametric (symbolic) sensitivity analysis has been done for the torque converter [14] and the SI engine model at the component level. It is interesting research to evaluate the effect of parameters on the powertrain's performance in a system level parametric sensitivity analysis. Moreover, studying the effect of the parameters simultaneously (multi-parameter sensitivity analysis) on the powertrain performance, such as driveability, ride comfort, and fuel consumption, helps the designers to understand the interaction among different components and parameters to obtain more efficient powertrain components.

Vibration analysis of the powertrain :

The developed cycle-by-cycle SI engine model is able to simulate the engine pulsation, and the longitudinal vehicle model can simulate the vibrations which are induced from the environment. Therefore, the proposed powertrain model can be used to study the longitudinal powertrain vibration [23, 25, 60]. In Chapter 3, the torque converter damping characteristics has been evaluated at the forward and reverse flow operation. The damping characteristics of the torque converter's lock-up clutch and the braking system is an interesting future research.

Model-based control design for optimal gear shifting :

The math-based powertrain model makes it suitable for model-based control applications, where the controller is design based on the dynamics behaviour of the model. One of the hot topics in the model-based powertrain control is generating gear shifting maps to improve vehicle's performance such as the ride comfort, the vehicle's jerk during gear shifting, and fuel consumption. This research is called the optimal gear shifting strategy. Different optimization techniques, both on-line and off-line, can be applied to the powertrain model to achieve better performance [36,37,52]. One of the interesting model-based control strategies is model-predictive-control (MPC) which can be used for different objective function to minimize fuel consumption and/or enhance the ride comfort.

Variable valve timing (VVT) simulation :

The developed four-cylinder engine model in this study uses a fixed valve timing during the intake and exhaust strokes. However, the model is able to be adapted for a VVT simulation. The VVT topic is an active area of research [8, 33, 55], and the VVT technology is implemented in some IC engines for better performance. The physics-based VVT model can be added to the current model to evaluate the effect of VVT on the brake torque, fuel consumption, and emission gasses.

Acausal chemistry-based combustion model :

The current combustion model in this research is based on the two-zone modeling approach with turbulent flame prorogation through the combustion chamber. The combustion reactions are not fully modeled in the chemistry-based approach. The causal thermodynamics, heat transfer, and chemistry-based emission model can be replaced by the an acausal modeling approach to achieve a more feasible combustion model. An interesting research in this area is developing acausal models [22,79] of the chemical kinetic reactions (forward and backward directions), and compressible flow thermodynamic (e.g. gas exchange process during the intake and exhaust process).

References

[1] E. Abu-Nada, I. Al-Hinti, A. Al-Sarkhi, and B. Akash. Effect of piston friction on the performance of si engine: a new thermodynamic approach. *TRANSACTIONS-ASME JOURNAL OF ENGINEERING FOR GAS TURBINES AND POWER*, 130(2):022802, 2008.

[2] H. Adibi Asl, N. L. Azad, and J. McPhee. Math-based modeling and parametric sensitivity analysis of torque converter performance characteristics. *SAE Technical Paper*, paper no. 2011-04-12, 2011.

[3] H. Adibi Asl, N. L. Azad, and J. McPhee. Modeling torque converter characteristics in automatic driveline: lock-up clutch and engine braking simulation. *American Society of Mechanical Engineers*, 2012.

[4] H. Adibi Asl, N. L. Azad, and J. McPhee. Math-based torque converter modeling to evaluate damping characteristics and reverse flow mode operation. *International Journal of Vehicle Systems Modelling and Testing*, 2013.

[5] H. Adibi Asl, R. Fraser, and J. McPhee. Math-based spark ignition engine modeling including emission prediction for control applications. *International Journal of Vehicle Systems Modelling and Testing*, under review, 2013.

[6] H. Adibi Asl, R. Masoudi, R. Fraser, and J. McPhee. Symbolic sensitivity analysis of math-based spark ignition engine with two-zone combustion model. *SAE Technical Paper*, under review, 2014.

[7] H. Adibi Asl, M. Saeedi, R. Fraser, P. Goossens, and J. McPhee. Mean value engine model including spark timing for powertrain control application. *SAE Technical Paper*, 2013-01-0247, 2013.

[8] T. Ahmad and M. A. Theobald. A survey of variable-valve-actuation technology. *Society of Automotive Engineers*, paper no. 891674, 1989.

[9] S. Al-Baghdadi, M. Abdul-Resul, S. Al-Janabi, and H. Abdul-Kadim. Improvement of performance and reduction of pollutant emission of a four stroke spark ignition engine fueled with hydrogen–gasoline fuel mixture. *Energy conversion and management*, 41(1):77–91, 2000.

[10] C. F. Aquino. *Transient A/F control characteristics of the 5 liter central fuel injection engine*, volume paper no. 810494. Society of Automotive Engineers, 1981.

[11] I. Arsie, C. Pianese, and G. Rizzo. Models for the prediction of performance and emissions in a spark ignition engine-a sequentially structured approach. *SAE transactions*, 107:1065–1079, 1998.

[12] K. J. Astrom and R. M. Murray. *Feedback systems: an introduction for scientists and engineers.* Princeton university press, 2008.

[13] M. L. Baglione. *Development of System Analysis Methodologies and Tools for Modelling and Optimizing Vehicle System Efficiency.* Ph.d. dissertation, University of Michigan, 2007.

[14] J. Banerjee, H. Adibi Asl, N.L. Azad, and J. McPhee. Parametric importance analysis and design optimization of a torque converter model using sensitivity information. *SAE International Journal of Passenger Cars-Mechanical Systems*, 5(1):621–638, 2012.

[15] H. Bayraktar. Mathematical modeling of spark-ignition engine cycles. *Energy sources*, 25(7):651–666, 2003.

[16] H. Bayraktar. Experimental and theoretical investigation of using gasoline–ethanol blends in spark-ignition engines. *Renewable Energy*, 30(11):1733–1747, 2005.

[17] H. Bayraktar and O. Durgun. Development of an empirical correlation for combustion durations in spark ignition engines. *Energy conversion and management*, 45(9):1419–1431, 2004.

[18] R. S. Benson, W. Annand, and P. C. Baruah. A simulation model including intake and exhaust systems for a single cylinder four-stroke cycle spark ignition engine. *International Journal of Mechanical Sciences*, 17(2):97–124, 1975.

[19] N. C. Blizard and J. C. Keck. Experimental and theoretical investigation of turbulent burning model for internal combustion engines. *Society of Automotive Engineers*, paper no. 740191, 1974.

[20] P. N. Blumberg. Powertrain simulation: A tool for the design and evaluation of engine control strategies in vehicles. Technical report, 1976.

[21] P. N. Blumberg, G. A. Lavoie, and R. J. Tabaczynski. Phenomenological models for reciprocating internal combustion engines. *Progress in Energy and Combustion Science*, 5(2):123–167, 1979.

[22] P. Bowles, M. Tiller, H. Elmqvist, and D. Bruck. Feasibility of detailed vehicle modeling. *Society of Automotive Engineers*, paper no. 01P-321, 2001.

[23] A. Boysal and H. Rahnejat. Torsional vibration analysis of a multi-body single cylinder internal combustion engine model. *Applied Mathematical Modelling*, 21(8):481–493, 1997.

[24] S. Chow, J. Mallet-Paret, and J. A. Yorke. A homotopy method for locating all zeros of a system of polynomials. In *Functional differential equations and approximation of fixed points*, pages 77–88. Springer, 1979.

[25] A. R. Crowther and N. Zhang. Torsional finite elements and nonlinear numerical modelling in vehicle powertrain dynamics. *Journal of Sound and Vibration*, 284(3):825–849, 2005.

[26] J. Deur, D. Hrovat, and J. Asgari. Analysis of torque converter dynamics. ASME, 2002.

[27] D. J. Dobner. Mathematical engine model for development of dynamic engine control. *Society of Automotive Engineers*, paper no. 800054, 1980.

[28] D. J. Dobner and R. D. Fruechte. An engine model for dynamic engine control development. In *American Control Conference, 1983*, pages 73–78. IEEE, 1983.

[29] D. M. Dunlavy and D. P. OLeary. Homotopy optimization methods for global optimization. *Sandia National Laboratories, Report SAND2005-7495*, 2005.

[30] H. Elmqvist, D. Bruck, and M. Otter. Dymola-user's manual. *Dynasim AB, Research Park Ideon, Lund, Sweden*, 1996.

[31] M. Fons, M. Muller, A. Chevalier, C. Vigild, E. Hendricks, and S. Sorenson. Mean value engine modelling of an si engine with egr. *SAE Technical Paper*, pages 01–0909, 1999.

[32] P. Fritzson, F. Cellier, and D. Broman. 2nd international workshop on equation-based object-oriented languages and tools. 2008.

[33] C. Gray. A review of variable engine valve timing. *SAE transactions*, 97:631–641, 1989.

[34] GT-POWER®. *Version v 7.3.0.* The Gamma Technologies Inc., Westmont, USA, 2013.

[35] L. Guzzella and C. Onder. *Introduction to modeling and control of internal combustion engine systems*. Springer, 2009.

[36] A. Haj-Fraj and F. Pfeiffer. Optimization of gear shift operations in automatic transmissions. In *Advanced Motion Control, 2000. Proceedings. 6th International Workshop on*, pages 469–473. IEEE, 2000.

[37] A. Haj-Fraj and F. Pfeiffer. Optimal control of gear shift operations in automatic transmissions. *Journal of the Franklin Institute*, 338(2):371–390, 2001.

[38] Y. Harigaya, M. Suzuki, and M. Takiguchi. Analysis of oil film thickness on a piston ring of diesel engine: effect of oil film temperature. *Journal of engineering for gas turbines and power*, 125(2):596–603, 2003.

[39] D. L. Harrington and J. A. Bolt. Analysis and digital simulation of carburetor metering. *Society of Automotive Engineers*, paper no. 700082, 1970.

[40] H. Heisler. *Advanced vehicle technology.* Butterworth-Heinemann, 2002.

[41] E. Hendricks, A. Chevalier, M. Jensen, S. C. Sorenson, D. Trumpy, and J. Asik. Modelling of the intake manifold filling dynamics. *Society of Automotive Engineers*, paper no. 960037, 1996.

[42] E. Hendricks and S. C. Sorenson. Mean-value modeling of si engines. *Society of Automotive Engineers*, paper no. 900616, 1990.

[43] E. Hendricks and S. C. Sorenson. Si engine controls and mean value engine modelling. *Society of Automotive Engineers*, paper no. 910258, 1991.

[44] E. Hendricks and T. Vesterholm. The analysis of mean value engine models. paper no. 890682, 1989.

[45] J. Heywood. Internal combustion engine fundamentals. 1988.

[46] G. F. Hohenberg. Advanced approaches for heat transfer calculations. *Society of Automotive Engineers*, paper no. 790825, 1979.

[47] D. Hrovat and W. E. Tobler. Bond graph modeling and computer simulation of automotive torque converters. *Journal of the Franklin institute*, 319(1):93–114, 1985.

[48] T. Ishihara and R. I. Emori. *Torque converter as a vibrator damper and its transient characteristics*. Society of Automotive Engineers, 1966.

[49] S. Ishizuka. Symbolic and numeric dae approach for dynamical system simulation. In *ICCAS-SICE, 2009*, pages 2388–2391. IEEE, 2009.

[50] A. Kesy and Z. Kesy. Damping characteristics of a transmission system with a hydrodynamic torque converter. *Journal of sound and vibration*, 166(3):493–506, 1993.

[51] Z. Kesy and A. Kesy. Application of numerical methods to the modelling of transmission systems with hydrodynamic torque converter. *International Journal of Computer Applications in Technology*, 31(3):275–283, 2008.

[52] D. Kim, H. Peng, S. Bai, and J. M. Maguire. Control of integrated powertrain with electronic throttle and automatic transmission. *Control Systems Technology, IEEE Transactions on*, 15(3):474–482, 2007.

[53] Y. H. Kim, J. Yang, and J. M. Lee. A study on the transient characteristics of automatic transmission with detailed dynamic modeling. *SAE Paper*, 941014, 1994.

[54] A. J. Kotwicki. *Dynamic models for torque converter equipped vehicles*. Society of Automotive Engineers, 1982.

[55] T. H. Ma. Recent advances in variable valve timing. In *Automotive Engine Alternatives*, pages 235–252. Springer, 1987.

[56] MapleSim®. *Version 6.1.* The Maplesoft Inc., Waterloo, Canada, 2013.

[57] R. Masoudi, H. Adibi Asl, N. L. Azad, and J. McPhee. Parameter identification of a quasi-dimensional spark ignition engine model. *SAE Technical Paper*, under review, 2014.

[58] R. A. Mercure. *Review of the Automotive Torque Converter*. Society of Automotive Engineers, 1979.

[59] M. J. Moran, H.N. Shapiro, D. Boettner, and M. Bailey. *Fundamentals of engineering thermodynamics*. Wiley, 2010.

[60] Z. P. Mourelatos. A crankshaft system model for structural dynamic analysis of internal combustion engines. *Computers & Structures*, 79(20):2009–2027, 2001.

[61] C. Newman, J. Batteh, and M. Tiller. Spark-ignited-engine cycle simulation in modelica. In *2nd International Modelica Conference Proceedings*, pages 133–142, 2002.

[62] H. Olsson, M. Otter, S. E. Mattsson, and H. Elmqvist. Balanced models in modelica 3.0 for increased model quality. *Proceedings of 6th International Modelica Conference*, 2008.

[63] A. Ostermann. Sensitivity analysis, analyzing uncertainty in civil engineering. *Springer Berlin Heidelberg*, pages 101–114, 2005.

[64] H. B. Pacejka. *Tire and Vehicle Dynamics*. SAE International and Elsevier, second edition, 2005.

[65] B. Pohl. Transient torque converter performance, testing, simulation and reverse engineering. *SAE transactions*, 112(6):201–216, 2003.

[66] B. K. Powell. A dynamic model for automotive engine control analysis. In *Decision and Control including the Symposium on Adaptive Processes, 1979 18th IEEE Conference on*, volume 18, pages 120–126. IEEE, 1979.

[67] J. D. Powell. A review of ic engine models for control system design. In *Proc. of the 10th IFAC World Congress, San Francisco, 1987*, 1987.

[68] J. I. Ramos. *Internal combustion engine modeling*, volume 80. Hemisphere Publishing Corporation New York, 1989.

[69] D. Robinette, M. Grimmer, and R. Beikmann. Dynamic torque characteristics of the hydrodynamic torque converter. *SAE International Journal of Passenger Cars-Mechanical Systems*, 4(2):1023–1032, 2011.

[70] W. H. Rong, K. Tanaka, and H. Tsukamoto. Torque converter with lock-up clutch by bond graphs. *ASME, FEDSM97-3368SM*, 97, 2007.

[71] M. Saeedi. *A Mean Value Internal Combustion Engine Model in MapleSim*. Master's thesis, University of Waterloo, 2010.

[72] A. Saltelli, S. Tarantola, and F. Campolongo. Sensitivity analysis as an ingredient of modeling. *Statistical Science*, pages 377–395, 2000.

[73] C. Schmitke and P. Goossens. Symbolic computation techniques for multibody model development and code generation. *in Proc of Multibody Dynamics 2011*, 2011.

[74] P. Senecal, J. Xin, and R. Reitz. Prediction of residual gas fraction in ic engines. *Society of Automotive Engineers*, paper no. 962052, 1996.

[75] Manual SIMULINK. Using simulink. *The Math Works Inc., Version*, 4, 2000.

[76] S. Sitthiracha. An analytical model of spark ignition engine for performance prediction. Master's thesis, King Mongkat's Institue of Technology, Thailand, 2006.

[77] R. J. Tabaczynski, C. R. Ferguson, and K. Radhakrishnan. Turbulent entrainment model for spark-ignition engine combustion. *Society of Automotive Engineers*, paper no. 7706146-5, 1977.

[78] A. Taghavipour, R. Masoudi, N. L. Azad, and J. McPhee. High-fidelity modeling of a power-split plug-in hybrid electric powertrain for control performance evaluation. In *Paper presented at the ASME 2013 World Congress*, 2013.

[79] M. Tiller, P. Bowles, and M. Dempsey. Development of a vehicle model architecture in modelica. In *Paper presented at the 3rd International Modelica Conference*, 2003.

[80] Toyota Technical Training. Automatic transmission, 2006. Course 262 - Section 2.

[81] S. R. Turns. *An introduction to combustion*, volume 499. McGraw-hill New York, 1996.

[82] S. Verhelst and C. Sheppard. Multi-zone thermodynamic modelling of spark-ignition engine combustion–an overview. *Energy Conversion and Management*, 50(5):1326–1335, 2009.

[83] C. P. Vyasarayani, T. Uchida, A. Carvalho, and J. McPhee. Parameter identification in dynamic systems using the homotopy optimization approach. *Multibody System Dynamics*, 26(4):411–424, 2011.

[84] C. P. Vyasarayani, T. Uchida, and J. McPhee. Single-shooting homotopy method for parameter identification in dynamical systems. *Physical Review E*, 85(3):036201, 2012.

[85] K. B. Wipke, M. R. Cuddy, and S. D. Burch. Advisor 2.1: a user-friendly advanced powertrain simulation using a combined backward/forward approach. *Vehicular Technology, IEEE Transactions on*, 48(6):1751–1761, 1999.

[86] H. Xia and P. Oh. A dynamic model for automotive torque converters. *International Journal of Vehicle Design*, 21(4):344–354, 1999.

[87] H. Xu, M. D. Bryant, R. D. Matthews, T. M. Kiehne, B. D. Steenwyk, N. W. Bolander, and F. Sadeghi. Friction predictions for piston ring-cylinder liner lubrication. American Society of Mechanical Engineers, 2004.

[88] Yeliana. *Parametric Combustion Modeling for Ethanol-gasoline Fuelled Spark Ignition Engines*. PhD thesis, Michigan Technological University, 2010.

[89] W. W. Yuen and H. Servati. A mathematical engine model including the effect of engine emissions. paper no. 840036, 1984.

[90] H. Zhao. *HCCI and CAI engines for the automotive industry.* CRC Press Boca Raton, FL, 2007.